Active Optical Devices in Integrated Optics

Pedro Miguel Mesquita Marques
Master in Engineering Physics
Department of Physics and Astronomy
Faculty of Sciences of the University of Porto
Faculty of Engineering of the University of Porto
2025

Active Optical Devices in Integrated Optics

Pedro Miguel Mesquita Marques
Dissertation carried out as part of the Master in Engineering Physics
Department of Physics and Astronomy
2025

Supervisor
Paulo Vicente da Silva Marques
Associate Professor
Faculty of Sciences of University of Porto

Co-supervisor
João Miguel Mendes da Silva Maia
PhD Researcher
INESC TEC

Acknowledgments

Life doesn't wait.

It does not care if you are happy or sad, vivid or tired. It does not wait for you to get up to give you another spin. And that is how I would describe this journey: full of unpredictable twists and turns, each stone I tripped on became a lesson, each puddle stepped in morphed into an experience. However, on rare occasions, the moody foggy mornings became mystical, the burdensome walks to work turned blissful, because the desire to understand became stronger than the necessity to get the job done. In this work

I found passion.

I am very grateful to everyone that helped me through the path that I chose.

To Prof. Paulo Marques for giving me the main framework of this thesis, for helping with the necessary hardware and in general, for being a great support.

A special thanks goes to my co-supervisor, Dr. João Maia, for everything, from teaching me how to use the lab equipment, to answering my unending questions, and for helping me the most when times got tough.

To all my friends who, one way or another, were there for me, either by accompanying me in runs at the sunset, or going out for a coffee at night, or by simply improving my day.

To the few persons that only passed by my life, leaving it a lot better than before, I wish you the world.

But most importantly, if it were not for my Family, I would not have been able to do anything at all. I am eternally grateful to my parents, for walking side by side with me, despite my occasional bad moods. To my godfathers, for being so close to me, and my uncles, grandparents and cousins, for showing unconditional support. But most importantly, and my biggest inspiration, is my aunt Nela. Not only was she always there for me, but she taught me that life should be taken lightly and with joy. I want to dedicate this work to her.

Resumo

Nesta dissertação, a fabricação de dispositivos óticos integrados em vidro borossilicato EAGLE2000 utilizando a técnica de escrita direta com laser femtossegundo (FLDW) foi amplamente explorada.

Esta técnica de microfabricação baseia-se no foco de um feixe laser no interior do substrato, onde mecanismos de absorção não linear promovem um aumento localizado do índice de refração, permitindo a criação de dispositivos capazes de guiar luz.

Neste trabalho, o principal dispositivo produzido com recurso a esta técnica é o interferómetro de Mach-Zehnder. Neste, a luz é injetada à entrada do dispostivo (fan-in), onde posteriormente é dividida por acopladores direcionais 50:50 em duas ondas de igual potência ótica. De seguida, um microaquecedor colocado diretamente acima de um dos braços do interferómetro, o qual aquece um dos braços mais do que o outro provoca, através do efeito termoótico, uma equivalente variação nos índices de refração nos braços, introduzindo uma diferença de fase entre estes. Por fim, outro acoplador 50:50 faz com que as duas ondas interfiram, dividindo a luz numa proporção que depende da diferença de fase introduzida pelo microaquecedor. As duas ondas podem então ser removidas do sistema através de um fiber-array de duas fibras.

A produção de MZIs de qualidade passou pela otimização de todos os seus componentes intermediários. Com base em trabalhos anteriores realizados no mesmo material [1], parâmetros como taxa de repetição [2] [3] [4] [5], abertura numérica da objetiva, polarização do feixe [6] [1] e profundidade de escrita [2] foram mantidos constantes.

Com o objetivo de minimizar as perdas de inserção, foram produzidos diversos guias de onda retos variando a velocidade de escrita e a energia dos impulsos laser. Uma análise às perdas (de acoplamento, propagação e inserção) e aos diâmetros dos modos dos guias em X e Y foi realizada e uma energia de impulso de 150 nJ e uma velocidade de escrita de 35 mm/s foram escolhidas para fabricações posteriores.

S-bends com diferentes raios de curvatura foram testados quanto às suas perdas de curvatura. Verificou-se que, a partir do raio de 70 mm, com perdas de curvatura de 3.83 dB, a diminuição de perdas de curvatura é desprezável, pelo que este raio de curvatura foi escolhido, por permitir uma maior densidade de integração, em comparação com raios maiores. Uma lei empírica que relaciona as perdas de curvatura por centímetro com o raio de curvatura também foi verificada [7].

Com o objetivo de produzir uma divisão de potência ótica da luz, especificamente uma

divisão 50:50, num design compacto e que proporcione repetibilidade, diversos acopladores foram testados variando a separação e comprimento dos guias na região de interação. Para cada separação, vários comprimentos de interação foram testados. A separação de 15 μm foi a que demonstrou um comportamento mais próximo do esperado, uma relação sinusoidal da refletividade com o comprimento da região de interação, que permitiu identificar uma fase (ϕ_0) introduzida pelas s-bends de 0.66 rads, um comprimento de acoplamento (L_c) de 3.2 mm e uma assimetria (Δ) dos guias de 0.091 rads/mm. Para produzir acopladores 50:50, um comprimento de interação (L_i) de 3.37 mm foi escolhido.

Para produzir os moduladores de fase térmicos, uma fina camada de ouro (100 nm) e crómio (5 nm) foi depositada na superfície do substrato de EAGLE2000 através da técnica de sputtering. Nesta camada, um microaquecedor foi produzido diretamente acima de um dos braços do interferómetro, de modo a garantir uma diferença máxima de temperatura entre braços, que se traduziu numa diferença de fase máxima. Os microaquecedores foram produzidos ”recortando” a sua forma na camada de ouro depositada utilizando o mesmo laser femtossegundo. Para que se garanta isolamento elétrico eficiente entre um lado e o outro do recorte, velocidade de escrita, energia de impulso e polarização do laser foram testados. Verificou-se uma independência do corte na polarização, e uma velocidade de escrita de 2 mm/s e uma energia de impulso de 1000 nJ foram escolhidos.

A resistência elétrica dos microaquecedores produzidos foi medida em relação à potência elétrica dissipada, e um comportamento aproximadamente linear foi observado [3].

A refletividade dos MZIs foi medida em relação à potência elétrica dissipada pelo microaquecedor. Obteve-se uma potência necessária para um período completo de modulação ($P_{2\pi}$) de 375.3 $\pm$ 0.1 mW. Introduzindo uma função degrau de tensão no microaquecedor, tempos de subida e descida de 24 ms e 32 ms, respetivamente, foram obtidos. A partir do tempo de subida, a largura de banda do sistema foi estimada, dando o valor de 14.58 Hz.

Para verificar se o ouro que rodeia o microaquecedor tem influência na eficiência do MZI, o mesmo dispositivos foi testado sem e com uma área de isolamento à volta do microaquecedor. Observou-se uma diminuição de $P_{2\pi}$ de 492.9 $\pm$ 0.05 mW para 451.76 $\pm$ 0.1 mW.

Palavras-chave: EAGLE2000, Femtosecond laser direct writing, Mach-Zehnder interferometers, Photonic integrated circuits, Thermal phase-shifter

Abstract

In this dissertation, the fabrication of integrated optical devices in EAGLE2000 borosilicate glass using the femtosecond laser direct writing (FLDW) technique was extensively explored.

This microfabrication technique is based on focusing a laser beam inside the substrate, where nonlinear absorption mechanisms induce a localized increase in the refractive index, allowing the creation of devices capable of guiding light.

Among the fabricated devices are straight waveguides, S-bends, directional couplers, and Mach–Zehnder interferometers (MZIs).

In the latter devices, light is injected at the input of the device (fan-in), where it is subsequently split by 50:50 directional couplers into two waves of equal optical power. Then, a microheater placed directly above one of the interferometer arms heats one arm more than the other, which, through the thermo-optic effect, induces an equivalent variation in the refractive indices of the arms, introducing a phase difference between them. Finally, another 50:50 coupler causes the two waves to interfere, splitting the light in a proportion that depends on the phase difference introduced by the microheater. The two output waves can then be extracted from the system using a two-fiber fiber array.

The production of high-quality MZIs required the optimization of all intermediate components. Based on previous work performed in the same material [1], parameters such as repetition rate [2] [3] [4] [5], objective numerical aperture, beam polarization [6] [1], and writing depth [2] were kept constant.

To minimize insertion losses, several straight waveguides were fabricated by varying the writing speed and the laser pulse energy. An analysis of coupling, propagation, and insertion losses, as well as of the mode field diameters in X and Y, was carried out, leading to the choice of a pulse energy of 150 nJ and a writing speed of 35 mm/s for subsequent fabrications.

S-bends with different curvature radii were tested for bend losses. It was found that, from a radius of 70 mm (with bend losses of 3.83 dB), the reduction in bend losses becomes negligible. Therefore, this curvature radius was chosen, as it allows higher integration density compared to larger radii. An empirical law relating bend losses per centimeter to the curvature radius was also verified [7].

To achieve optical power splitting—specifically a 50:50 split—in a compact and reproducible design, several couplers were tested by varying the separation and interaction length of the waveguides in the coupling region. For each separation, several interaction lengths were tested. The 15 µm separation exhibited the most expected behavior—a sinusoidal relationship

between reflectivity and interaction length—which allowed identifying a phase (ϕ_0) introduced by the S-bends of 0.66 rad, a coupling length (L_c) of 3.2 mm, and a waveguide asymmetry (Δ) of 0.091 rad/mm. To produce 50:50 couplers, an interaction length (L_i) of 3.37 mm was chosen.

To fabricate the phase shifters, a thin layer of gold (100 nm) and chromium (5 nm) was deposited on the surface of the EAGLE2000 substrate via sputtering. From this layer, a microheater was produced directly above one of the interferometer arms to ensure the maximum temperature difference between arms, resulting in a maximum phase difference. The microheaters were fabricated by "cutting" their shape into the deposited gold layer using the same femtosecond laser. To ensure efficient electrical isolation between the two sides of the cut, writing speed, pulse energy, and laser polarization were tested. It was found that the cutting process was independent of polarization, and a writing speed of 2 mm/s and a pulse energy of 1000 nJ were selected.

The electrical resistance of the fabricated microheaters was measured as a function of the dissipated electrical power, showing an approximately linear behavior [3].

The reflectivity of the MZIs was measured as a function of the electrical power dissipated by the microheater. A power of 375.3 ± 0.1 mW was required for a full modulation period ($P_{2\pi}$). When a voltage step function was applied to the microheater, rise and fall times of 24 ms and 32 ms, respectively, were obtained. From the rise time, the system's bandwidth was estimated to be 14.58 Hz.

To verify whether the gold surrounding the microheater influences the efficiency of the MZI, the same device was tested both without and with an isolation area around the microheater. A reduction in $P_{2\pi}$ from 492.9 ± 0.05 mW to 451.76 ± 0.1 mW was observed.

Keywords: EAGLE2000, Femtosecond laser direct writing, Mach-Zehnder interferometers, Photonic integrated circuits, Thermal phase-shifter

Contents

List of Figures

List of Tables

List of Abbreviations

CCD	Charge-coupled device
CPA	Chirped pulse amplification
EBL	Electron beam lithography
EDFA	Erbium doped fiber amplifier
EIC	Electronic integrated circuit
FLDW	Femtosecond laser direct writing
FWHM	Full width half maximum
LNOI	Lithium niobate on insulator
MFD	Mode field diameter
PIC	Photonic integrated circuit
RNF	Refracted near-field
SMF	Single mode fiber
TIR	Total internal reflection

1 Introduction

Until very recently, electronic integrated circuits (EICs) have been at the heart of the digital revolution, allowing for unforeseen breakthroughs in computing, information technologies and communications. Transistor integration density, however, is reaching its physical limits [8], and new solutions ought to be found for the ever-growing demand in data processing. To this end, photonic integrated circuits (PICs) have entered the scene as a potential candidate, leveraging light properties to realize high-speed, low-power and bandwidth-rich information processing [9]. Programmable PICs, in particular, are showing up as a versatile tool for realizing, on the same hardware, several optical signal processing tasks. These devices allow real-time manipulation of light through electrical control of light flow by means of, for instance, active modulation of available beam-splitters. This versatility is changing the paradigm in applications such as telecommunications, artificial intelligence, quantum and neuromorphic computing [10] [11] [12] [13]. PICs show several advantages over EICs, including low propagation losses, since light is not subject to resistive, inductive and capacitive losses [14] [15], higher bandwidths, operating at THz frequencies, the ability to perform wavelength-division multiplexing, allowing for the simultaneous processing of several light signals, and low latency, enabling ultra-fast processing [16].

Many programmable PICs rely on the Mach-Zehnder interferometer (MZI) as the main building block for several architectures. This device allows for precise control of light amplitude and phase, and when several are placed in cascaded meshes, any arbitrary unitary linear transformation can be performed [17], allowing for system reconfigurability, valuable in machine learning algorithms [18], namely through the Reck/Clements architectures [17] [19].

The choice in fabrication method will also influence the complexity and quality of produced optical devices. Traditional photolithography, despite being a well-established method for PIC production, enabling high scalability and a strong integration with existing electronic technologies, device fabrication involves multiple steps, cleanroom facilities and do not allow for true 3D structures. Figure 1.1 shows a typical photolithography method employed in PIC production.

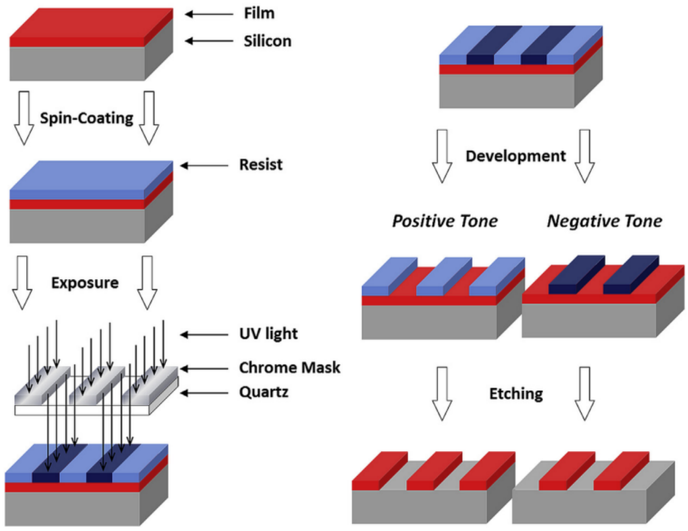

Figure 1.1: Typical photolithography production process [20].

Femtosecond laser direct writing (FLDW) is an alternative approach that leverages ultra-short, high power laser pulses to induce non-linear absorption processes inside a transparent material, inducing changes in the material's properties, namely the refractive index [21] [22]. By translating the substrate, true 3D structures can be created, all in a single step [23]. Waveguides produced using this method possess a more circular refractive index cross-section, which translates into smaller coupling losses when compared with the rectangular cross-section produced by photolithographic methods [24], which demands the introduction of tapers/spot-size converters. The smooth refractive index modification naturally produced by this method also allows reaching propagation losses as low as 0.07 dB/cm in glass [25]. FLDW can also be applied to a myriad of materials, ranging from polymers, to crystals, polycrystalline ceramics and glasses [26] [27].

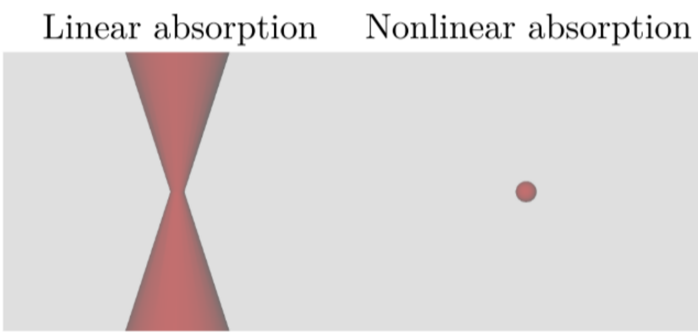

Figure 1.2: Linear vs non-linear light absorption in the FLDW technique. Comparison between linear absorption, typically seen in continuous wave (CW) lasers, and non-linear absorption found in FLDW. Schematic taken from [28].

One downside to this method resides in its serial nature, contrary to the inherent parallel processing capabilities of photolithography, allowing for much higher throughputs. This highlights the importance of fabrication speeds. Fused silica, being one of the main materials used together with FLDW, possesses writing speeds in the order of 0.05 cm/s [29]. On the other hand, borossilicate glasses like EAGLE2000, the material used in this work, enables writing speeds up to 12 cm/s [30].

In this dissertation, several optical devices produced in EAGLE2000 glass using the FLDW technique will be studied, with the final goal being the production and optimization of MZIs, the building block of programmable PICs.

In chapter 2, some PIC fabrication methods will be discussed, including photolithography and FLDW, as well as some materials typically employed in PIC fabrication. A theoretical explanation of the workings of a femtosecond laser unit will also be given, as well as its interaction with several transparent materials, focusing on EAGLE2000.

In chapter 3, specifications about the femtosecond laser writing system employed in this work will be given. The process used for polishing the substrate surfaces to achieve optical quality is also described. The method employed for device characterization is depicted, as well as a circuit that was devised to allow automatic alignment of the fibers with the optical devices.

In chapter 4, several fundamental optical devices will be explored, including straight waveguides, s-bends and directional couplers. Their working principles, fabrication and light-guiding properties will be studied, with the main objectives being low insertion losses, compactness and repeatability.

In chapter 5, the thermal phase-shifters essential to the production of MZIs will be studied, including an analysis of FLDW ablation on a gold and chromium layer deposited on top of the optical substrate. Finally, the Mach-Zehnder interferometers are fabricated and thoroughly studied for their behavior, including modulation amplitudes, rise and fall times, and electrical power dissipated to produce a 2π phase-shift, with the main objective being minimizing the latter. To this end, the introduction of an isolation layer around the phase-shifter is also studied for its influence on power efficiency.

1.1 List of Presentations

My work has been selected for presentation at the **Doctoral Congress on Engineering (DCE25)**.

2 Femtosecond Laser Direct Writing

In this chapter, the FLDW technique will be thoroughly explained. A brief introduction to laser generation and its properties will be given, followed by an analysis of laser focusing inside of a substrate, the mechanisms of laser-matter interaction and resulting mdifications. Several modification regimes are analyzed, followed by the effect of repetition rate on material modification. Longitudinal and transverse writing configurations are compared and, finally, some writing geometries made possible with the transverse writing configuration are compared.

2.1 Laser Theory

To comprehend the physics underlying FLDW, understanding how the laser is generated and turned into femtosecond pulses is essential. A laser is a device that produces a coherent, monochromatic and collimated beam of light through the process of stimulated emission of radiation. The formation of a laser beam is achieved in a laser cavity containing a gain medium. Inside this cavity, photons are only allowed to oscillate along the cavity modes, which restrain the photons to a narrow frequency range. Initially, energy accumulates on these cavity modes through spontaneous emission of radiation and, when population inversion is achieved, stimulated emission of radiation takes over and light amplification is achieved [31].

2.1.1 Ultrashort Pulse Generation

Modes inside the cavity oscillate asynchronously and the output light consists on a continuous wave (CW) composed of the frequencies of the various cavity modes. With mode-locking, the temporal phase of some or all of the modes is synchronized, leading to the formation of ultrashort bursts of high intensity light. Mode-locking can be achieved by inserting elements which lock the modes inside the cavity, such as optical modulators, saturable absorbers (passive mode-locking) or by using a mode-locked pump laser (active mode-locking) [32]. These methods, however, are not able to produce high intensity pulses. To further increase intensity and reduce the pulse duration to the femtoseconds, Chirped Pulse Amplification (CPA) is usually employed [33] [34]. After the pulse leaves the lasing cavity, it passes through a stretching component, usually grating-based stretchers, dispersion fibers or prism pairs, which extend the pulse in time, but also lowers the peak intensity, preventing any damage on subsequent optical components. Afterwards, an amplification stage, like an Erbium-Doped Fiber Amplifier (EDFA) increases the pulse energy by 10^6 to 10^9 times before a compressor shortens the pulse to the femtosecond duration (fig. 2.1) [35].

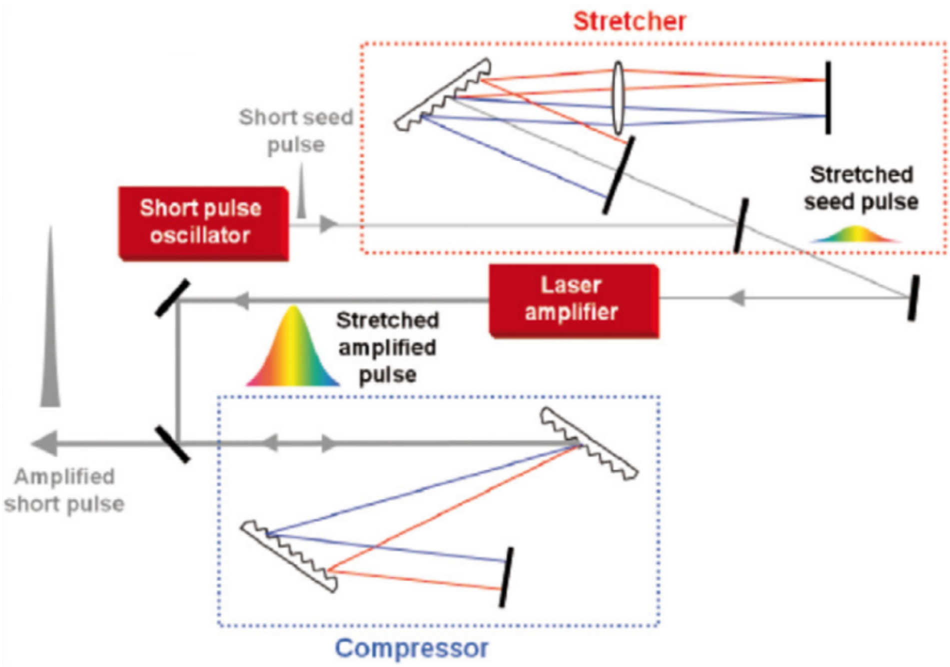

Figure 2.1: Schematic representation of Chirped Pulse Amplification (CPA) [32].

The FLDW unit used in this work can produce pulses with a maximum energy of 11.4 μJ, and a minimum pulse duration of 248 fs (FWHM) (see table 3.1). Since this pulse possesses an approximately lorentzian shape, the maximum peak power achievable by this laser is 28 MW.

2.1.2 Gaussian Beams

Although a femtosecond laser is made of a series of ultrashort bursts, their spatial distribution can still be described, in the paraxial regime, by a gaussian beam.

$$I(\rho, z) = I_0 \left(\frac{\omega_0}{\omega(z)}\right)^2 \text{exp}\left(-\frac{2\rho^2}{\omega^2(z)}\right) \tag{2.1}$$

Here, z is the distance along the optical path, the focus being at $z = 0$,and ρ is the distance from the optical axis. I_0 is the intensity at the point $(0, 0)$, ω_0 is the waist radius at the focus, and $\omega(z)$ is the waist radius at any distance z, being described by:

$$\omega(z) = \sqrt{1 + \left(\frac{z}{z_0}\right)^2} \tag{2.2}$$

, with z_0 being the Rayleigh range, corresponding to the distance from the focus along the optical axis for which $\omega(z) = \sqrt{2}\omega_0$. It is also expressed as:

$$z_0 = \frac{\pi n \omega_0^2}{\lambda} = \frac{1}{2} b \tag{2.3}$$

, λ being the wavelength, and b the confocal parameter.

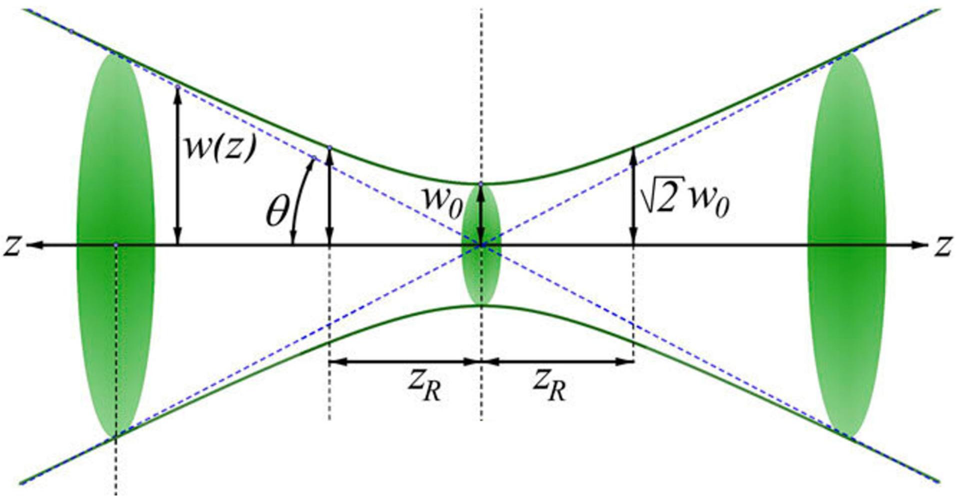

Figure 2.2: Schematic representation of a gaussian beam.

2.1.3 Focusing Inside the Material

In order to achieve the necessary intensities for nonlinear absorption, while also reaching small spot sizes, the laser is focused inside the material using an objective lens. Since the laser employed has a bandwidth of around 9 nm, chromatic aberrations can be neglected, however, spherical aberrations are still an issue that must be addressed. When using spherical lenses, light rays closer to the optical axis focus further than rays at the edges. This problem is solved by employing an aspherical lens. Unfortunately, light is focused inside a material passing through an air-material interface, where another refraction, once again, changes the beam focus. As a result, FLW written structures depend on both inscription depth and numerical aperture.

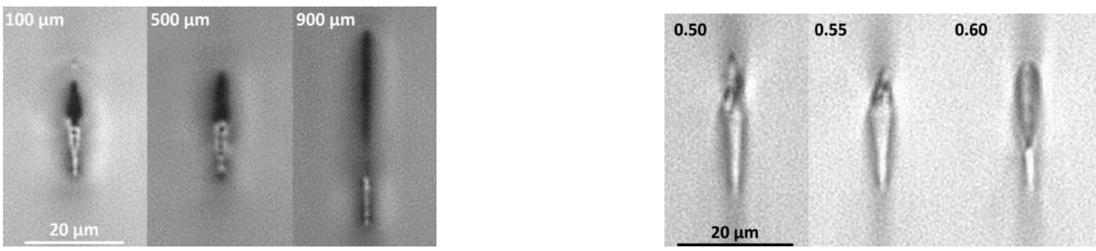

Figure 2.3: Cross-section view of waveguides inscribed in Suprasil 1. Pulse energy and writing velocity fixed at 200 nJ and 100 μs^{-1}. **left:** Dependence on written structures with inscription depth; **right:** Dependence on written structures with NA [2]

.

The feature sizes of the focal volume can be characterized by knowing the diffraction-limited minimum waist radius (ω_0) and the Rayleigh range (z_R), given by [36]:

$$\omega_0 = \frac{M^2\lambda}{\pi NA} \tag{2.4}$$

$$z_0 = \frac{M^2 n\lambda}{\pi NA^2} = \omega_0 \frac{n}{NA} \tag{2.5}$$

, where M^2 is the beam quality factor, and λ is the laser wavelength in vacuum. From the system parameters (NA = 0.42, λ = 515 nm, M^2 = 1.12), we obtain ω_0 = 437 nm and z_0=1,58 μm. This focal volume, however, does not correspond to the modified volume. Indeed, as will be seen in section 2.2.4, the high repetition rates used in this work (1 MHz) places the modifications in a heat accumulation regime, where heat from the laser energy does not have enough time to dissipate out of the focal volume, modifying surrounding material, effectively increasing the modified cross-section [5].

Another issue to account for is the fact that a change in the distance between the lens and the air-material interface does not correspond to a similar change in the focusing depth. Knowing that the refractive index of the substrate is higher than that of air, the laser will focus deeper than it would without the substrate. To relate the focusing depth with (z') and without the substrate (z), formula (2.6) is used:

$$z' = z\frac{n''}{n'}\sqrt{1 + \frac{(n''^2 - n'^2)NA^2}{(n''n')^2 - (n''NA)^2}} \tag{2.6}$$

The indices n" and n' correspond to the substrate and air refractive indices, respectively.

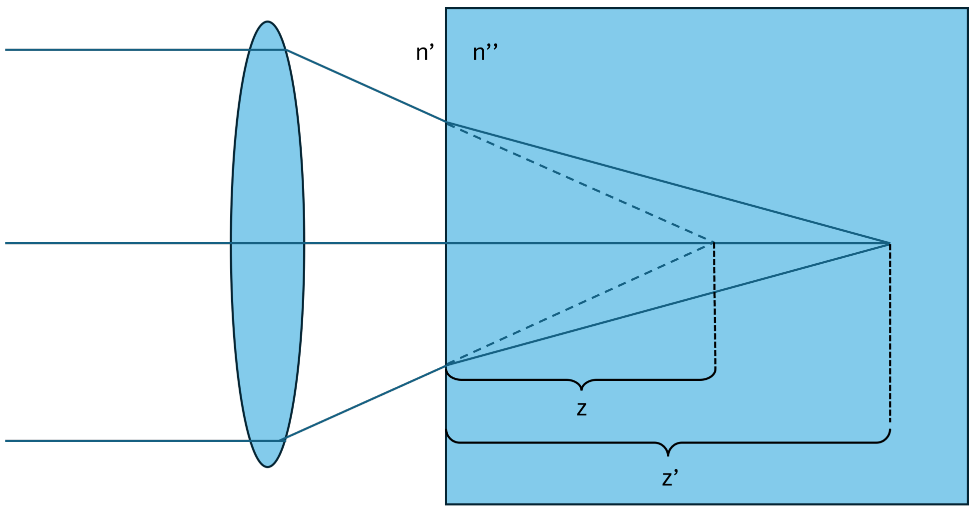

Figure 2.4: Laser focusing inside a substrate.

An approximation to this equation is made to simplify the calculations.

$$z' = z\frac{n''}{n'} \tag{2.7}$$

Knowing the values of n' and NA, this approximation introduces an error of ≈ 10%, meaning that, for instance, if this formula is used to focus the laser at a depth of z' = 50 μm, the modification will in reality be at z' = 55 μm. Nevertheless, this difference is not important and can be neglected.

2.1.4 Self-focusing

When working with high intensities, nonlinear material responses must be taken into account. Since EAGLE2000 is a glass, it is centrosymmetric, meaning that $\chi^{(2)} = 0$. Furthermore, susceptibilities higher than the third order can be considered negligible, leaving us with an expression for the polarization vector:

$$\mathbf{P} = \epsilon_0 \left[\chi^{(1)} + \frac{3}{4}\chi^{(3)}|\mathbf{E}|^2\right] \mathbf{E} \tag{2.8}$$

This relation can be represented in terms of the refractive index n, through the following relation:

$$n = \sqrt{1 + \chi^{(1)} + \frac{3}{4}\chi^{(3)}|\mathbf{E}|^2} \approx n_0 + n_2 I \tag{2.9}$$

Here n_0 is the usual linear refractive index, approximated by $n_0 = \sqrt{1 + \chi^{(1)}}$, $n_2 = \frac{3\chi^{(3)}}{4\epsilon_0 c n_0^2}$ is the nonlinear refractive index, and $I = \frac{1}{2}\epsilon_0 c n_0^2 |\mathbf{E}|^2$ is the light intensity.

When the laser is focused inside the substrate, the intensity near the optical axis is higher than on its boundaries, leading to a higher refractive index change in the laser's core. This refractive index gradient, provided that n_2 is positive, acts as a convergent lens, leading to self-focusing of light, further increasing the light intensity at the optical axis. Self-focusing is achieved when a minimum critical power is reached, being given by:

$$P_{cr} = \frac{3.77\lambda^2}{8\pi n_0 n_2} \tag{2.10}$$

For Corning 0211, a borosilicate glass close in composition to EAGLE2000, the critical power for the 515 nm wavelength was estimated to be $\approx$ 0.7 MW, based on [37]. Thus, to avoid self-focusing, laser peak powers must not exceed this value.

2.2 Laser-induced material modifications

When a laser is focused on materials transparent to its wavelength, linear absorption on itself does not enable light absorption, since the bandgap exceeds the photon energies. However, there is a region around the focus where laser intensity is high enough so that non-linear absorption phenomena start to occur. In this region, the laser beam produces an electric field in the same order of magnitude of that binding the valence electrons to their atoms , which corresponds to a laser intensity in the TW/cm^2 order [38] [21]. These high intensities are achieved by combining tight focusing and the high peak powers achieved by femtosecond laser pulses, which, as it was seen before, can reach peak powers in the MW order.

2.2.1 Photon Absorption

High intensity light can be absorbed by the material by multiphoton absorption or tunneling ionization [39].

The first process occurs when a single electron absorbs multiple photons of light simultaneously, provided there is a high enough intensity [40]. When the sum of the simultaneously absorbed photons exceeds the bandgap of the material, the electron jumps to the conduction band.

In tunneling or Zener ionization, the high electric field generated by the laser beam deforms the potential barrier between the valence and conduction bands, allowing for electrons to quantum tunnel into the conduction band.

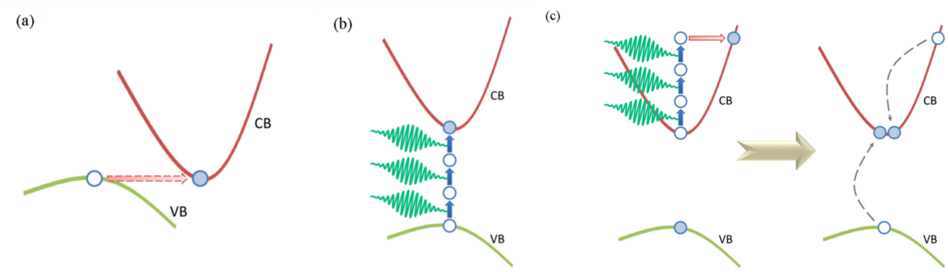

Figure 2.5: Nonlinear absorption processes present in FLDW. **a)** Tunneling/Zener ionization; **b)**Multiphoton absorption; **c)** Avalanche ionization [41].

These two processes can happen simultaneously, however one of them is often times dominant. Multiphoton absorption, for instance, is more expressive for lower peak intensities and higer frequencies, since less photons are required to jump an electron to the conduction band. Tunneling ionization benefits from higher intensities and lower frequencies, since a higher deformation of the potential barrier is achieved this way. The Keldysh parameter, γ, quantifies the degree of dominance of either process.

$$\gamma = \frac{\omega}{e}\sqrt{\frac{m_e c n \epsilon_0 E_g}{I}}$$

In this equation, m_e and e correspond to the electron mass and charge, n is the linear refractive index, E_g is the bandgap energy, ω is the laser frequency and I is the laser intensity at the location of the process.

If $\gamma \ll$ 1.5, then the dominant mechanism is tunneling ionization; when $\gamma \gg$ 1.5, multiphoton absorption is, instead, the most common process; when this value is close to 1.5, both processes occur with similar predominance. For the configuration at hand, $\gamma \approx 1.82$, meaning that no process dominates over the other and both contribute to photon absorption.

After electrons reach the conduction band, they can acquire more energy through free carrier absorption, as depicted in c) of figure 2.5. After absorbing energy from several photons, this extra energy can be higher than the bandgap of the material, and a collision from this electron with a valence band electron can promote it to the conduction band, leaving the two electrons at the conduction band minimum. This process is known as impact ionization, and it can grow exponentially as more electrons in the conduction band become available to be excited and collide with other electrons in the valence band, leading to avalanche ionization, a process that is described by the following equation:

$$\frac{dN}{dt} = \alpha I N \tag{2.11}$$

With N being the carrier density, α being the avalanche ionization coefficient, and I the laser intensity. This process can only occur if a minimum number of seed electrons are already present in the conduction band, which can be produced from impurity or defect states, or by the aforementioned multiphoton absorption and tunneling ionization.

2.2.2 Free Electron Plasma Formation

After a significant number of carriers reaches the conduction band, the electron density increases until it reaches the critical density for plasma formation $n_c = \frac{m_e \epsilon_0 \omega^2}{e^2}$, and thus a plasma is formed in the affected region, vibrating at a frequency $\omega_p = \sqrt{\frac{e^2 N}{\epsilon_0 m_e}}$. This plasma coexists with the lattice and if N increases to the point where ω_p reaches the laser frequency, plasma and laser resonate together [42], with power being transferred to the lattice through carrier-phonon scattering. Energy traded between the carriers and lattice reaches an equilibrium after several picoseconds, longer than the duration of the pulse. This means that the absorption is decoupled from lattice heating, which translates into deterministic breakdown, allowing for more precise machining when compared to longer pulses. The fact that nonlinear absorption processes are highly dependent on the bandgap of each material leads one to think that the threshold intensity (I_{th}) required for these processes to happen would vary greatly with E_g, however, experimental results show that I_{th} only varies very slightly with E_g, since most of the absorption process occurs through avalanche ionization, which depends linearly with I. This result further reinforces the idea that FLDW can be employed in a wide range of materials [21].

2.2.3 Modification regimes

The mechanisms by which electron energy is transferred to the lattice and the material modifications resulting from this interaction are not completely understood, however, the observed modifications can be grouped in three regimes: I, II and III.

In **regime I**, a smooth and uniform refractive index modification is observed, due to a combination of stress-induced changes, densification, colour-centre formation, and changes in effective fictive temperature, depending on the material system under investigation [32].

In **regime II**, organized birrefringent sub-wavelength optical nanogratings are formed [43].

When high power pulses focus on a transparent dielectric material, they produce localized inhomogeneous nonlinear multiphoton ionization at defects or color centers, producing hot-spots. When a spot is hit once, a memory effect leads to an increase of the ionization rate, making it so the next pulses ionize the same spot more easily. The hot-spots then evolve into spherically-shaped nanoplasmas with a density n_e smaller than the critical density n_{cr}, which, due to field enhancement at the boundaries of the nanoplasma, grow asymmetrically in a direction perpendicular to the laser polarization, forming plasma disks as n_e approaches n_{cr}, which turn into plasma nanoplanes. Eventually, the electron plasma density in the nanoplanes exceeds n_{cr}, point at which they become quasi-metallic, influencing light propagation in a way such that it only promotes nanoplane growth at an inter-plane spacing of $\lambda/2n$. (Fig. 2.6) There is very little research on nanogratings in EAGLE2000 glass, however, the formation of such structures has been found in several borossilicate glasses, such as Borofloat, [44] [45], Schott AF 32 and EAGLE XG [46].

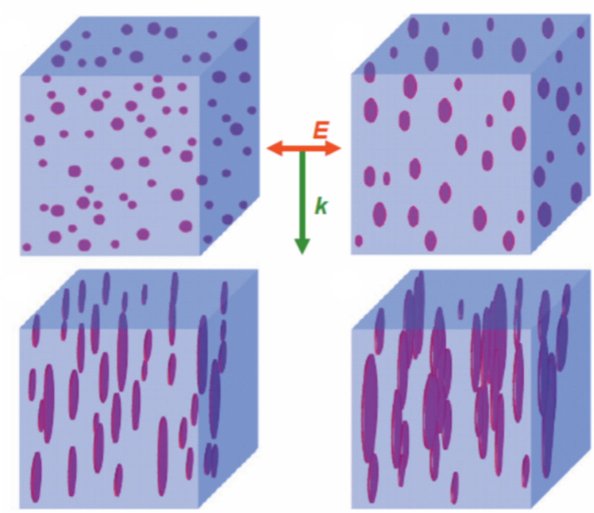

Figure 2.6: Various phases involved in nanograting formation [47].

Regime III is obtained when the laser pulse energy is increased to the point where the plasma energy becomes high enough such that ionic shielding is reduced, causing Coulomb repulsion between ions. These repulsions, together with the high temperatures and pressures, result in shock waves and densification, resulting in microexplosions that leave a less dense or hollow core surrounded by a region of higher density [48] [49] [50]

The particular modification regime is governed by exposure parameters, such as pulse energy, duration, repetition rate, wavelength, polarization, focal length, writing speed, and others, but also on the material properties, including bandgap, thermal conductivity, and others [36].

Although all of these modification regimes have been observed for many different materials, namely fused silica glass, to the best of my knowledge, mainly the first and third regimes have been observed for EAGLE2000 glass.

2.2.4 Effect of repetition rate on material modification

In section 2.2.3, we saw how several parameters can influence the modification regime of a material. A study of particular relevance is the dependence on the material modification on the laser repetition rate. At low repetition rates (1 - 200 kHz), heat diffusion modifies the area around the focal volume. Increasing the beam intensity results in an increase of this area [51]. Since the material is isotropic, the modified region will also become more isotropic as this energy increases. As repetition rate increases, the duration between pulses decreases, and heat starts accumulating at the focal volume, which begins to act as a point source of heat [52]. By keeping the net fluence constant, with a laser power of $\approx$ 200 mW and a writing speed of 25 mm/s, and changing the repetition rate from 200 kHz to 2 MHz, Eaton et al. [5] showed that waveguides with similar diameters were formed, and that generally for higher repetition rates, lower insertion losses of produced waveguides were observed, with 1.5 MHz providing the lowest IL.

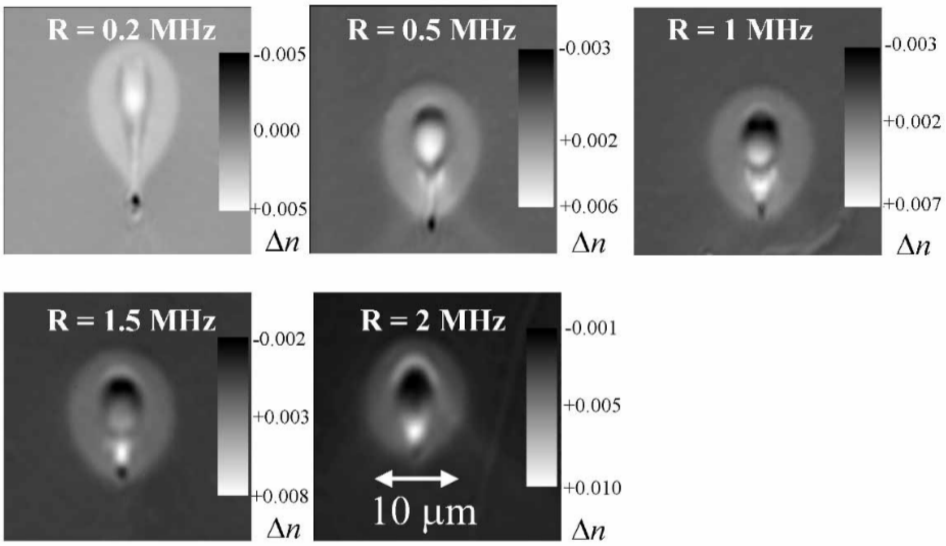

Figure 2.7: Cross-sectional profiles from refracted near-field (RNF) measurements of waveguides produced in EAGLE2000 glass by varying the laser repetition rate and keeping the net fluence constant [5].

The core structure is due to the high temperature laser impacts on the focal volume, while the cladding is attributed to a more slowly evolving gaussian temperature distribution. The size of the modification can be described as the area at which the temperature exceeded the melting point of the material.

Alexander Arriola et al. [53] found that introducing an annealing step after the production of multimode waveguides generates monomode waveguides with high refractive index contrasts ($\Delta n = 8.4 \times 10^{-3}$), enabling small s-bend radii.

2.2.5 Writing configurations

One of the main advantages of FLDW is the ability to produce arbitrary 3D structures inside a transparent material by translating it in relation to beam focus. To this end, one can employ longitudinal or transversal writing configurations. On the longitudinal configuration, the substrate is translated parallel to the beam incidence. Since the beam possesses a gaussian transversal profile, waveguides formed using this method exhibit a cylindrical geometry, allowing for waveguides with a circular cross-section. This technique, however, is limited by the working distance of the employed lens and it can only be used with the substrate translating downwards, since otherwise the modified structures would alter the beam path, focusing it in undesired spots. The transverse configuration, on the other hand, involves translating the substrate perpendicular to the laser focus, offering much greater freedom in waveguide writing, even though the cross-section ceases to be radially symmetrical.

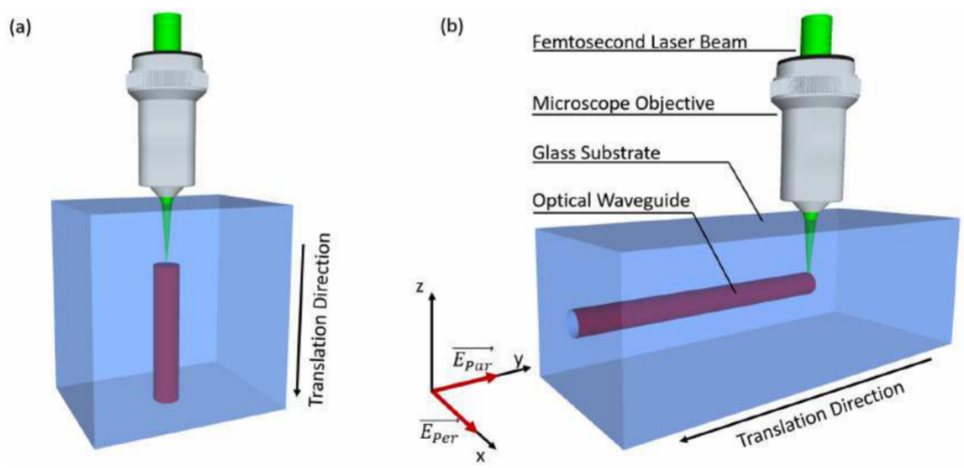

Figure 2.8: Different writting configurations. **a)** Longitudinal configuration; **b)** Transversal configuration [2].

2.2.6 Laser inscription geometries

Waveguide fabrication can be done in several different ways, depending on whether the refractive index modification induced by the laser is positive or negative. The first and most common waveguide is that where the laser alters the core of the material, increasing its refractive index, consisting in a Type I waveguide (fig. 2.9 (a)). By leaving the core unaltered and inscribing tracks on two opposite sides, the stress induced by those tracks changes the refractive index of the core through the strain-optic effect (fig. 2.9 (b)) [54]. If laser inscription produces a negative refractive index change, the cladding has to be written instead of the nucleus, being referred to as the depressed cladding structure (fig. 2.9 (c)) The two latter structures have the additional advantage of allowing for core size control, enabling extension of the cut-off wavelength, widening the range of usable wavelengths with respect to the first type of structure. The main advantage of the second structure when compared to the third is its easier production, with only two tracks being needed for light guiding.

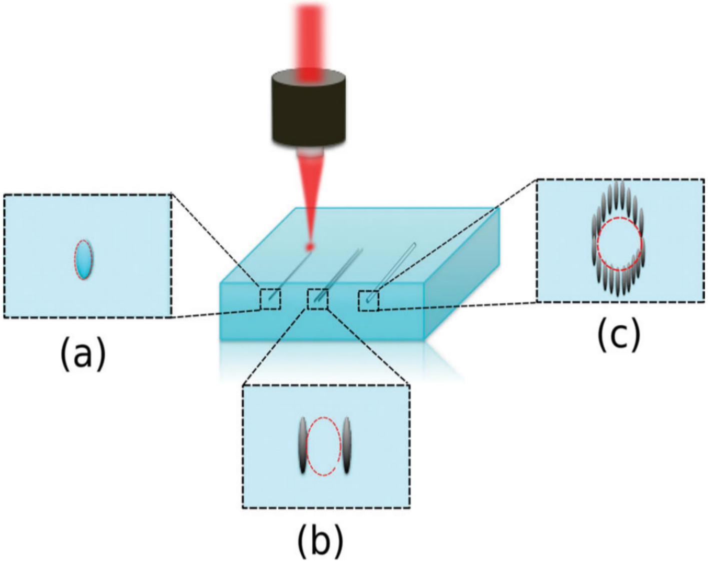

Figure 2.9: Different inscription geometries. **a)** Positive core modification (Type I waveguide); **b)** Waveguide produced by stress induced by two parallel tracks; **c)**Depressed cladding structure.

3 Fabrication and Characterization

A brief introduction to the laser system employed in this work is given, as well as the optical system used. The method followed for laser calibration is explained. The substrate polishing procedure is described, followed by an explanation of the alignment setup used in characterizing the optical devices. A homemade automatic alignment system is also described.

3.1 Femtosecond Laser Direct Writing Unit

The femtosecond laser system used throughout this work is a Satsuma HP fiber-amplified laser from Amplitude Systèmes. This laser is capable of generating sech^2 pulses with a FWHM of 248 fs at a repetition rate of 1 MHz with a maximum pulse energy of 11.4 μJ, possessing a polarization contrast of 1200:1.

This laser has a fundamental wavelength of 1030 nm, being able to generate a second harmonic of 515 nm, and a third harmonic of 343 nm. Throughout this work, only the second harmonic will be used, and the parameters specific to this wavelength are depicted in table 3.1. These values were obtained from the last certificate of conformance performed on 13/4/2025.

Parameter	Specifications
Center Wavelength	515 nm
Repetition Rate	1 MHz
Beam Quality, $M^2(X,Y)$	(1.12-1.13)
Beam Diameter ($1/e^2$) (X, Y)	(1.97,2.08) mm
Beam Divergence (X, Y)	(0.69,0.75) mrad
Ellipticity (%)	7
Pulse Duration	248 fs
Maximum Average Power	5.7 W
Maximum Pulse Energy	11,4 μJ

Table 3.1: Parameters of the Satsuma HP fiber-amplified laser.

After being generated, the fs-laser firstly passes through a beam expander that collimates it, decreasing the inherent beam divergence associated with the system, while also allowing for a better usage of the entrance pupil of the writing objective, effectively maximizing the numerical aperture. It then goes through a periscope system that raises the laser beam into the main optical circuit schematized in figure 3.2. Next, it goes through a power control unit (Watt Pilot from Altechna, fig. 3.1) constituted by a half-wave plate that rotates the polarization direction of the laser and two Brewster type thin film polarizers. The two thin films are placed at an angle that completely reflects the s-polarized light and transmits the p-polarized light. As the half-wave plate is rotated, the proportion of s and p-polarized light in the laser can be increased or diminished, allowing for a change in optical power emerging from the attenuator. The transmitted p-polarized light offers more power, although it comes with some s-polarized light. On the other hand, reflected s-polarized light suffers two reflections, hence having a much higher polarization contrast in comparison with transmitted light, despite having less power. For that reason, s-polarized light was chosen, with p-polarized light being discarded in a beam dump.

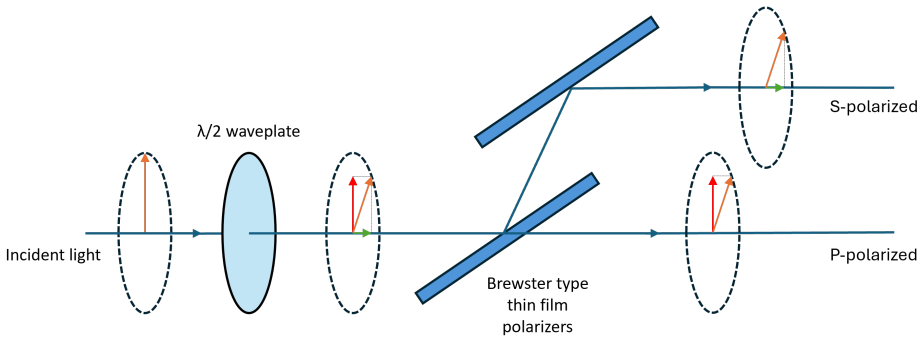

Figure 3.1: Working principle of the power control unit.

A half-wave plate is used to control the beam polarization, being controlled by the SCA software. A dichroic mirror is used to reflect the laser onto the objective, while also transmitting light from the substrate to a CCD camera, which allows visualization of the whole process. Light from a small laser placed besides the camera can also be transmitted. After the dichroic mirror, light enters a MituToyo M plan APO NIR 50x, an aspheric objective lens with a numerical aperture of 0.42 and a working distance of 17 mm, where it is focused on the substrate to be machined. Throughout the whole optical circuit, variable iris apertures were placed between each optical component, ensuring the correct propagation of the beam.

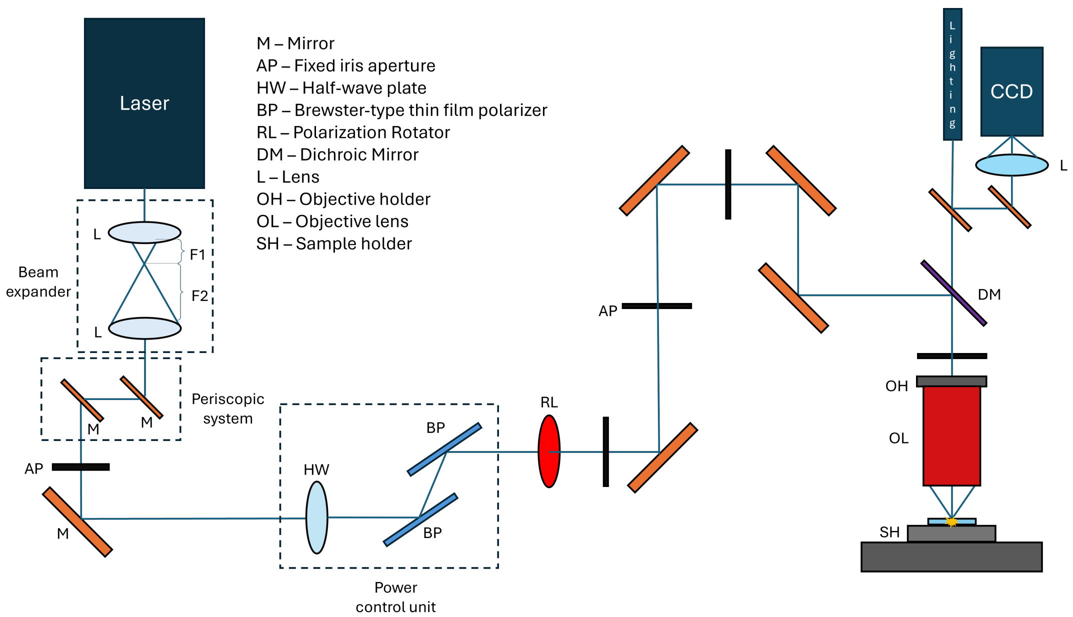

Figure 3.2: Femtosecond laser direct writing workstation.

The substrate is positioned on top of a stainless steel platform which is connected to a vacuum pump that, when activated, produces a downward force on the sample, fixing it in place. This platform is in turn fixed on top of a translation stage (Aerotech ANT130V5 - PLUS), which allows translation on the Z direction with a travel range of 5 mm, an accuracy of $\pm$ 200 nm and a resolution of 2 nm. The whole apparatus is on top of a set of two translation stages that move in the X and Y directions (Aerotech ANT130XY-110 PLUS). The travel range of the stages is of 110 mm, with an accuracy of $\pm$ 300 nm and a resolution of 1 nm, being able to achieve an acceleration of 500 mm/s^2.

3.2 Laser calibration

Before writing, laser power and polarization must be calibrated. Beam polarization is controlled by a λ/2 waveplate present on the system. Rotation of this waveplate can be done through the SCA software. To get a rough estimate of polarization direction, a polarizing filter is placed on top of a luminescent card, both farther away from laser focus, so that a better visualization of the beam is achieved. Since for all writing procedures the polarization will be kept on the X direction, which corresponds to the writing direction, the polarizing filter axis was oriented to roughly match the Y direction, so that the desired polarization corresponds to a minimum in brightness. Since the human eye is better at detecting changes in light at small intensities rather than at high intensities [55], this configuration allows for a more precise polarization adjustment. This way, the polarization is adjusted on the software until minimum brightness is achieved (total darkness is not achieved since a small portion of p-polarized light always passes through the attenuator). Average laser power must also be determined before any writing can be done. This step has to be done every time the laser is turned on, since even ambient temperature variations can affect laser power. To this end, a powermeter is employed to measure the output power of the laser after passing through the system. To modulate laser power, the SCA software allows rotation of the half-wave plate before the Brewster-type thin films. Since the powermeter can only detect powers up until roughly 50 mW, care must be taken in choosing the value of light passing through the modulator. Since the software works by choosing the percentage of light passing through the modulator, we started by measuring the output power corresponding to 0%, increasing in steps of 0.5 % until near maximum power is reached. Figure 3.3 shows the laser output power as a function of transmission percentage on the modulator.

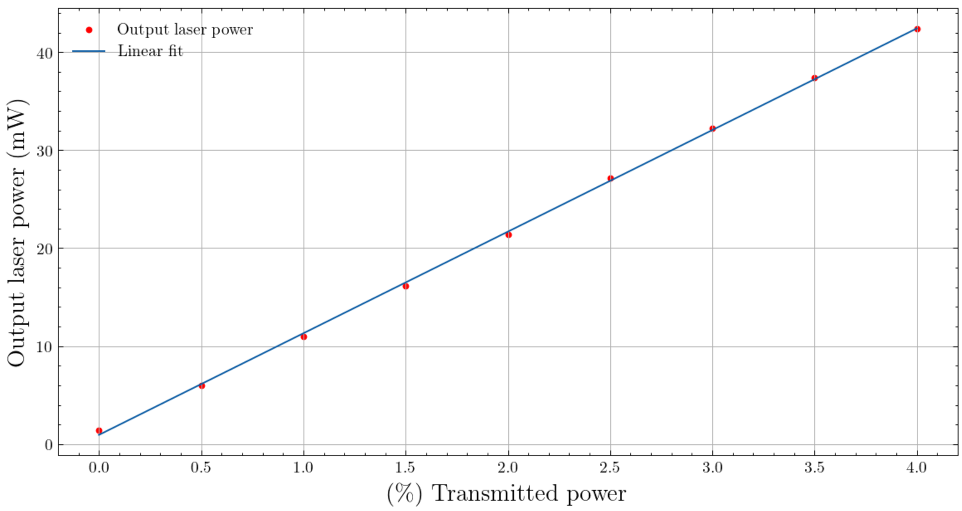

Figure 3.3: Calibration of laser output power.

As expected, the graph follows a quasi-linear behavior, meaning that the desired power can be well approximated by a linear fit. Since the parameter of relevance in altering a material is the pulse energy, knowing the repetition rate (R), the desired pulse energy (E) can be selected by actuating on laser output power (P). The formula that relates the two is the following:

$$P = ER \tag{3.1}$$

This way, to choose the desired pulse energy, this equation allows finding the correspondent output power, and through the linear adjustment made on the above graph, the corresponding transmitted power is introduced in the software.

3.3 Polishing Procedure

After producing the waveguides, the substrate side facets upon which they will be coupled to the measuring system have to be polished for two reasons: first, the substrate surfaces do not have optical quality, possessing a rough surface; and second, when the writing laser focus reaches the borders, it suffers from border effects, where the part of the laser that does not pass through the substrate focuses below, inherently producing a different refractive index cross-section, increasing losses. Fig. 3.4 illustrates the effects of polishing the surfaces. The polishing procedure is described below.

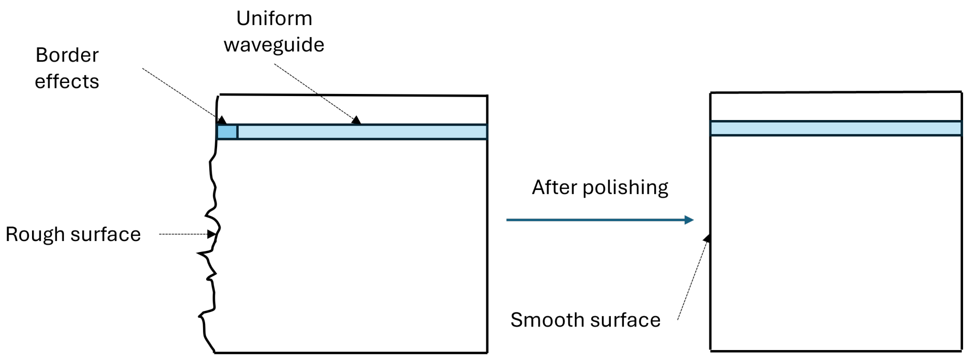

Figure 3.4: Effects of polishing in removing surface roughness and border effects from the side facets.

The glasses going into the jig consist of the substrate, a support glass that is polished on one side and two alignment glasses. The assembly is placed on a hot plate and heated up to around 150 ºC. When the support glass is hot, OCON-199 bonding wax is spread across all of the top surface until the wax liquefies. The substrate is carefully placed on top of the support glass, avoiding bubble formation, and, by using the alignment glasses, the surface to be polished is aligned with a side facet of the support glass. The hot plate is turned off and the whole assembly is left to cool down for 45 minutes. When the wax is solidified, the alignment glasses are carefully removed, and the excess bonding wax is scraped off of all surfaces except the substrate. The jig is cleaned with water and it is placed on the first polishing plate with a solution of silicon carbide (600 μm) slowly dripping for 10 minutes. This step is made to ensure all rust and contaminants are removed from the plate before the substrate assembly is placed. Afterwards, the jig is removed from the plate and the substrate assembly is positioned on the jig by gently tightening the positioning screw. The jig and substrate are cleaned with water and the plate is made to spin at a very slow speed while the silicon carbide solution is provided. While the plate is kept at a low speed (5 rpm), the assembly is slowly placed on the plate while making sure the jig rotates without resistance and no screeching sound is audible, which could indicate substrate scratching. Plate speed is slowly raised to 20 rpm, while listening for unusual sounds. When the final speed is reached, a dripping rate of 3 drops per plate rotation ensures that the substrate does not scratch directly against the dry plate, which could produce damage. After 45 minutes, the jig is carefully removed, rinsed, and the polished surface is observed at the microscope to look for defects. If the substrate shows any imperfections, it is placed 10 more minutes on the first plate and checked again. This process is repeated until a uniform and defect-free surface is observed. Just like the first plate, a second jig is placed on the second plate with a solution of aluminum oxide (3 μm) for 10 minutes to remove all contaminants and rust. This second jig is then removed and rinsed and the main jig is slowly placed on the second plate in a similar way to the first plate, carefully and slowly raising the plate speed to 20 rpm.

Again, a dripping rate of 3 drops per plate rotation is ensured and the substrate is left to polish for 90 minutes. In the end, the jig is removed, cleaned and observed for imperfections. The third and final plate is rinsed with water and a Logitech polishing suspension type SF1 is made to drip on the surface. All previous steps for placing the jig are followed, only now the polishing speed is of 18 rpm. After letting the substrate polish for 90 minutes, the jig is again removed, cleaned and verified a final time. The surface should be completely transparent and presente no imperfections. The support-substrate assembly is carefully removed from the jig and placed on the hot plate along with the alignment glasses, which is heated up to 150ºC in order to liquify the wax. The substrate is turned 180º to expose the other surface to polish and all the previous steps are repeated.

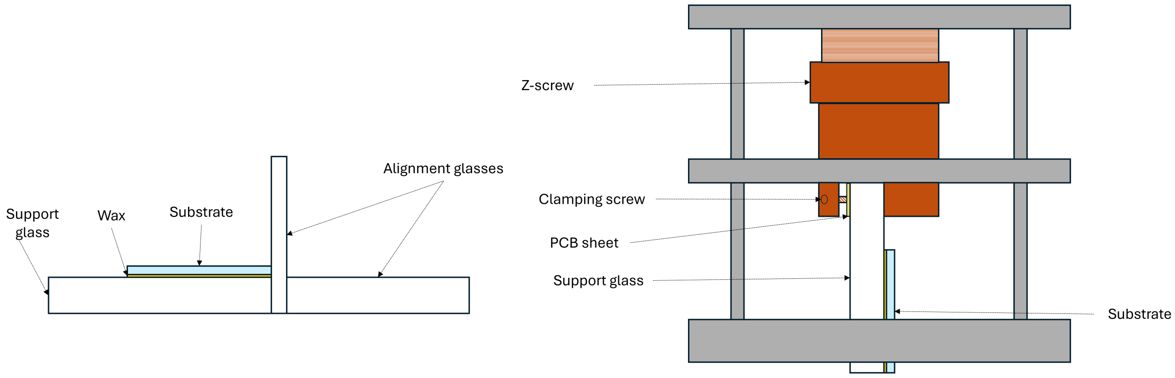

Figure 3.5: **a)** Substrate alignment using the auxiliary glasses; **b)** Polishing jig with glass assembly.

3.4 Characterization setup

Characterization of produced devices is made on the setup schematized in figure 3.6.

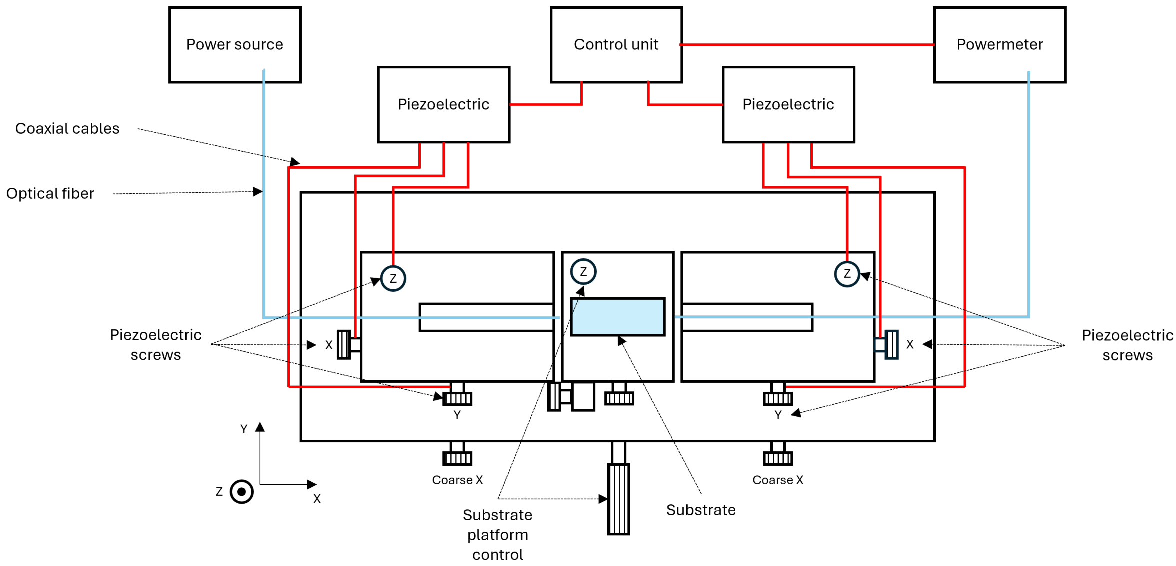

Figure 3.6: Setup employed to characterize the optical devices produced.

In this setup, a single mode fiber (SMF28) emerges from a Santec TSL-210V power source to an Elliot gold MDE881 alignment stage, where it is edge-coupled to the substrate containing the waveguides to be characterized. Transmitted light is collected by another edge-coupled SMF28 fiber/fiber-array (the latter used for the MZI study) placed in a symmetrical alignment stage and guided to a power meter (HP 8153A/EXFO IQ-203, the latter used for MZI study). Piezoelectric screws are used to align the fibers to the waveguides, which can be controlled by hand turning of the screw (coarse tuning) and through voltage applied to a piezoelectric crystal inside them (fine tuning), performed by two Elliot Scientific Dali E-2100 precision stages.

The substrate is placed upon a precision platform, which possesses four degrees of freedom: Y, Z, yaw and pitch.

On the fiber-waveguide interface, an index-matching liquid (Cargille series: AA, $n = 1.458 \pm 0.0002$) is employed to reduce Fresnel reflections, further increasing measurement accuracy.

To ensure that light is passing through a waveguide, a laser source with visible light was first used, which when focused with an objective on a surface, allowed for mode visualization. This is then followed by the tunable wavelength power source to characterize the power transmitted through the system.

3.5 Automatic alignment system

To automatize the characterization setup, an electrical circuit to automatically align the fibers was designed. The precision stages can automatically align the fiber using the ”Track” algorithm, which scans the entire voltage range of the piezoelectric crystals on the y and z axes to find the coordinates of maximum optical power transmission. An input on the back of the precision stages is provided to introduce a voltage signal coming from the power meter, which is proportional to the measured optical power.

However, connecting the power meter directly to the precision stages has two issues:

- The output power of the photodetector is not enough to power the precision stages, introducing instability and noise;
- The precision stages have current-driven inputs, which means that the current delivery for a given photodetector voltage must be maintained constant regardless of the load impedance of the circuitry from inside the precision stages. This current, however, must be proportional to the voltage coming out of the power meter, which in turn is proportional to the measured optical power.

The first issue is solved with the implementation of a simple buffer circuit at the output of the power meter, while the second problem was approached by implementing two Howland Current Sources, one for each precision stage. A Howland Current Source is an operational amplifier (Op-Amp) configuration that, for a certain input voltage, maintains the same current value through the load resistance, regardless of its value.

This behavior can only be achieved if the resistance values are chosen so that $\frac{R_1}{R_2} = \frac{R_3}{R_4}$. In that case, the circuit acts as a current source, with the output current being given by:

$$i_o = \frac{V_{in}}{R_1} \tag{3.2}$$

The resistance values were chosen so that for a maximum defined input optical power of 5 mW, which translates to, at a defined measuring sensitivity, an output voltage of 500 mV, the current going inside the precision stages, represented as the load resistances (R_L), would be the maximum signal input allowed of 2 mA, thus allowing the usage of the whole range of possible current values, maximizing the precision of the measurement. With this information, the resistances were all set to 250 Ω, with the measured values displayed in figure 3.7. However, in the most typical case in which the input optical power will be a fraction of 5 mW, sometimes being in the order of the μW, the signal fed to the piezoelectric controllers will be too small for an efficient peak detection. Thus, an inverting amplifier with a variable gain is introduced after the buffer, with the gain variation being achieved by making use of a potentiometer (100 $k\Omega$).

If we describe the potentiometer resistances before and after the contact as $R_1 + R_2 = R_T$, where R_1, R_2 and R_T are the resistances before and after the middle contact and the total resistance, respectively, by knowing the gain of an inverting amplifier $(G = -R_2/R_1)$, we get the following gain expression:

$$G = 1 - \frac{R_T}{R_1} \tag{3.3}$$

Since R_1 ranges from 0 to R_T, the possible gain values range from $-\infty$ to 1, covering all negative real numbers. To compensate for the negative gain introduced, the piezoelectric controllers have a function that allows for polarization inversion, giving back positive current values.

The operational amplifiers were powered by $\pm$ 12 V.

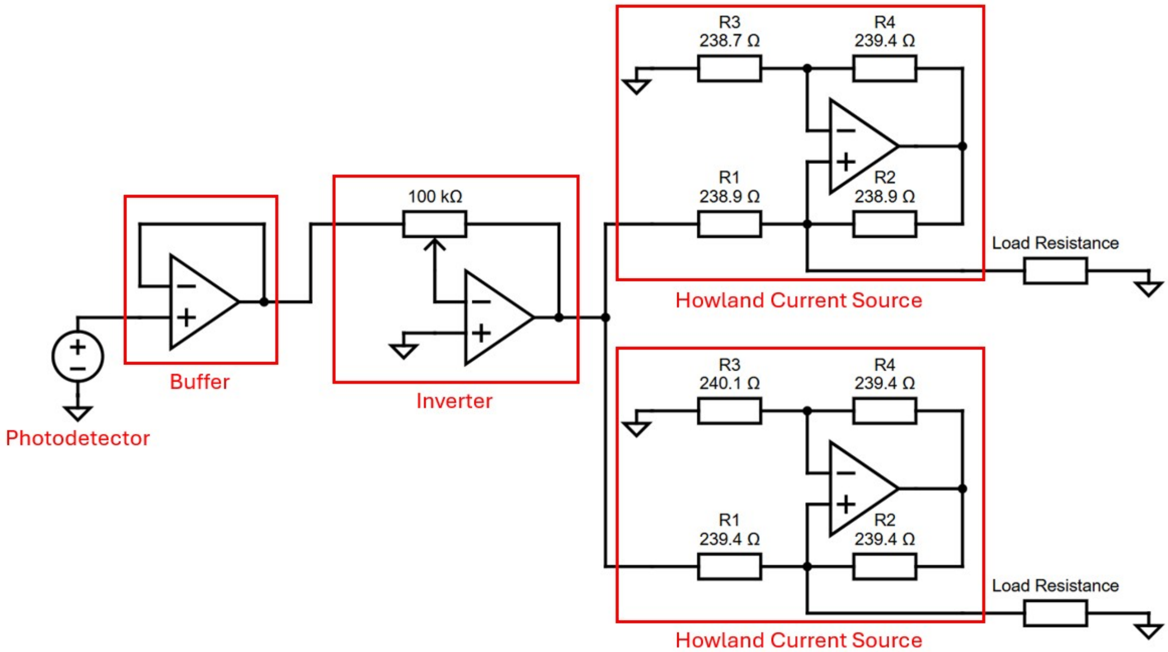

Figure 3.7: Circuit employed to power the feedback circuit from the precision stages.

Automatic alignment ensures both accuracy and precision of the measurements, while also saving time between measurements.

3.6 Characterization of optical devices

The main way to characterize the produced optical devices is through the measurement of power losses along the system. The total power loss measured on a system is described by its insertion losses (IL). This quantity is given by:

$$IL = -10\log_{10}\left(\frac{P_{out}}{P_{in}}\right) \tag{3.4}$$

, where $P_{in/out}$ are the input and output optical powers, respectively. Insertion losses can be decomposed on several loss mechanisms, namely Fresnel losses (FL), coupling losses (CL), propagation losses (PL) and bending losses (BL). These quantities relate through the following formula:

$$IL = 2CL + 2FL + PL + BL \tag{3.5}$$

3.6.1 Fresnel losses

When the optical fiber makes contact with a waveguide, light has to pass through a thin layer of air to enter the device. These medium changes introduce Fresnel losses, which are given by:

$$FL = -10\log_{10}\left(1 - \left(\frac{n_2 - n_1}{n_2 + n_1}\right)^2\right) \tag{3.6}$$

For this reason, an index-matching fluid is introduced in the fiber-waveguide interface, drastically reducing these losses. For comparison, by knowing the refractive indices of fused silica and EAGLE2000 at 1550 nm (1.444 and 1.5145, respectively), the Fresnel losses without the index-matching would be of 0.331 dB. By introducing the fluid, these losses decrease to 0.001 dB, a drastic decrease that allows us to ignore this kind of losses.

3.6.2 Coupling Losses

Beyond Fresnel reflections, there are also coupling losses related to mode mismatch between fiber and waveguide.

To measure mode mismatch, the setup illustrated in figure 3.8 was employed.

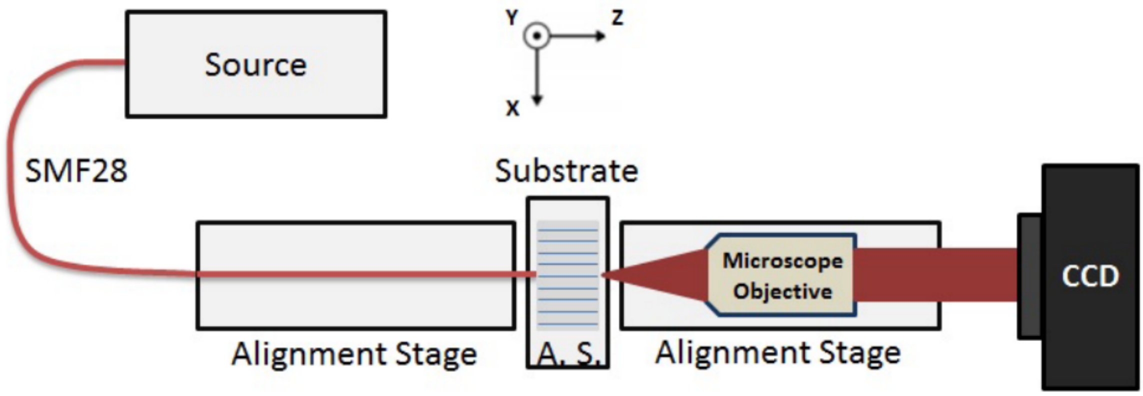

Figure 3.8: Optical system employed to determine coupling losses. Taken from [56].

A microscope objective magnifies and focuses light coming out of the substrate onto a CCD camera (Point Grey Research CMLN-13S2M-CS), which is attached to a tube to prevent contact with airborne particles and to reduce noise on the image.

The CCD camera captures the intensity profile of the magnified laser beam, which can be analyzed with LaseView. This camera possesses different sensitivities in different areas, which means that a zone with an approximately uniform sensitivity must be found so that a reasonably accurate image can be formed. This also means that an objective with high magnification cannot be used, so that the image fits the designed sensitivity zone, which has the disadvantage of lowering resolution. For this reason, a 20 x lens was used. Figure 3.9 shows examples of zones with uniform and non-uniform sensitivities.

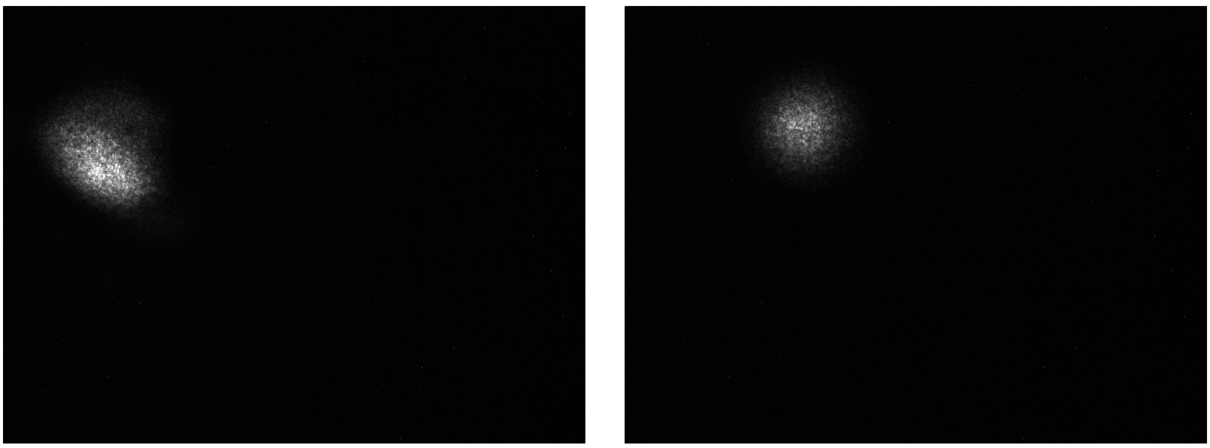

Figure 3.9: CCD images of light intensity profiles. The left image depicts a zone with different varying sensitivities, resulting in an inaccurate measurement of the mode profile. The right image shows the desired output.

The magnified mode diameter of the optical fiber, a', and the distances along the X and Y axes of the waveguide mode where the intensity is e^{-2} of the peak intensity, d'_x and d'_y, were taken. By knowing the real mode diameter of the SMF28 optical fiber (10.4 μm @ 1550 nm), the magnifying factor introduced by the objective lens was determined, allowing for the determination of d_x and d_y.

The electric fields inside fiber and waveguide are assumed to be monomode, thus possessing gaussian shapes:

$$\begin{cases} E_f(x,y) = A_f \exp((x^2+y^2)/a^2) \\ E_w(x,y) = A_w \exp((x/d_x)^2 + (y/d_y)^2) \end{cases} \tag{3.7}$$

Performing the overlap integral of both of these profiles allows for the determination of the coupling coefficient, η, given by the following equation:

$$\eta = \frac{|\int_{-\infty}^{+\infty} E_f(x,y)E_w(x,y)dxdy|^2}{\int_{-\infty}^{+\infty} |E_f(x,y)|^2 dxdy \int_{-\infty}^{+\infty} |E_w(x,y)|^2 dxdy} \tag{3.8}$$

Combining equations 3.7 and 3.8, a simplified expression is achieved:

$$\eta = \frac{4a^2 d_x d_y}{d_x^2 + d_y^2} \tag{3.9}$$

From this, the coupling loss (in dB) can be calculated:

$$CL = 10 \log_{10}(\eta) \tag{3.10}$$

3.6.3 Propagation losses

When traveling along the waveguide, light suffers losses of many natures, including absorption losses, scattering losses, namely Rayleigh and Mie scattering, rough sidewalls or inhomogenities, radiation losses, and many others. All of these mechanisms can be described by an attenuation coefficient, α, which dictates the rate of power loss inside the waveguide per distance traveled. The specific decrease in power is, after a distance l of propagation, $P(l) = P(0)\exp(-\alpha l)$, and it allows for the determination of losses per centimeter of propagation:

$$PL_{dB/cm} \approx 4.3\alpha \tag{3.11}$$

α can be determined by the cut-back technique, which involves measuring $P(l)$ for several lengths of a straight waveguide, however, this involves several cutting and polishing steps of the substrate, which takes a considerable amount of time. An alternative is the calculation of the propagation losses per centimeter by knowing the insertion and coupling losses. This can be done through equation 3.12, where l is the waveguide length.

$$PL_{dB/cm} = \frac{IL - 2CL}{l} \tag{3.12}$$

3.6.4 Bending losses

When the waveguide possesses curvature, the propagating mode becomes partially distorted, and it can couple with radiation modes not present in the core [57], introducing bending losses. Furthermore, it was found that bending losses per unit length exponentially increase as the radius of curvature decreases [7]. This relation is described by equation (3.13).

$$BL_{dB/cm} = ae^{-bR} \tag{3.13}$$

The parameters a and b ought to be obtained experimentally.

The most straightforward way to find a and b is through the creation of several curved waveguides, all with the same length of the curved part but different curvature radii. From this, the bending losses per centimeter can be calculated for each radius by knowing the insertion losses of the bends and that of a straight waveguide with the same length (l_c) through equation (3.5).

$$BL_{dB/cm} = \frac{IL_{curve} - IL_{straight}}{l_c} \tag{3.14}$$

Fitting an exponential curve allows for an empyrical determination of a and b.

4 Fabrication of fundamental optical devices

In this chapter, several fundamental passive optical devices were produced, with the main focus being compactness, the minimization of insertion losses, and repeatability, in order to implement them in Mach-Zehnder interferometers. Some fabrication parameters, such as numerical aperture, repetition rate, beam polarization and inscription depth were fixed. Other parameters, such as pulse energy and writing speed were analyzed and optimized. Several s-bends with different radii were tested and optimized for compactness and power losses. The best results from both straight waveguides and s-bends were used for the fabrication of directional couplers, which were also tested for different separation distances and interaction lengths. The main goal was to find the parameters that allow for 50:50 power splitting, while also minimizing device footprint and keeping low asymmetry.

4.1 Background

Waveguides are devices that allow confinement and propagation of light. They are composed of a core with a refractive index of n_{co}, and a cladding with n_{cl}. Light guiding, however, is only possible if the refractive index at the core, n_{co}, is higher than at the cladding n_{cl}, since only this way it is possible to achieve Total Internal Reflection (TIR) [58] [59]. Inside the waveguide, light can only propagate through certain modes which are the solutions to Maxwell's equations under the imposed constraints. Waveguides produced in this work are characterized by a refractive index distribution that varies only in the directions transversal to laser inscription, N(x,y), remaining invariant along the z direction. Taking advantage of this geometry, propagating modes assume the following form:

$$\mathbf{E}(x, y, z) = \mathbf{E_m}(x, y)e^{-i(\beta_m z - \omega t)} \tag{4.1}$$

, where $\mathbf{E_m}(x, y)$ and β_m are the transversal electric field and the propagation constant of the mode m, respectively.

Another quantity, the generalized frequency V, quantifies the number of modes that propagate inside of an optical fiber, however, as it can be seen in image 4.1, the cross-section of produced waveguides resemble those of optical fibers, allowing for an approximation to a certain degree of V [60]. The formula for this quantity is shown below [61]:

$$V = \frac{2\pi a}{\lambda}\sqrt{n_{co}^2 - n_{cl}^2} \tag{4.2}$$

For a circular step-index fiber with core radius equal to the highest semi-axis of the waveguides produced (7.379 μm), by a rough estimation of n_{co} = 1.5149 and n_{cl} = 1.5143 [62], it is possible to obtain V $\approx$ 1.196 < 2.405, the cutoff frequency. This estimation shows that the waveguides produced are monomode under the measuring wavelength [63].

$$\mathbf{E}(x, y, z) = E(x, y)e^{-i(\beta z-\omega t)}\hat{\mathbf{e}} \tag{4.3}$$

, where $\hat{\mathbf{e}}$ is an arbitrary direction transverse to $\hat{\mathbf{z}}$.

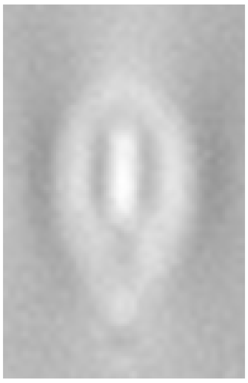

Figure 4.1: Transmission mode optical microscope image of the cross-section of a waveguide produced on an EAGLE2000 glass substrate.

4.2 Choice of fabrication parameters

The properties of produced waveguides depend on the chosen fabrication parameters. Thus, the first step in producing optical devices passes by constraining some parameters, namely numerical aperture, repetition rate, writing polarization and inscription depth. A high numerical aperture introduces aberrations that break down the paraxial regime. A previous study performed by Vítor A. [2] on this material showed that an objective with a numerical aperture of 0.7 produces a secondary structure below the main wave-guiding region, guiding light for some fabrication parameters. The same work also motivates the use of an objective lens with a numerical aperture of 0.42. The repetition rate was fixed at 1 MHz [3] [4] to ensure that laser modification is in a heat accumulation regime [5]. The writing polarization is kept parallel to the inscription direction to avoid the ”Quill” effect [6] [1]. Inscription depth is also an important parameter, since keeping it below 100 μm avoids spherical aberrations [2]. Lower depths also decrease the power necessary to perform light modulation on future produced MZIs [4], as the temperature difference between the two arms is more easily achieved the closer they are to the microheater.

4.3 Pulse energy and writing speed optimization

In this section, the effects of laser pulse energy and writing speed were studied on waveguide production. Four sets of straight waveguides were produced with pulse energies of 125, 150, 175 and 200 nJ, and within each set, writing speed was varyed from 10 to 80 mm/s in steps of 5 mm/s. The waveguides have a length of 2.4 cm.

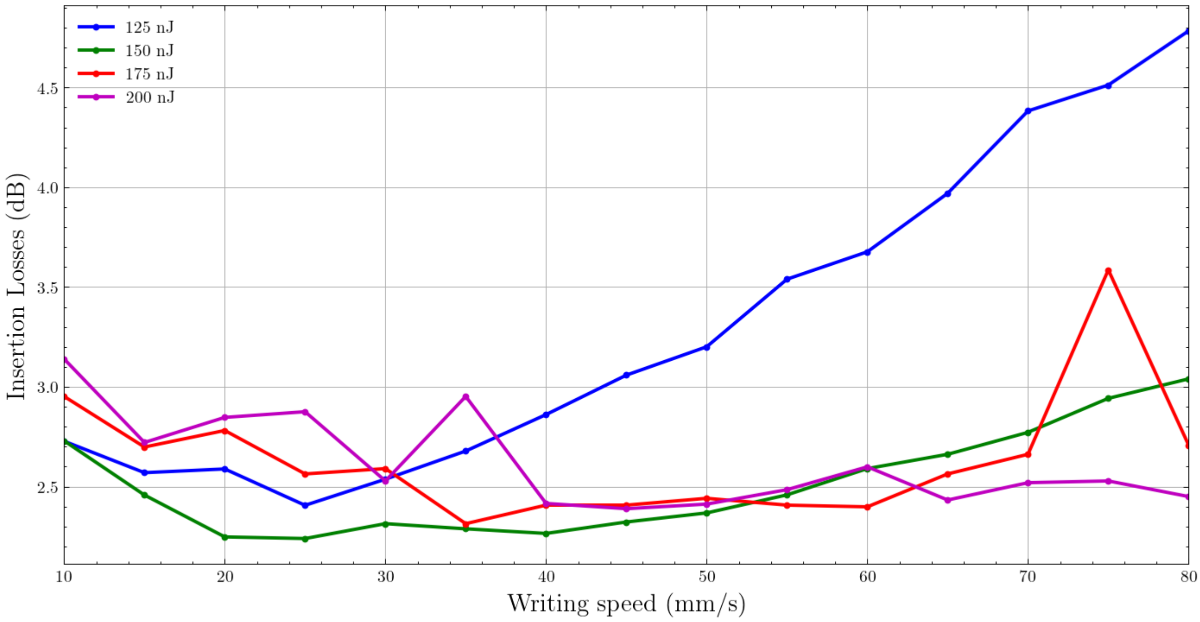

Figure 4.2: Dependence of insertion losses on writing speed for several pulse energies.

Fig. 4.2 shows the dependence of insertion losses on the writing speed for several values of the pulse energy. For the 125 nJ set, losses generally decrease until 25 mm/s, where they start to sharply rise. This loss increase can be due to the decreased fluence for higher writing speeds, translating into a smaller modified area and a smaller refractive index contrast, resulting in weaker light confinement and, ultimately, higher losses. For 150 nJ, less variability is observed, however losses decrease until a set of minima ranging from 20 to 40 mm/s is reached. After this, losses increase monotonically, but not as much as in the previous case. This can be explained by ways similar to the last pulse energy value, however to a lesser degree, since this time fluence for the same writing speed is higher. For a pulse energy of 175 nJ, an overall decrease in insertion losses is observed until 35 mm/s, followed by a small increase in insertion losses, and an unexpected peak at 75 mm/s, probably due to defects in the material or in fabrication. The last energy value, 200 nJ, is characterized by a general decrease in insertion losses, with an anomaly being found at 35 mm/s, which can also be due to defects on the material or fabrication. An approximately constant behavior is observed from that point up to the last writing speed tested.

Coupling losses were also studied to better understand the different loss mechanisms on the waveguides. Figure 4.3 displays the coupling losses as a function of writing speed for several pulse energies.

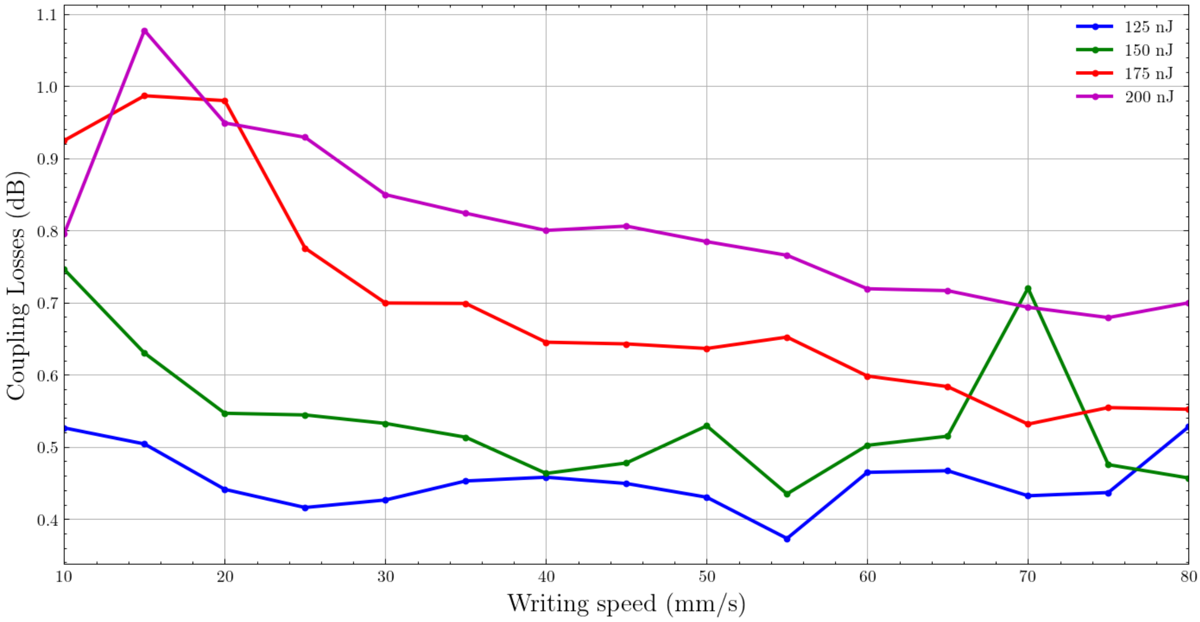

Figure 4.3: Dependence of coupling losses on writing speed for several pulse energies.

For the same writing speed, coupling losses tend to increase for increasing pulse energy. This tendency can also be inferred from the increase in mode-field diameters in the X and Y directions with increasing pulse energy displayed in fig. 4.4. Although a higher pulse energy results in a higher refractive index contrast, which leads to higher confinement and smaller MFDs, this phenomenon may be outweighed by the increase in modified volume, which in turn leads to modes with overall higher MFDs. Since the MFD of the SMF28 optical fiber is of $\approx$ 10.4 μm, higher MFDs result in higher mode mismatch, and in turn, higher coupling losses. For all pulse energies, coupling losses tend to decrease with increasing writing speeds. This can be explained by the decrease in net fluence, which, once again, ultimately leads to smaller MFDs and mode mismatches. The only exception lies in the 125 nJ set, where coupling losses start to increase after a minimum at 55 mm/s is reached, along with a generalized increase in MFD. Here, the smaller refractive index contrast leads to a weaker confinement, and despite the smaller modification volume, the net result is an increase in MFD.

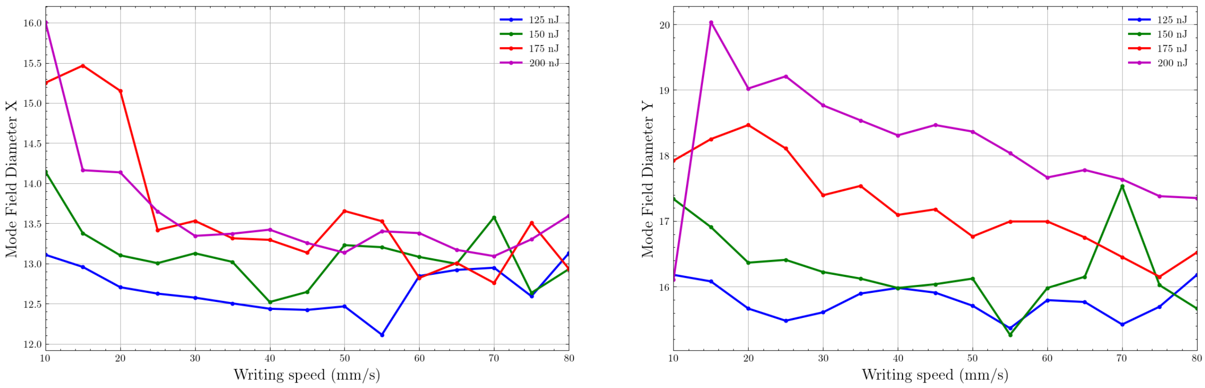

Figure 4.4: Mode field diameters in the X (left) and Y (right) directions as a function of writing speed for several pulse energies.

Propagation losses were also studied as a function of writing speed for several pulse energies. For a given writing speed, propagation losses tend to increase with decreasing pulse energies. This can be attributed the smaller confinement observed for lower energies, caused by the smaller refractive index contrast, which can lead to higher scattering losses due to imperfections in the cladding-like structure of the modified region. For all pulse energies, propagation losses tend to increase for higher writing speeds. As stated before, this can be attributed to the lower fluence that translates into smaller mode confinement and, consequently, higher cladding losses. This is very noticeable for the 125 nJ set, but becomes less relevant for higher energies, until the 200 nJ set, where there seems to be an independence of propagation losses on writing speed, indicating that mode confinement does not change.

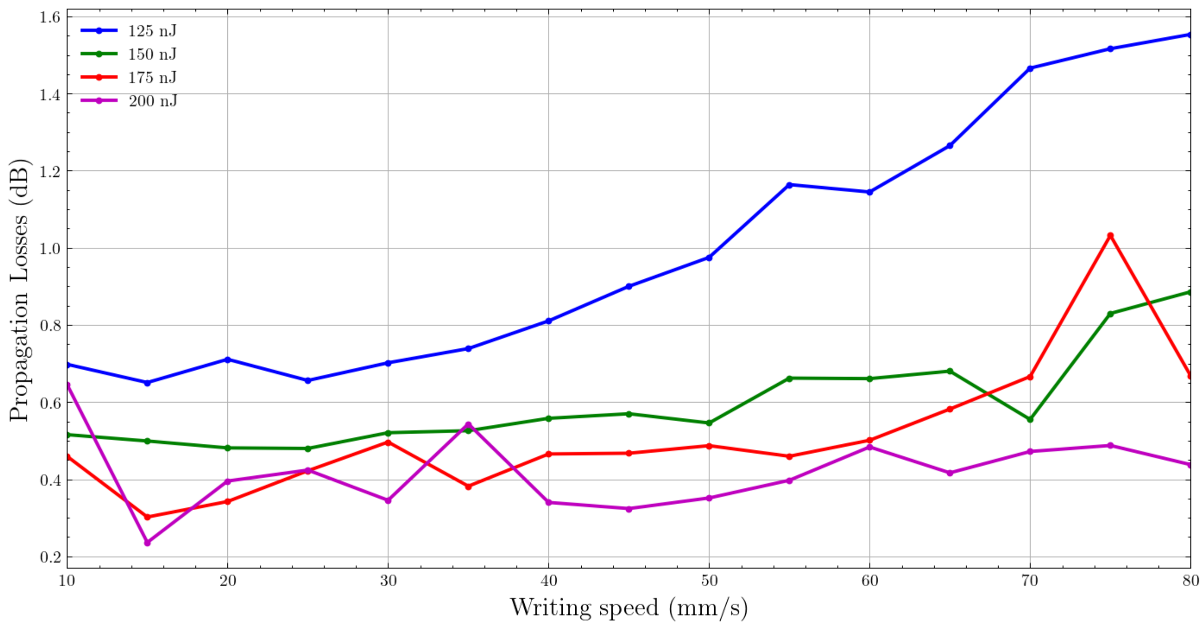

Figure 4.5: Dependence of propagation losses on writing speed for several pulse energies.

4.4 S-bend radius optimization

The fabrication of directional couplers, Mach-Zehnder interferometers and many other optical devices demands the redirection of light inside the substrate without the introduction of significant additional losses. To this end, s-bends consisting of two arch circumferences were studied for the losses they introduce in the system. Fig. 4.6 shows a schematic representation of this structure.

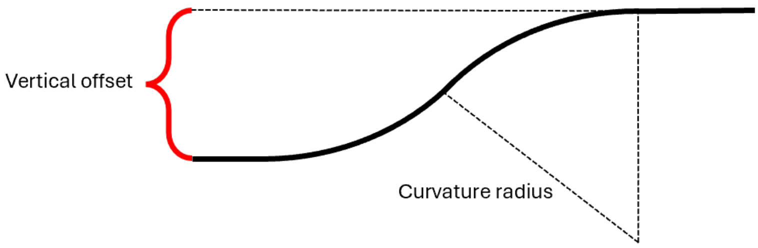

Figure 4.6: Schematic representation of the s-bend employed in this work.

Although there are curve shapes that introduce smaller losses, such as the cossine profile [64], the double arch circumference is not far behind in performance. Furthermore, this method is the simplest to implement on the software, while also allowing for an easy theoretical calculation of the losses introduced by bending, which can be calculated based on the theory described in section 3.6.4.

Since all of the next devices contain s-bends, the choice in fabrication parameters is important to guarantee the smallest possible insertion losses. In section 4.3 it was observed that smaller propagation losses reside at higher pulse energies, however, coupling losses are also higher than for lower energies. Higher energies are also associated with a higher refractive index contrast, which translates into smaller bending losses [36]. By taking all these factors into account, a pulse energy of 150 nJ and a writing speed of 35 mm/s were chosen for all studied devices, since this set of values shows relatively small coupling and propagation losses, and is expected to lead to relatively small bending losses.

The writing polarization is kept fixed along the X direction, meaning that in only remains parallel to the writing direction on the straight portions of the device, not being the case for the curved sections. Nevertheless, it should not present significant changes in losses. For the geometric parameters, the radii of curvature was varied between 10 and 100 mm in steps of 10 mm. The vertical offset introduced was of 112.5 μm for all the s-bends.

Below the s-bends, three straight waveguides were produced so that bending losses can be calculated by subtracting the insertion losses of these waveguides to those of the s-bends. Although distance traveled on the s-bends is slightly higher, introducing more propagation losses than in the straight waveguides case, the maximum difference in distance is 0.004 mm, translating into negligible losses. The straight waveguides yielded output powers which were averaged and produced insertion losses of 2.86 $\pm$ 0.3 dB. Figure 4.7 depicts the bending losses as a function of curvature radius.

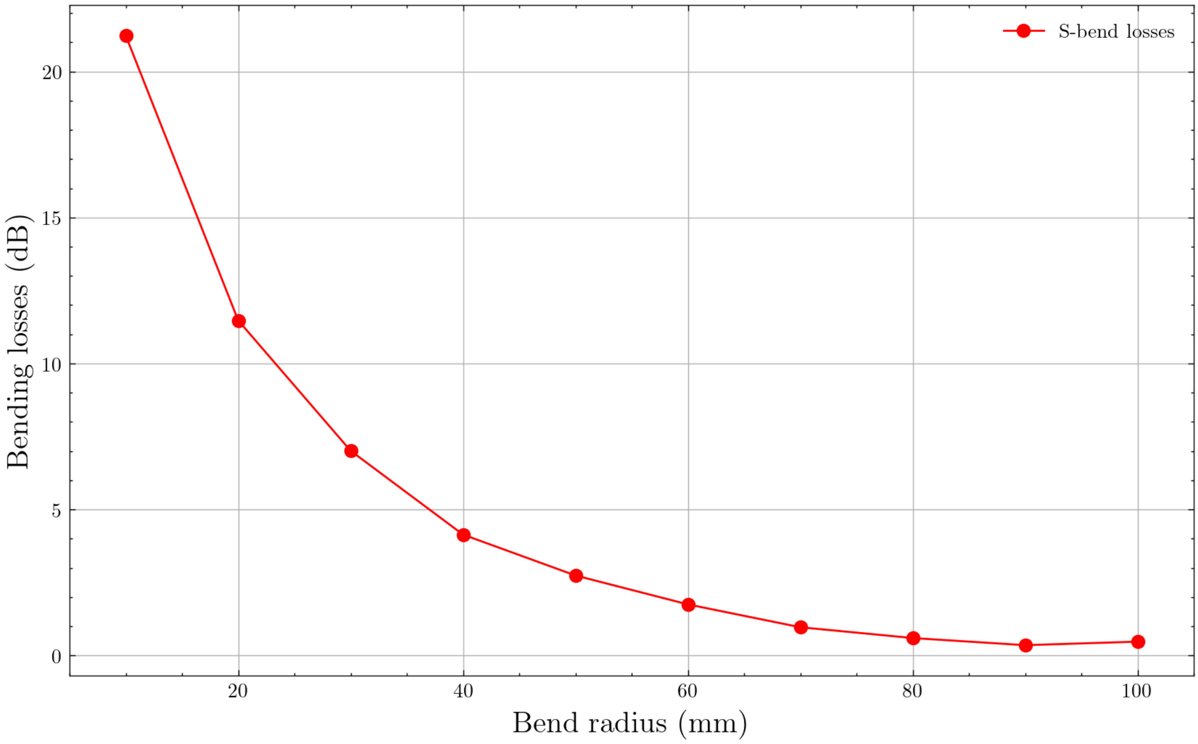

Figure 4.7: Bending losses for s-bends with varying radii.

A bending loss decay with increasing radii is observed, which is to be expected, since the larger the radius gets, the closer the s-bend becomes to a straight waveguide. For a radius of 100 mm there seems to be a small increase in bending losses, probably due to the fact that this s-bend is in an extreme of the substrate, where more debris are present, increasing insertion losses. After a radius of 70 mm, the insertion losses do not present a significant decrease from one to the next. Indeed, from 60 to 70 mm, the insertion losses show a decrease in 0.78 dB, while from 70 to 80 mm, this decrease is of only 0.37 dB. Since the devices must be compact in order to increase integration density, a bending radius of 70 mm is chosen for future devices to optimize the efficiency-compactness trade-off.

From this data, and knowing the arc lengths (l_c) for each s-bend, bending losses per centimeter were estimated and fitted with the function $f(x, a, b, c) = a + b * exp(-c * x)$ to verify equation (3.14). The 10 mm radius s-bend was removed since it was considered an outlier, allowing for a better data fitting.

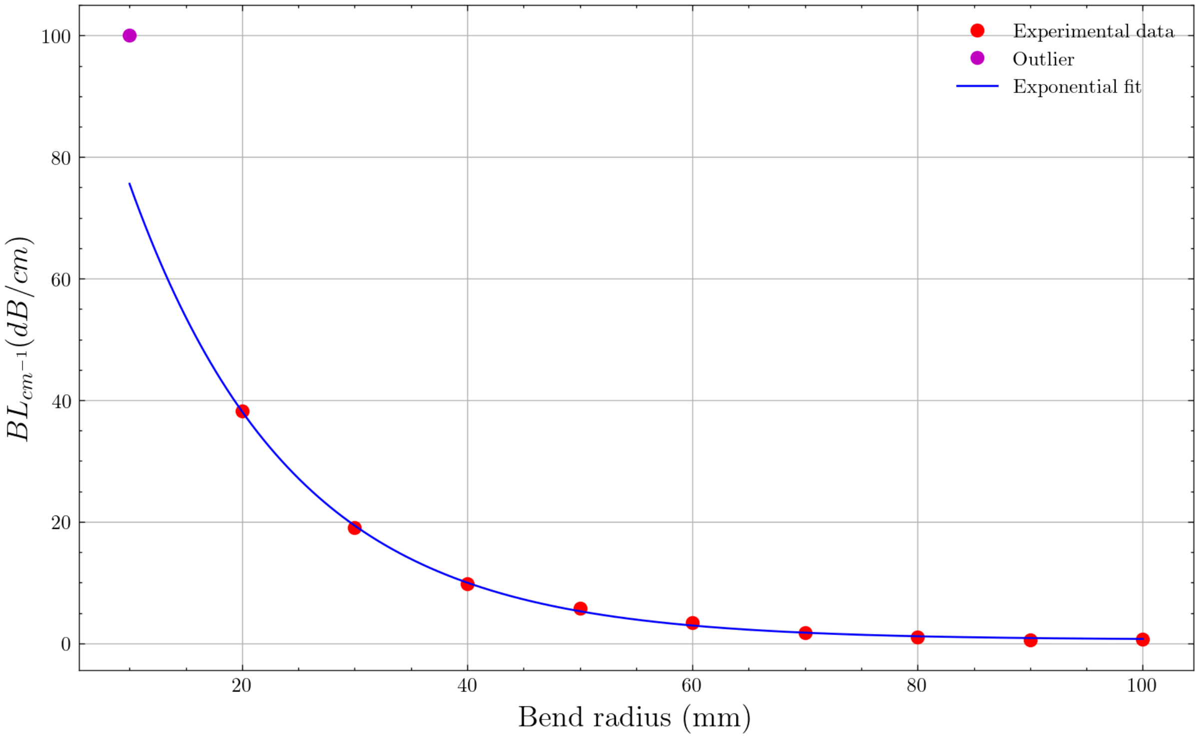

Figure 4.8: Bending losses per centimeter and corresponding fit.

The fit parameters and corresponding uncertainties are depicted in table 4.1.

	a (dB/cm)	b (dB/cm)	c (mm^{-1})	r^2
value	0.59	150	0.069202	0.9994
uncertainty	0.04	26	0.000003	

Table 4.1: Optimized fitting parameters.

As it can be seen, the behavior is well predicted by this fit, with minimum achieved bending losses per centimeter of 0.56 dB/cm at a bend radius of 90 mm. For the 70 mm bend radius, this value is of 1.73 dB, which is considerably higher, however, for the productions of interest, this will not make a very big difference.

4.5 Directional Couplers

The next step in producing MZIs is the fabrication and optimization of directional couplers. These devices act as beam-splitters, essentially dividing incoming light waves into two beams with optical powers that depend on the geometrical and material parameters of the system. Directional couplers are used in a myriad of photonic devices, such as electro-optic modulators [65], quantum logic gates [66] , boson sampling [67], optical interleavers [68], wavelength division (de-)multiplexers [69], polarization splitters [70], and many others. In this section, several directional couplers with different geometries will be analyzed and studied, with special focus in achieving 50:50 power splitting, to be used in MZI production.

4.5.1 Coupled Mode Theory

In this section, Coupled Mode Theory will be used to explain the behavior of directional couplers, namely how they can transfer energy between their interacting arms. It is a typical approach that, although only approximate, assuming , provides a simple and efficient explanation of light coupling on ideal waveguides (no losses). For a more profound analysis, see the following works [71] [72] [73].

As it was stated in the last chapter, a waveguide has one or several guided modes that are solutions to Maxwell's equations on that specific configuration. If we consider two separate waveguides, I and II, that do not interact with each other, they will possess solutions ψ_a and ψ_b with propagation constants β_a and β_b, and they will propagate independently from each other. Only the case in which ψ_a and ψ_b are co-directional and $\beta_b > \beta_a$ will be treated.

$$\begin{cases} \psi_a = A(z)E_a(x,y)e^{-i\beta_a z}e^{i\omega t} \\ \psi_b = B(z)E_b(x,y)e^{-i\beta_b z}e^{i\omega t} \end{cases} \tag{4.4}$$

If the waveguides are sufficiently close to each other, these modes cease to exist, and instead, the ordinary and extraordinary modes, ψ_o and ψ_e, appear. These modes are given by:

$$\begin{cases} \psi_o = (E_a(x,y) + E_b(x,y))e^{-i\beta_o z}e^{i\omega t} \\ \psi_e = (E_a(x,y) - E_b(x,y))e^{-i\beta_e z}e^{i\omega t} \end{cases} \tag{4.5}$$

The original modes can be described as linear combinations of ψ_o and ψ_e, with $A(z)$ and $B(z)$ taking the following forms:

$$\begin{cases} A(z) = [A_0 e^{i\beta_c z} + A_e e^{-i\beta_c z}]e^{-i\Delta z} \\ B(z) = [B_0 e^{i\beta_c z} + B_e e^{-i\beta_c z}]e^{i\Delta z} \end{cases} \tag{4.6}$$

These quantities relate to the original ones through the following relations:

$$\begin{cases} \beta_{e,o} = \beta_m \pm \beta_c \\ \beta_m = \frac{\beta_a + \beta_o}{2} \\ \beta_c = \sqrt{\kappa^2 + \Delta^2} \\ \Delta = \frac{\beta_b - \beta_a}{2} \end{cases} \tag{4.7}$$

, where κ is the coupling coefficient, which quantifies the degree of coupling between the two modes.

The coupling coefficient quantifies the degree of coupling between the two interacting modes, being proportional to the following expression:

$$\kappa \propto \iint E_a(x,y)E_b(x,y)dxdy \tag{4.8}$$

An empyrical equation relates κ and the interaction region separation, s_i [74]:

$$\kappa(s_i) = \kappa_0 * e^{-\alpha s_i} \tag{4.9}$$

, where κ_0 and α are two constants that depend on the modal profiles of the two involved modes, and on the properties of the material.

$A(z)$ and $B(z)$ must also satisfy the coupling mode equations and boundary conditions:

$$\begin{cases} \frac{dA(z)}{dz} = -i\kappa B(z)e^{i2\Delta z} \\ \frac{dB(z)}{dz} = -i\kappa A(z)e^{-i2\Delta z} \\ A(0) = A_e + A_o \\ B(0) = B_e + B_o \end{cases} \tag{4.10}$$

Solving this set of equations allows us to write the following expression for the transfer matrix, which is the response of the directional coupler to an arbitrary set of input amplitudes $A(0)$ and $B(0)$ on the upper and lower ports, respectively:

$$\begin{bmatrix} e^{-i\Delta L_i}\left(\cos\beta_c L_i - i\frac{\Delta}{\beta_c}\sin\beta_c L_i\right) & e^{-i\Delta L_i}\left(\frac{-i\kappa}{\beta_c}\right)\sin\beta_c L_i \\ e^{i\Delta L_i}\left(\frac{-i\kappa}{\beta_c}\right)\sin\beta_c L_i & e^{i\Delta L_i}\left(\cos\beta_c L_i + i\frac{\Delta}{\beta_c}\sin\beta_c L_i\right) \end{bmatrix} \tag{4.11}$$

Here, L_i is the interaction length, which is the length along which the waveguides are brought close together.

Since light starts to couple on the s-bends before reaching the interaction region, these also introduce a phase-shift, ϕ_0, and thus the arguments of the trigonometric functions suffer the following transformation:

$$\beta_c L_i \rightarrow \beta_c L_i + \phi_0 \tag{4.12}$$

The normalized power transferred between the two arms is given, therefore, by:

$$\begin{cases} |A(z)|^2 = 1 - F \sin^2(\beta_c L_i + \phi_0) \\ |B(z)|^2 = F \sin^2(\beta_c L_i + \phi_0) \end{cases} \tag{4.13}$$

Here, $F = (\kappa/\beta_c)^2$ is the maximum power transfer between the two arms.

Coupling length, the distance interval between minimum and maximum power transfer, is given by:

$$L_c = \frac{\pi}{2\beta_c} \tag{4.14}$$

4.5.2 Fabrication Parameters

The same parameters used for the production of s-bends were used. Produced devices are composed of two waveguides that start separated by a pitch of 250 μm and are brought close together by s-bends, where they become separated only by the interaction region separation (s_i) for a certain interaction length (L_i). Afterwards, s-bends separate the waveguides to their original distances. A schematic representation can be seen in fig. 4.9.

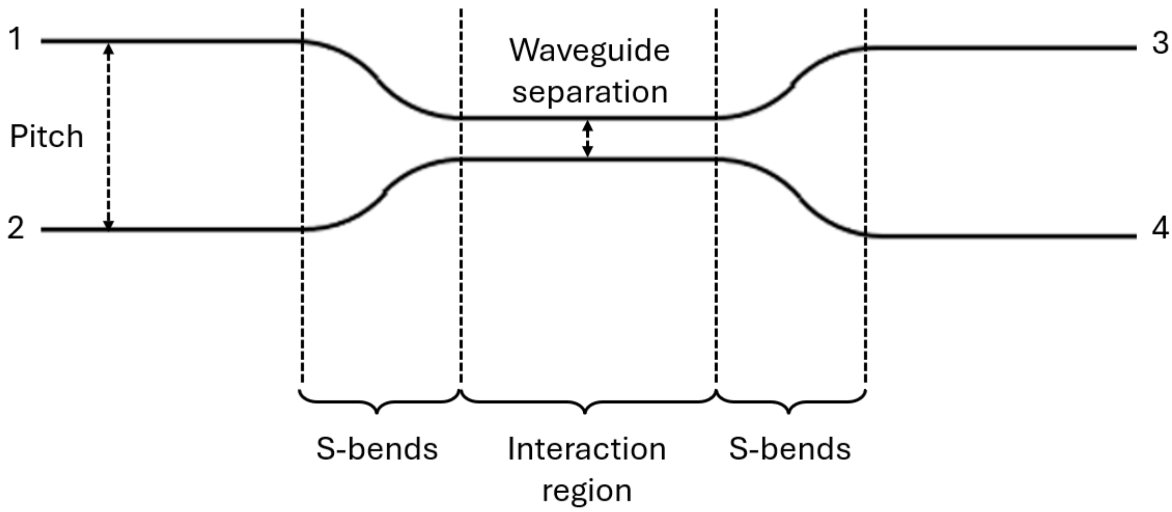

Figure 4.9: Schematic representation of produced directional couplers.

The s-bend radius was chosen to be R=70 mm. Although this radius does not provide minimal losses, these do not decrease significantly for further radii increase, with the advantage of allowing more compactness in the horizontal dimension when the vertical dimension is fixed. This will be proven useful when the interaction distance is to be increased. Three sets of directional couplers with interaction region separations (s_i) of 15, 20 and 25 μm were produced. Smaller values were not chosen, as from the previous study on the waveguides, the fundamental mode obtained for the fabrication parameters used (150 nJ, 35 mm/s) showed a mode-field diameter (MFD) on the x-direction of 13 μm, thus, lowering this separation could result in waveguide superposition, leading to asymmetries that would prevent complete power transfer from one arm to the other on the directional coupler.

For each group of directional couplers, 3 straight waveguides were made to estimate the insertion losses on different zones of the substrate to discard any possible dependence with position on the substrate. 50 directional couplers with varying interaction lengths were produced. These lengths ranged from 0 to 7.35 mm, with a 150 μm step. The pitch, which is the distance between the arms of the directional coupler before and after the interaction region, was fixed at 250 μm. For every coupler, the input fiber was coupled to the lower arm in order to measure transmitted power.

4.5.3 Device characterization

For the first set of directional couplers, with a separation of 15 μm, the three waveguides were measured and, on average, yielded insertion losses of 2.81 $\pm$ 0.2 dB.

Figure 4.10 shows the output optical powers on the upper and lower arms of the coupler, as well as the total output optical power as a function of interaction length. Each measurement was made two times and the average was plotted. An oscillating behavior is observed, with power being almost completely transferred from one arm to the other. Also noticeable is the existence of a localized drop in power that only seems to happen at the lower arm. This could mean that a defect is present in this arm after the interaction region, that could be due to defects on this region or a poor coupling to the fiber. The total optical power, after 3 mm of interaction length, seems to steadily decrease. This can be caused by a coupling with non-propagating modes generated on the interaction region, and since longer interaction regions means more coupling, more power is being lost.

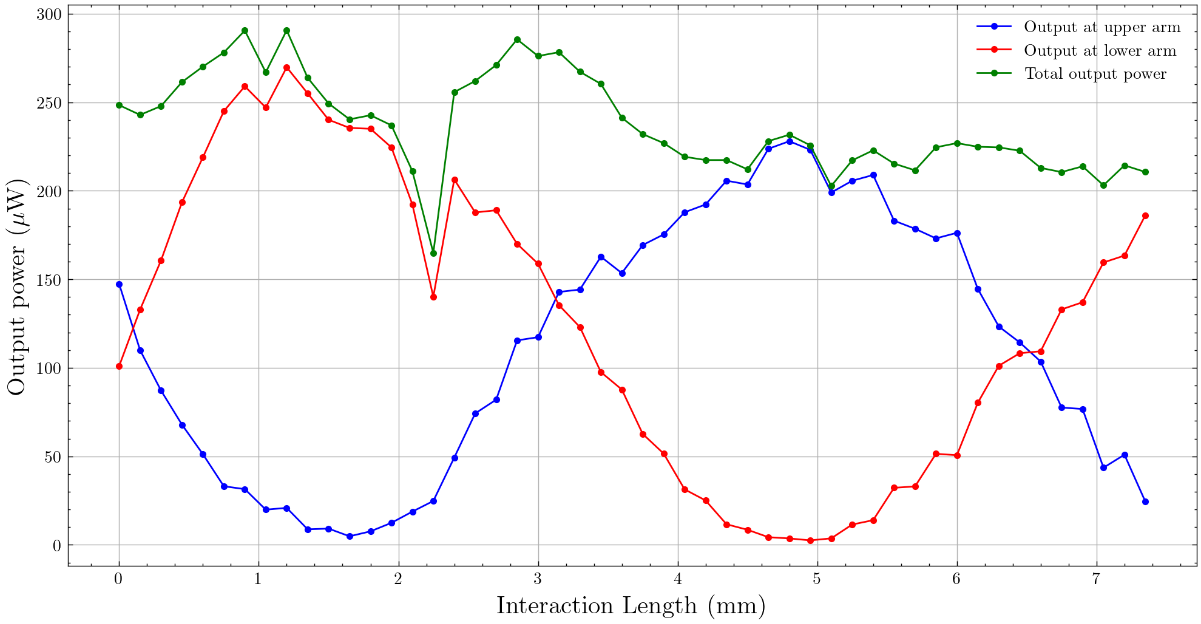

Figure 4.10: Output optical powers of the upper and lower arms, and total output power as a function of interaction length.

The reflectivity, defined as the power coming out of the lower arm (input at lower arm) divided by the total output power, was measured as a function of interaction length. Each measurement was made two times and the average is plotted in figure 4.11 as a function of interaction length.

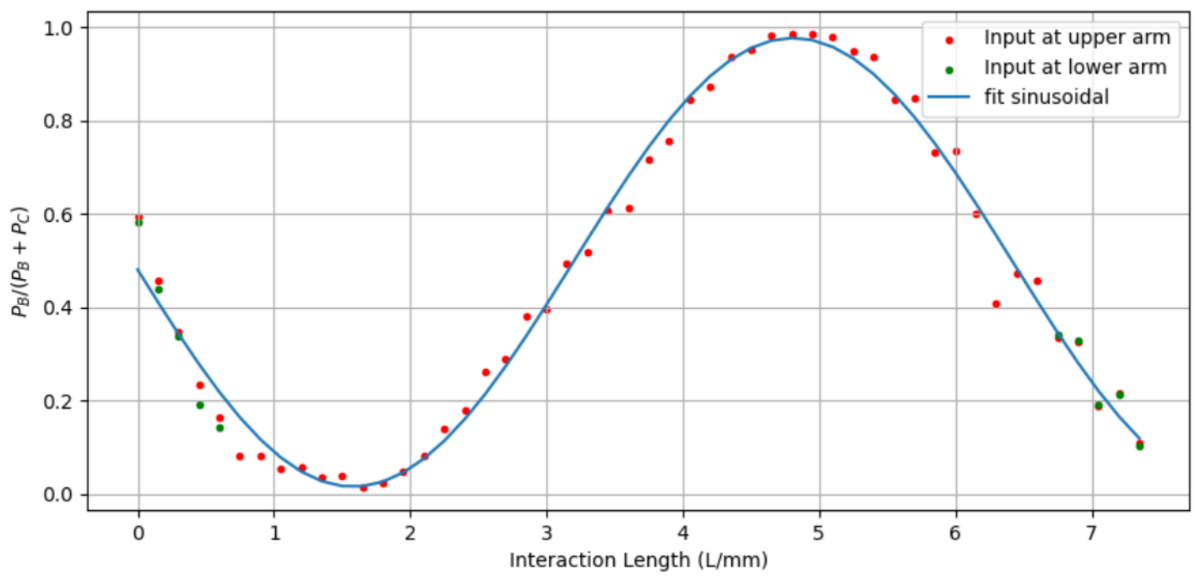

Figure 4.11: Reflectivity of directional couplers with a 15 μm separation as a function of interaction length.

The points in red and purple represent the reflectivity through the upper arm, while the green points correspond to the same quantity measured from the lower arm. The latter set of points show a smaller reflectivity, indicating a stronger coupling to the opposite arm, a sign of waveguide asymmetry.

Overall, the behavior can be accurately described by a sinusoidal fit of the form $f(L, F, \beta_c, \phi_0) = 1 - F\sin^2(\beta_c * L + \phi_0)$. It was found that the points in purple do not follow the fit, and for this reason they were removed from it. The parameters obtained are in table 4.2.

	F	β_c (rads/mm)	ϕ_0 (rads)	κ (rads/mm)	Δ (rads/mm)	L_c (mm)	r^2
value	0.9675	0.48148	0.8152	0.47359	0.0867	3.2625	0.991
uncertainty	0.0001	0.00003	0.0006	0.00003	0.0003	0.0001	-

Table 4.2: Parameters of directional coupler set with 15 μm separation.

The first feature to notice is the non-unitary F, which raises from the existence of the aforementioned asymmetry between the arms quantified by Δ. This asymmetry might come from some superposition between the two waveguides in the interaction region, and it inhibits a total power transfer between the arms, with the minimum achieved reflectivity value being of 0.014, even though the interaction length for which there is minimum reflectivity was most probably not reached. The phase ϕ_0 arises from the coupling happening at the s-bends, which themselves introduce some power transfer. As it was mentioned before, at small interaction lengths, the reflectivity does not seem to accompany the fit. It could be due to the proximity of this zone to the edge of the substrate, which could be less clean or poorly polished.

The estimated coupling length L_c is much smaller than that obtained by Vítor A. [56] for fused silica substrates and for the same separation, having attained 5.6 mm. This discrepancy is due to the higher confinement observed in fused silica, which yielded a mode with an MFD of 12.3 μm x 7.1 μm, while modes on these waveguides yield 13 μm x 16.1 μm. This increase in mode size results in a higher coupling coefficient (κ), which in turn increases β_c and decreases L_c. This decreased confinement, however, translates into higher curvature radii than in the fused silica case, increasing device footprint.

Overall, the graph covers three regions of 50:50 power splitting.

For the 20 μm separation devices, the average output power of the three waveguides below yielded insertion losses of 2.693 $\pm$ 0.009 dB, slightly smaller than the 2.81 dB obtained for the first set of waveguides, possibly indicating better device quality in this zone, probably due to better cleanliness/polishing conditions.

Output optical powers on the upper and lower arms of the coupler, as well as total output optical power are depicted as a function of interaction length in figure 4.12. A large anomaly is seen on the upper arm, with power oscillating in an unexpected manner. This could be due to localized defects in the substrate, since after an interaction length (l_i) of 3 mm the behavior seems to be the one expected. After 4 mm the total optical power decreases steadily, once again, probably meaning that power is being transferred to non-propagating modes. Total power transfer is not observed, only reaching a minimum for the upper arm of 22.6 μW, indicating waveguide/mode assymetry.

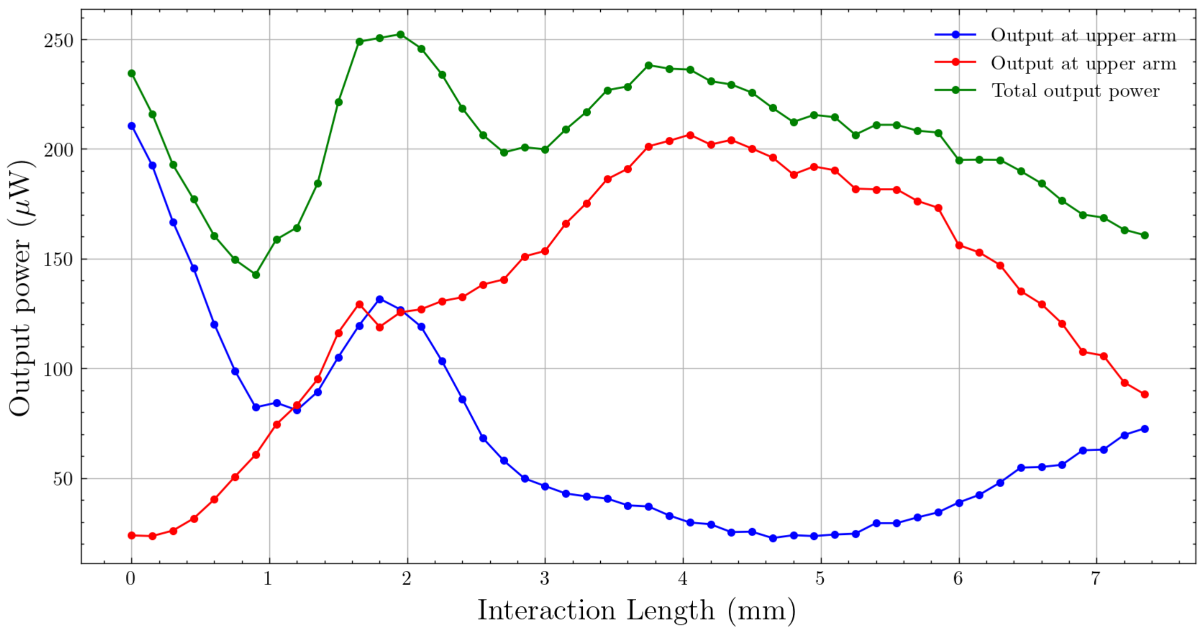

Figure 4.12: Output optical powers of the upper and lower arms, and total output power as a function of interaction length.

The reflectivity as a function of interaction region separation is present in figure 4.13.

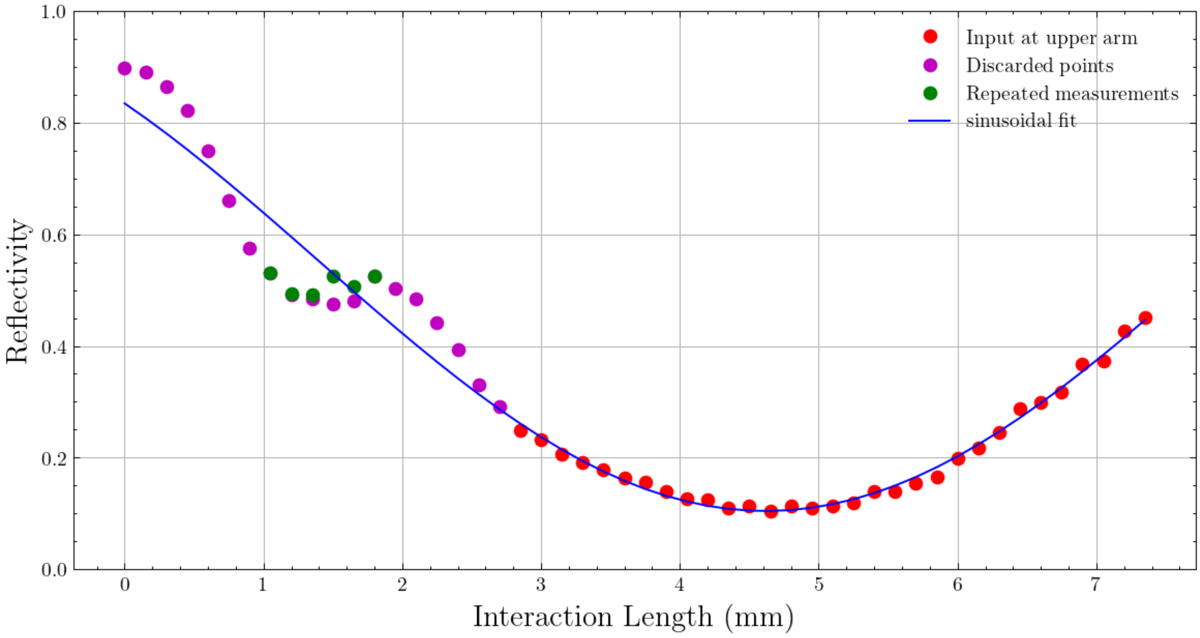

Figure 4.13: Reflectivity of directional couplers with 20 μm separation as a function of interaction length.

The red and purple points represent reflectivity measurements made from the upper input arm of the directional couplers. A sinusoidal behavior could only be observed for interaction lengths higher than 2.7 mm, with only the red points being used on the fit, while the purple points correspond to the unexpected behavior already mentioned. The points in green correspond to measurement repetitions made on the most poorly behaved zone, with some of them overlapping with the original points, reinforcing the idea that the error is not contained in the measurement process. A full period was not obtained, since, as expected, a higher separation translates to less coupling, which increases the coupling length. A full range of modulations was also not achieved, with the minimum value being of 0.10, pointing at mode asymmetry. From the sinusoidal fit, the following parameters were obtained:

	F	β_c (rads/mm)	ϕ_0 (rads)	κ (rads/mm)	Δ (rads/mm)	L_c (mm)	r^2
value	0.896194	0.245720	0.4330	0.232617	0.07917	6.3926	0.992
uncertainty	0.000006	0.000005	0.0001	0.000005	0.00002	0.0001	

Table 4.3: Parameters of set of directional couplers with 20 μm separation.

As it was expected, a non-unitary F points to a non-complete power transfer between arms and mode asymmetry. This result is reinforced by the high value of Δ, which is expectedly smaller than that obtained for the previous case. Since the waveguides are further apart, they do not overlap as much, resulting in a smaller mode asymmetry. The incomplete modulation could also be explained by the simultaneous propagation of multiple modes, however, that is highly unlikely, since, from the CCD images made on the waveguide with these fabrication parameters, an approximately gaussian intensity distribution was observed, indicating monomode operation. As expected, the value of κ is smaller than what was obtained before, which can be explained by the weaker mode superposition. The coupling length showed an increase from the last value due to the decreased β_c. The phase introduced by the s-bends, ϕ_0 also decreased in relation to the previous case, a result that comes from the higher distance between the s-bends, reducing power transfer.

Due to the non-predictable behavior of the devices on the 50:50 power splitting region, this separation will not be used to produce 50:50 directional couplers, although the smaller reflectivity variation around this zone, paired with the small interaction length would allow for more compact devices compared to those obtained with 15 μm separation.

For the last set of devices, with 25 μm separation, averaging the output powers of the last three straight waveguides allowed for the determination of an IL of 3.31 $\pm$ 0.02 dB. This value is a bigger jump than that from 15 μm to 20 μm, which can be attributed to defects or dirtiness on the material, a different inscription depth, or bad polishing. Figure 4.14 shows the output powers in the upper and lower arms, as well as the total output power as a function of interaction length.

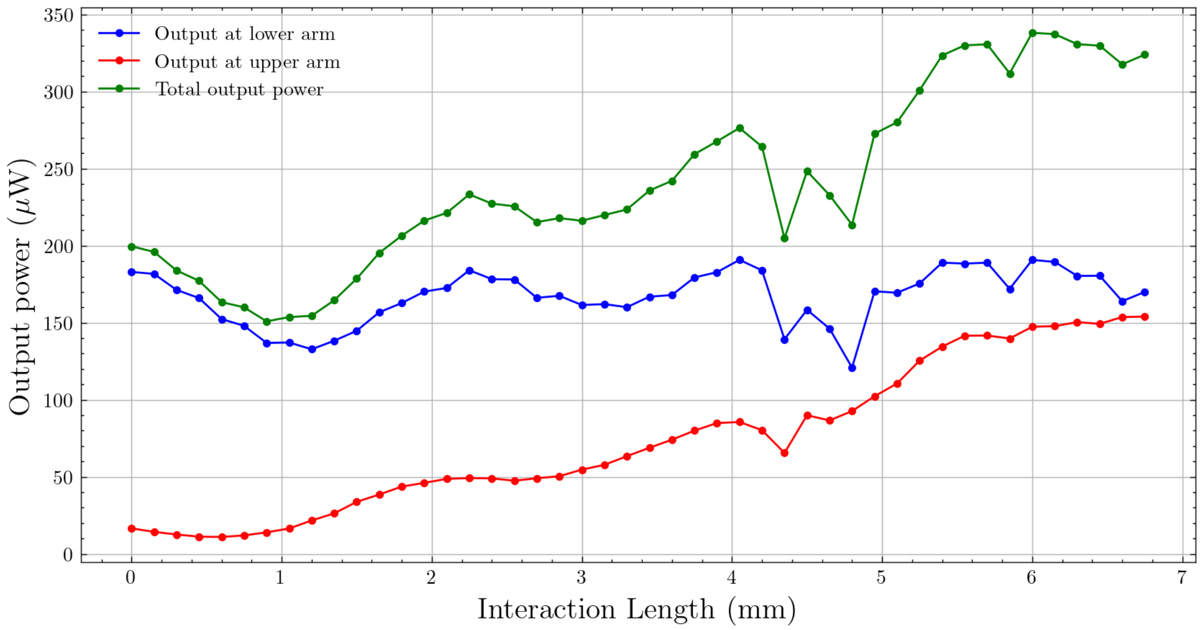

Figure 4.14: Output optical powers of the upper and lower arms, and total output power as a function of interaction length.

A very unexpected behavior was observed, with the total output power increasing as opposed to the decreasing tendency that has been observed. This result comes from the **quasi-**

	F	β_c (rads/mm)	ϕ_0 (rads)	κ (rads/mm)	Δ (rads/mm)	L_c (mm)	r^2
value	0.4945	0.1535	0.3290	0.1079	0.1091	10.24	0.97
uncertainty	0.0008	0.0003	0.0002	0.0002	0.0006	0.03	-

Table 4.4: Parameters of set of directional couplers with 25 μm separation.

monotonous, yet oscillating increase in output power observed at the upper arm, while for the lower arm, an approximately constant output power is observed. The secondary oscillation on both arms can be caused by coupling to non-propagating modes. The lower arm also shows an irregular drop in between the 4 and 5 mm in interaction length, probably caused by defects on the waveguide, poor edge coupling, or bad polishing/cleanliness.

Figure 4.15 shows the reflectivity as a function of interaction length for these devices.

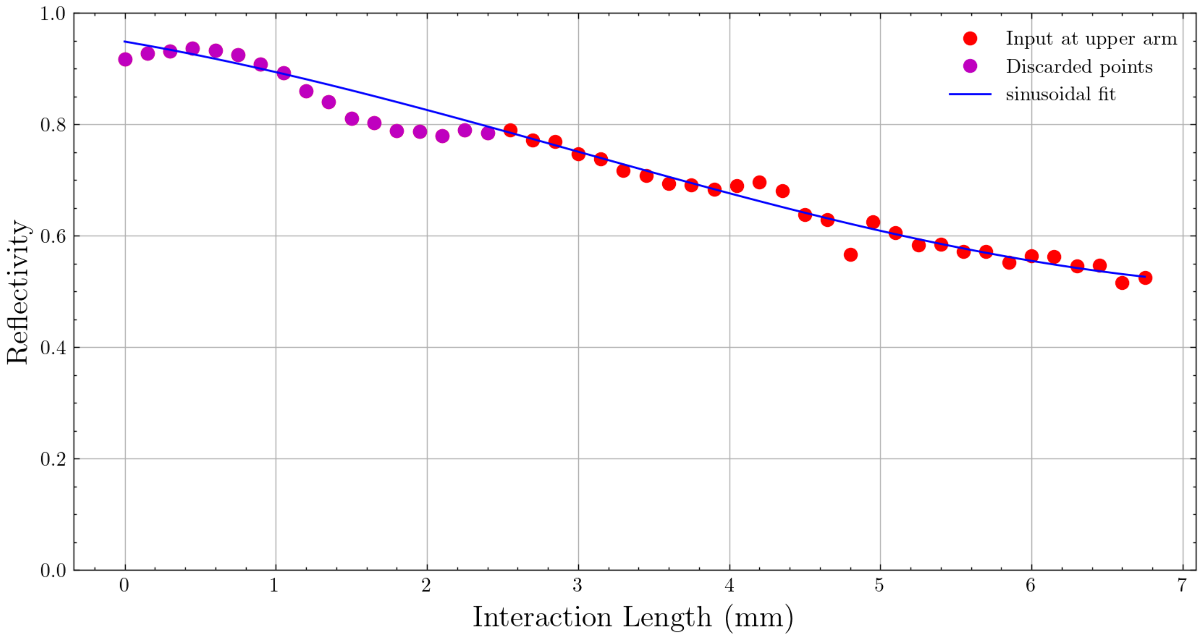

Figure 4.15: Reflectivity of directional couplers with 25 μm separation as a function of interaction length.

Even though this set of waveguides have an irregular behavior, a full period of oscillation was not expected, since this is the highest separation value tested. This was, indeed, the case. The secondary oscillatory behavior is once again observed until an interaction length of 2.40 mm. The purple points were discarded from the fit, since they present an undesired secondary oscillation. A very low value of F was obtained, which, once again, was not to be expected. This value, paired with the high value of Δ strongly indicates mode asymmetry, an unexpected result, given that the waveguides are farther apart than the previous sets. The decrease in κ, however, is to be expected. The higher separation of the s-bends also explains the lower ϕ_0 value. A higher coupling length was also to be expected.

To better study a full range of light modulation, specially the interaction length for which 50:50 power splitting is achieved, several directional couplers were produced for interaction lengths between 1 and 6 mm with a 15 μm separation (s_i). In total, 23 interaction lengths were studied, each having 5 identical couplers to ensure repeatability, creating a total of 115 devices. The increment in interaction length is of 172 μm. Below the directional couplers and after the first set of 10 interaction lengths (50 couplers), 3 straight waveguides were produced to assess the minimum achievable losses. For the first set, insertion losses of 2.70 $\pm$ 0.03 dB were obtained, while for the second set, 3.11 $\pm$ 0.06 dB, which is still a significant jump that, as usual, could be attributed to different substrate cleaning/polishing conditions.

As before, the output optical power through the upper, lower, and both ports was studied, and the results are depicted in figure 4.16. Once again, there is power oscillation between waveguides. Power transfer, however, is not complete due to waveguide assymetry. Total power, as in the last time, tends to decrease probably due to the previously mentioned non-propagating modes.

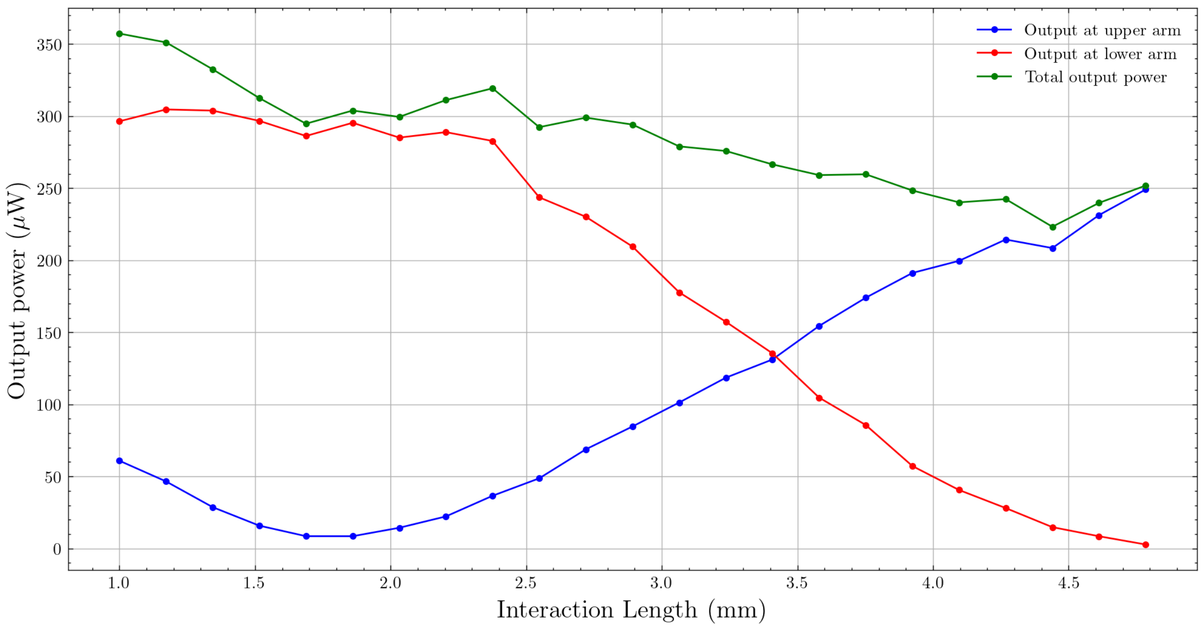

Figure 4.16: Output optical powers of the upper and lower arms, and total output power as a function of interaction length for 15 μm separation.

The average reflectivity is represented as a function of interaction length on figure 4.17. The error bars represent the sample standard deviation. Also plotted was the first set of points obtained for a 15 μm separation, for comparison.

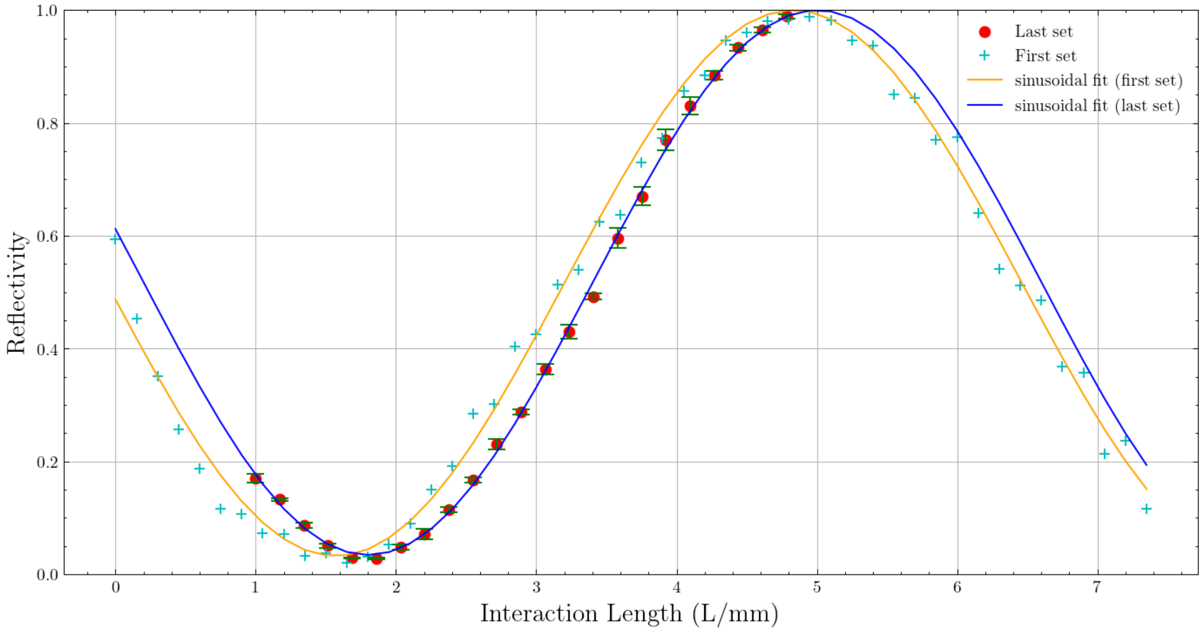

Figure 4.17: **Red:** Full modulation interval of directional couplers with 15 μm separation; **Cyan:** First set of directional couplers with 15 μm separation.

The fit is the same as in the previous cases and, as it can be seen, it produces an even better correspondence to the data points ($r^2 = 0.999$) than what was obtained in the first set of directional couplers with 15 μm separation ($r^2 = 0.991$).

	F	β_c (rads/mm)	ϕ_0 (rads)	κ (rads/mm)	Δ (rads/mm)	L_c (mm)	r^2
value	0.96575	0.49080	0.6863	0.48233	0.0908	3.20046	0.999
uncertainty	0.00001	0.00001	0.0001	0.00001	0.0001	0.00009	-

Table 4.5: Parameters of new set of diretional couplers with 15 μm separation.

The first feature to notice is the absence of full modulation, with the minimum reflectivity value achieved being 0.024, higher than the minimum of 0.014 achieved earlier for the same separation. The amplitude of modulation, F, shows a slight decrease from the previous value, which sits at 0.967. On the other hand, this set of devices contains a higher asymmetry than in the previous case (0.0867 rad/mm), and therefore, higher than the other two sets of devices, possibly pointing to a higher device superposition. The initial phase introduced by the s-bends ϕ_0 is smaller than that obtained for the first set (0.8016 rads), but still higher than those obtained for 20 μm separation (0.433 rads) and 25 μm separation (0.37 rads). This reflects on the observed shift to the right of this set in relation to the first set of devices analyzed, and it points to a stronger coupling in the s-bend regions. The β_c value shows a small increase from the previous 0.488 rads/mm obtained, which also corresponds to a slightly smaller L_c.

Since these devices were produced in different runs, fabrication conditions were slightly different, including laser power, substrate alignment, polarization, inscription depth, and many others. Since device characteristics are very sensitive to fabrication conditions, some variability is to be expected. Overall, this set of devices present much more robust results, reducing the fabrication and measurement variability, allowing for a closer view of the underlying behavior. Keeping this in mind, the fit was used to determine the best interaction length for which a 50:50 power splitting is achieved, corresponding to 3.369 mm.

4.6 Conclusion

In this chapter, several fundamental optical devices were succesfully produced and studied. The first step consisted on fixing several fabrication parameters for all produced devices, such as repetition rate (1MHz), numerical aperture (0.42), beam polarization (parallel to writing direction), and inscription depth (50 μm).

Next, by varying pulse energy and writing speed, several straight waveguides were studied for their insertion, coupling and propagation losses, as well as their MFD in the X and Y directions. It was seen that coupling losses, as well as MFD in both directions, tend to increase with increasing laser pulse energy, most probably due to the higher modification volume, which resulted in larger mode diameters. For the same and every pulse energy, coupling losses and MFD tend to decrease with increasing writing speed, probably due to the smaller fluence which results in smaller modified volumes and, therefore, smaller modes. Only the 125 nJ set showed the inverse behavior, slightly increasing for 80 mm/s. Here, the decreased refractive index contrast caused by the smaller fluence may have lead to a weaker confinement, increasing the mode size despite the smaller modified volume. For a given writing speed, propagation losses showed an increase with decreasing pulse energies. The smaller confinement seen at lower pulse energies leads to more propagation on the cladding, where more defects are present, translating into higher losses. This smaller confinement is also observed at the same pulse energy and increasing writing speed, where fluence diminishes. The only exception is the 200 nJ set, where propagation losses seem to be independent of writing speed. Overall, a pulse energy of 150 nJ and a writing speed of 35 mm/s were chosen for the next devices.

S-bends were also studied for their losses at varying curvature radii. By fixing the vertical offset at 112.5 μm, it was found that bending losses decrease as radius increases, approaching the asymptotic losses of straight waveguides produced in the same substrate, as expected. A compromise between losses and compactness had to be found, and a 70 mm radius was chosen for future designs with bending losses of 0.97 dB, since it is already very close to the minimum obtained value (0.35 dB @ 90 mm). A decaying exponential behavior was also observed for the bending losses per centimeter, as predicted by equation (3.14). It was also found that for a radius of 70 mm, the bending losses per centimeter are of 1.73 dB.

Regarding the directional couplers, three interaction region separations were tested, 15, 20 and 25 μm and, for each one, several interaction lengths were tested. For a 15 μm separation, an oscillatory behavior was observed, indicating power transfer between the arms. Total power transfer decreased with increasing interaction length, possibly due to coupling with non-propagating modes. The fit parameters revealed device asymmetry, with an F of 0.9675 $\pm$ 0.00001, an asymmetry Δ of 0.0867 $\pm$ 0.0003 rads/mm, an initial phase ϕ_0 of 0.8152 $\pm$ 0.0006 rads induced by the s-bends, and other parameters were determined, namely a β_c of 0.48148 $\pm$ 0.0003 rads/mm, a coupling coefficient κ of 0.47359 $\pm$ 0.00003 rads/mm, and a coupling length L_c of 3.2625 $\pm$ 0.0001 mm.

For the 20 μm separation, power transfer is still visible, however an unexpected behavior is observable at small interaction regions. This could be due to coupling to non-propagating modes, or propagation of multiple modes with different coupling coefficients, although the intensity profile of the waveguide produced with these fabrication parameters showed a gaussian power distribution, indicating monomode operation. Producing a fit with the most well behaved points allowed for the determination of F = 0.896194 $\pm$ 0.000006, Δ = 0.07917 $\pm$ 0.00002 rads/mm, ϕ_0 = 0.4330 $\pm$ 0.0001 rads, β_c = 0.24572 $\pm$ 0.00005 rads/mm, κ = 0.232617 $\pm$ 0.000005 rads/mm, L_c = 6.3926 $\pm$ 0.0001 mm and r^2 = 0.992. A higher asymmetry is observed than on the previous case, which is to be expected, since the waveguides in the interaction region are further apart. The smaller initial phase reveals the weaker influence of the s-bends on power transfer between arms. A higher coupling length was also expected.

For the 25 μm separation, power transfer is observable, with power at the upper arm increasing for higher coupling lengths, however, power at the lower arm does not seem to be decreasing, and, as a result, total output power is increasing, which is the opposite behavior than the one observed for the previous sets. This power increase could be due to different polishing and cleanliness conditions. A secondary oscillatory behavior is also seen for both arms, which could indicate coupling between modes of higher order although, as explained before, this is highly unlikely. Overall, this set of devices did not provide any conclusive results.

To better study a full period of modulation, 115 couplers were produced with a 15 μm separation and varying interaction lengths. Once again, oscillatory power transfer between arms was observed, as well as a decreasing total power due to the reasons previously mentioned.

It was not possible to achieve a full range of reflectivities, with the minimum value being of 0.028, which arises from waveguide assymetry. Overall, the expected sinusoidal behavior of the reflectivity was observed and an interaction length (L_i) of 3.369 mm was chosen for the production of 50:50 couplers.

5 Mach-Zehnder Interferometers

This chapter revolves around the design and study of Mach-Zehnder interferometers.

In section 5.1 a brief theoretical introduction to the workings of Mach-Zehnder interferometers is given. The mechanism by which a phase-shift is achieved is also depicted here.

The choice of microheater materials as well as the laser parameters used to produce them are explained in section 5.2. Several laser writing speeds and pulse energies are analyzed in order to find the configuration that ensures electrical isolation between both sides of the mark.

In section 5.3, the inscription of MZIs and their reflectivities are measured before and after depositing the metal layer.

In section 5.5, great detail is given to microheater production, and active modulation of the devices is achieved, with focus being given to the power necessary for a 2π phase shift, device temporal response and bandwidth.

In section 5.6, the same MZI is characterized before and after introducing an isolation area around the microheater to assess if it introduces an increase in efficiency.

5.1 Background

5.1.1 Working Principles

A Mach-Zehnder interferometer consists of a series combination of two beam-splitters, which in our case will be achieved by the introduction of 50:50 directional couplers, and a phase-shifter in between them. The latter component introduces a shift on the propagating light wave which, when interacting with light from the lower arm through the last coupler, produces interference, allowing for light modulation. Figure 5.1 shows a schematic representation of this device.

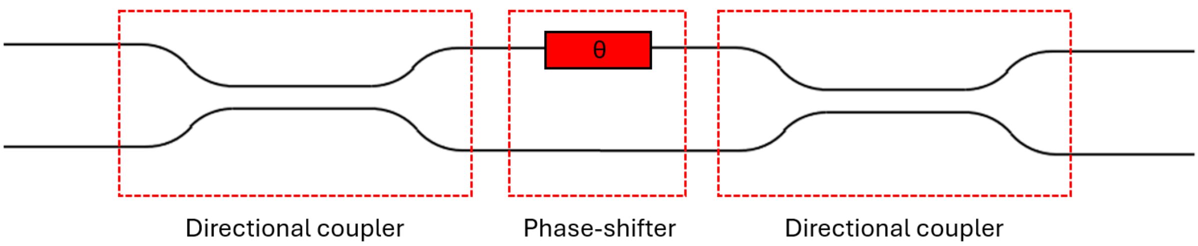

Figure 5.1: Schematic representation of a MZI and building blocks.

A matrix treatment of this device's fundamental components is presented. As it was seen in the last chapter, the transfer matrix of a directional coupler is given by:

$$DC = \begin{bmatrix} e^{-i\Delta L_i}\left(\cos\phi - i\frac{\Delta}{\beta_c}\sin\phi\right) & e^{-i\Delta L_i}\left(\frac{-i\kappa}{\beta_c}\right)\sin\phi \\ e^{i\Delta L_i}\left(\frac{-i\kappa}{\beta_c}\right)\sin\phi & e^{i\Delta L_i}\left(\cos\phi + i\frac{\Delta}{\beta_c}\sin\phi\right) \end{bmatrix} \tag{5.1}$$

Here, $\phi = \beta_c L_i + \phi_0$, for simplification.

Since the phase-shifter only introduces an additional phase in the upper arm, given by θ, this component's transfer matrix is simply:

$$\begin{bmatrix} e^{i\theta} & 0 \\ 0 & 1 \end{bmatrix} \tag{5.2}$$

The transfer matrix for the MZI is given by:

$$MZI = DC * PS * DC \tag{5.3}$$

By simulating this matrix in jupyter notebook, it was found that, given arbitrary parameters F, β_c and ϕ_0, the reflectivity of an MZI varies sinusoidally with the phase θ of the phase-shifter. An interesting find is that the asymmetry parameter Δ introduces an horizontal shift on this behavior. By assuming a small Δ and directional couplers with arbitrary ϕ, the reflectivity of an MZI depends on θ through equation (5.5). Indeed, the DC matrix can be decomposed on the following product:

$$DC = \begin{bmatrix} e^{-i\Delta L_i} & 0 \\ 0 & e^{i\Delta L_i} \end{bmatrix} \begin{bmatrix} \cos\phi + i\frac{\Delta}{\beta_c}\sin\phi & \left(\frac{-i\kappa}{\beta_c}\right)\sin\phi \\ \left(\frac{-i\kappa}{\beta_c}\right)\sin\phi & \cos\phi - i\frac{\Delta}{\beta_c}\sin\phi \end{bmatrix} \tag{5.4}$$

The first matrix corresponds to an additional shift to the phase given by the phase shifter equivalent to making the substitution $\theta \to \theta + 2\Delta L_i$.

$$R = 1 - \sin^2(2\phi)\cos^2\left(\frac{\theta}{2}\right) \tag{5.5}$$

It is found that complete power transfer only happens when 50:50 power splitting is achieved.

5.1.2 Thermal phase-shifters

Thermal phase-shifters will provide the phase difference necessary for light modulation. When a temperature difference is applied to the arms of the interferometer, the phase on each arm will be shifted by a different ammount. That happens because EAGLE2000 glass, as with many other glasses [75], possesses a significant thermooptic coefficient n_t, which relates a variation in local temperature (δT) to a variation in refractive index (δn):

$$\delta n = n_t \delta T \tag{5.6}$$

This difference in refractive index between the two arms will translate to a difference in the phase of modes propagating in the upper and lower arms, producing interference. The microheater is placed on the surface of the substrate directly above one of the arms. It has the same length as the interferometric arm and a rectangular cross-section. This symmetry ensures that each arm has a uniform temperature, while possessing different temperatures between one another. The phase difference between the arms is given by:

$$\Delta\theta = \frac{2\pi n_t L_{arm}}{\lambda_0} \Delta T \tag{5.7}$$

Here, λ_0 is the wavelength of propagating light in the vacuum and ΔT is the temperature difference between the arms. Assuming that the microheater is an infinitesimaly thin wire (l/w $\gg$ 1) and no electric power is dissipated into the air, the temperature difference can be deduced by solving the stationary heat conduction equation with appropriate boundaries:

$$\Delta T = \frac{P_e}{\kappa_t \pi L_h} \log\left(\frac{\rho_2}{\rho_1}\right) \tag{5.8}$$

P_e is the power dissipated from the microheater as heat, κ_t is the thermal conductivity of the material, L_h is the length of the microheater, and ρ_1 and ρ_2 are the radial distances of the farthest and closest interferometric arms, respectively.

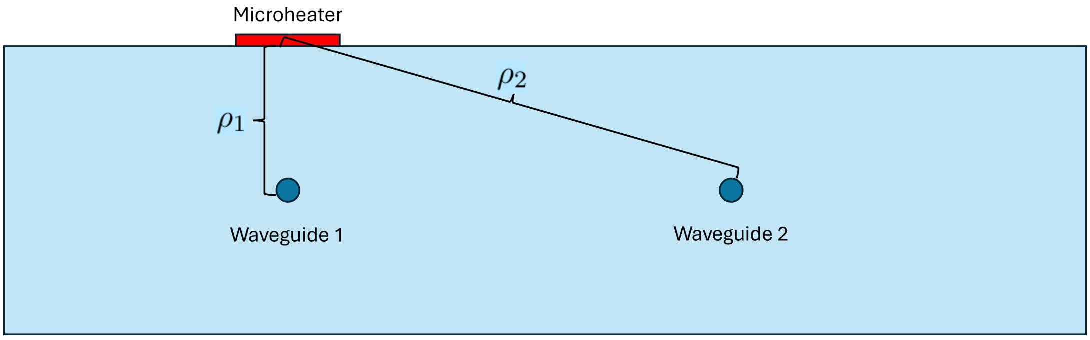

Figure 5.2: Schematic of the cross-section of the substrate with the microheater.

By joining equations (5.7) and (5.8), we get the following expression for the dependence of the phase difference ($\Delta\theta$) on microheater power (P_e):

$$\Delta\theta = \underbrace{\frac{2n_t}{\lambda_0 \kappa_t} \frac{L_{arm}}{L_h} log\left(\frac{\rho_2}{\rho_1}\right)}_{\alpha} P_e \tag{5.9}$$

The α coefficient directly relates electrical power dissipation to the phase shift in the arm [4]. Here, the length of the interferometric arm will always match that of the microheater, thus:

$$\alpha = \frac{2n_t}{\lambda_0 \kappa_t} log\left(\frac{\rho_2}{\rho_1}\right) \tag{5.10}$$

By using the value of n_t estimated by [3] for CORNING EAGLE XG, a borossilicate glass similar to EAGLE2000, and the κ_t value given by [76], α can be estimated as 20.36 rads/W and the power needed to produce a 2π phase-shift, $P_{2\pi}$ = 309 mW.

5.1.3 Microheater Characteristics

The microheaters used in this work possess the geometry depicted in figure 5.3.

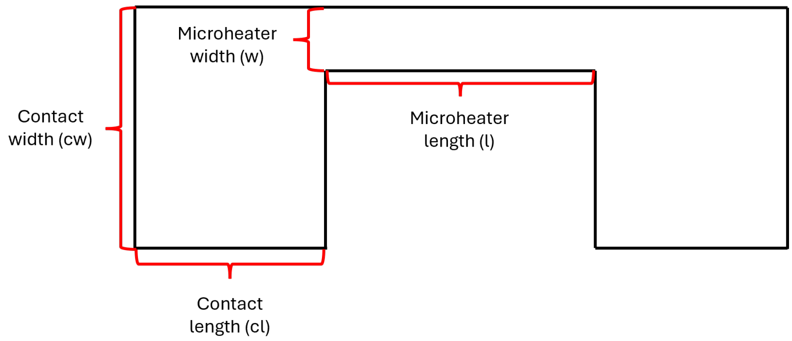

Figure 5.3: Schematic of top view of employed microheater.

The heating only happens in the thinner portion of the device, with contact to the external circuit being made through the contact pads with tungsten needles.

Based on the image, the resistance can be calculated through the following formula:

$$R = R_{sh}\frac{l}{w} \tag{5.11}$$

, where $R_{sh} = \rho/h$ is the sheet resistance of the gold film, which corresponds to the resistance of an arbitrary sized square sheet of gold when measured between opposite sides of the square, in units of ohms per square ($\Omega/\square$); l and w correspond, respectively, to the length and width of the microheater, and they are the main parameters that will determine the resistance of the microheater.

It is important to note that the microheater resistance (R_{ts}) exhibits a dependence on the dissipated electrical power (P_{ts}). This is due to the dependence of resistance on operating temperature, which increases when power is increased. This relation is given by [3]:

$$R_{ts} = R_0 + \gamma P_{ts} \tag{5.12}$$

Here, R_0 is the resistance of the microheater when no current is passing through.

5.2 Microheater Patterning

A thin sheet of gold was used for the microheaters, since it is not prone to oxidation, making its connection to an external circuit an easy task. For the gold to adhere to the substrate, a chromium layer was deposited, with a thickness that cannot be either too thick nor too thin. If the layer is too thick, heating to only about 200ºC would cause the chromium atoms to start diffusing into the gold layer, altering the resistivity of the gold layer over time; and it cannot be too thin, otherwise the adhesion to the substrate would be too weak. Flamini et al. [3] verified, with manual tape pull tests, that the ideal thickness of this layer would be 2 nm.

Since the available sputtering machine only has a resolution of 5 nm of deposition thickness, although it is not ideal, this was the chosen value for the chromium layer. A thickness of 100 nm was chosen for the gold layer. The microheaters were produced using the femtosecond laser unit, and as such, the optimal exposure conditions must be found that provide the best electrical isolation. To that end, the laser repetition rate was changed to 500 kHz, and the focusing lens was swapped for a MituToyo 10 x objective with a MituToyo ring, providing a numerical aperture of 0.26. A smaller numerical aperture increases the distance between the objective and the focus, avoiding possible ablated gold from making contact with the lens, damaging it. The sample was characterized with an optical microscope and a profilometer.

Two sets of marks were written, one on the +X and another one on the +Y directions. On each set, pulse energy and writing speed were varied between 117 and 1114 nJ, and 0.05 and 4 mm/s, respectively, while keeping the writing polarization parallel to the writing direction.

The microscope images of the +X and +Y marks for the same pulse energy and writing speed do not show significant differences in laser patterning, thus, only the +X marks will be shown here. The +Y marks are available in the Annex.

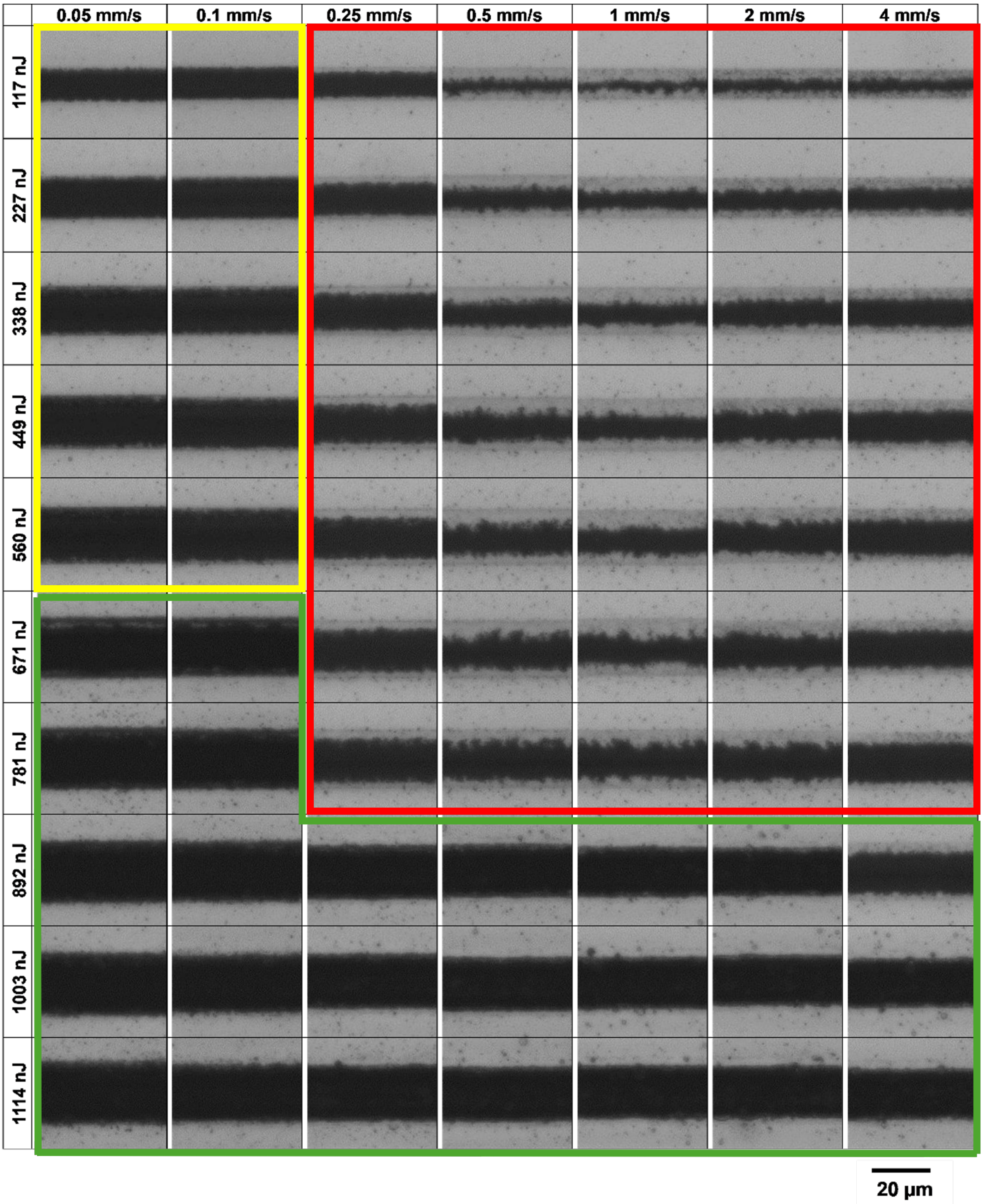

Figure 5.4: Microscope images of ablation marks made on a gold surface along the +X direction. **Red:** Partial gold removal; **Yellow:** Total gold removal; **Green:** gold and glass removal. A special thanks to João M. Maia for providing these images and his insights.

From the microscope images and profilometry, three ablating regimes were observed: partial gold removal (first regime), where the depth of the groove made on the surface reaches 100 nm, however gold removal is not uniform; total gold removal (second regime), where the depth of the groove is still 100 nm, however gold removal is uniform; and gold and glass removal (third regime), where glass is removed along with the gold, guaranteeing electrical isolation. From figure 5.4, the first regime is easily observed for writing speeds higher or equal to 0.25 mm/s and pulse energies smaller than 800 nJ. For all marks, the depth of the groove is approximately 100 nm, however the microscope images show a non-uniform pattern, with the darker area corresponding to the region of total gold ablation and a gray area where only partial ablation is observed. This set of parameters does not guarantee electrical isolation. The second regime can be seen for writing speeds equal to or smaller than 0.1 mm/s and pulse energies inferior to 600 nJ. Groove depths of approximately 100 nm, paired with microscope images that present uniform ablation profiles ensure a steady removal of the gold layer. The green region in figure 5.4 comprises the set of parameters for which both gold and glass are removed from the substrate. This is the regime that ensures electrical isolation and will allow for the reliable production of microheaters. As expected, for a fixed writing speed, an increase in pulse energy translates to a raise in ablation width, which reaches a plateau in the 20 nm at energies greater than 800 nJ. Conversely, for a constant pulse energy, increasing the writing speed results in a slight decrease in ablation width, and a transition from a uniform ablation profile to a irregular one, except for energies greater than 800 nJ, with higher writing speeds being needed for this transition to happen. For all profiles, black dots are observable which correspond to gold particles and ablated glass that were shot out of the substrate during patterning. To achieve fast device prototyping, while also ensuring reliable electrical isolation, a pulse energy of 1000 nJ and a writing speed of 2 mm/s were chosen for the microheater patterning.

5.3 Waveguide characterization

The first step in producing an MZI is the inscription of two 50:50 directional couplers in series with a straight section in between that will act as the phase-shifter. In this section, the fabrication method employed on these devices is discussed and the choice of geometric parameters is explained.

Three reference marks are made on the corners of the substrate with high laser intensity. Once the metal layer is deposited on top of the substrate, these marks will remain visible and serve as a reference for the correct placement of the microheaters. As usual, the laser and geometrical parameters employed for the production of the last devices were used, and the interaction length allowing for 50:50 directional couplers was also chosen.

The length of the arms connecting the two DCs was varied from 1 to 10 mm in steps of 1 mm. The length of the microheater will be made to match that of the interferometric arm, thus changing this length does not change α, as equation (5.10) suggests, thus it does not alter the power needed for a given phase-shift. It will, however, change the operating temperature of the microheater for a given dissipated power, with a longer heater corresponding to a lower operating temperature. This has the advantage of avoiding sudden combustion of debris surrounding the heater, which could damage it and possibly render it useless. Thus, a compromise must be made between device compactness and functionality. Three identical devices were made for each arm length, which were spaced from each other by 300 μm. Above and below the interferometers, 3 straight waveguides were produced to assess the minimum losses. In this section, the MZIs are analyzed before and after the chromium + gold layer deposition.

The average insertion losses on the lower and upper waveguides, before and after gold deposition are depicted in table 5.1.

	Before deposition/dB	After deposition/dB
Lower waveguides	3.4 ± 0.3	3.7 ± 0.2
Upper waveguides	3.11 ± 0.06	4 ± 2

Table 5.1: Propagation losses before and after deposition

Before gold deposition, the insertion losses on the lower and upper waveguides do not show a significant difference, however, after deposition, both of these values increase, possibly meaning that some gold was erroneously deposited on the input and/or output facets of the substrate. Although the side surfaces were thoroughly cleaned with acetone and deionized water, some gold might not have been removed, partially blocking the side facets. This is made clear on the upper waveguides, with one of them possessing insertion losses of 6.24 dB, more than double its value from before deposition, 3.06 dB.

For all the produced MZIs, the reflectivity was measured before and after the gold layer deposition. The results are depicted in figure 5.5.

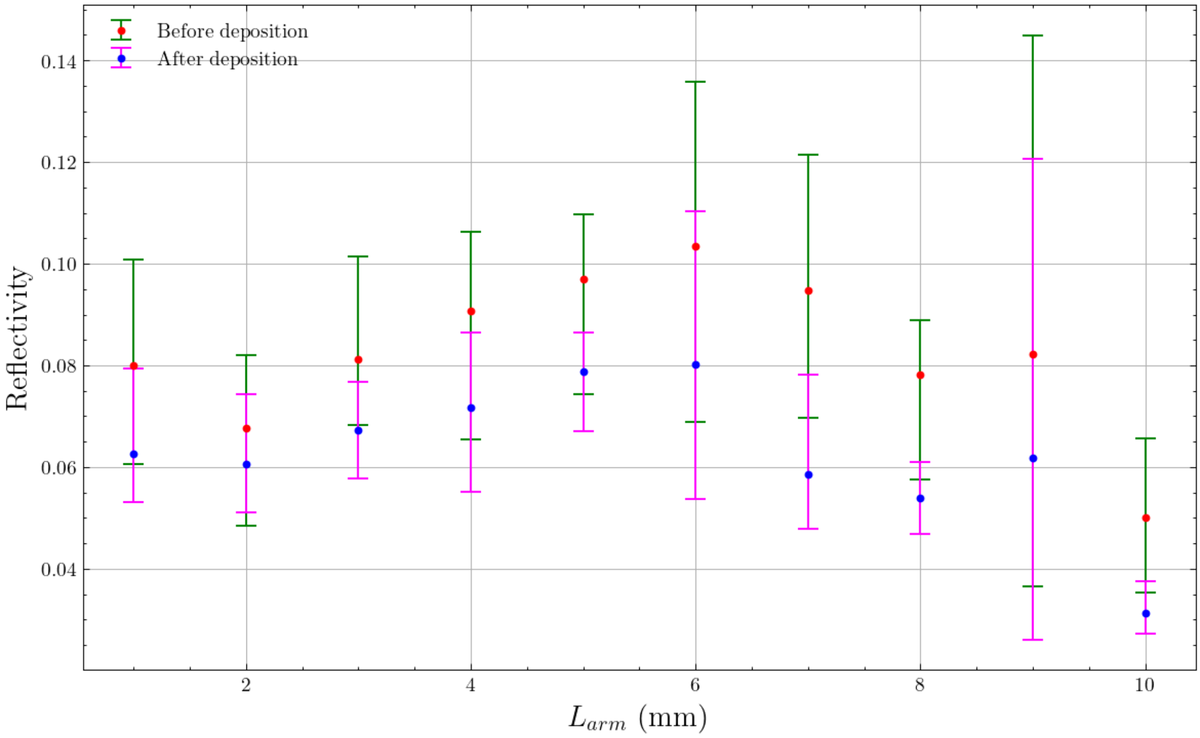

Figure 5.5: Mean reflectivity as a function of the interferometric arms length L_{arm} before and after metal layer deposition. The error bars correspond to the minimum and maximum values achieved.

It would be expected for the reflectivity to be 0 for all devices, however, reflectivities before gold deposition reach a minimum of 0.05. This reflectivity offset can be due to non-50:50 directional couplers, different fabrication conditions on the arms, or the existence of coupler assymetry, the latter ones being the most likely. After deposition, all reflectivity values systematically decrease, with the new minimum being of 0.035, however, since the error bars cover the first set of points, this difference is not significant.

Assuming that the directional couplers have the parameters present in table 4.5, a theoretical value of the reflectivity was calculated, yielding 0.23, which is higher than the obtained range of values.

5.4 Microheater characterization

The reference marks produced in the waveguide inscription step are used to place the microheaters in the right place. For each set of three MZIs with similar interferometric arm lengths, a microheater is designed on the lowermost device. The l/w ratio was chosen to be 100 to validate the approximation made on equation (5.8), ensuring that the microheater is thin enough. To know the resistance, gold resistivity (ρ) must also be known. According to Gilani et al. [77], the resistivity of thin films can become several times higher than that of their bulk form, however, for our case, 100 nm is not thin enough for this phenomenon to be seen, thus, the resistivity of bulk gold, 24.4 nΩm, was used. Using equation (5.11), resistance is estimated at 24.4 Ω. Considering a maximum electrical power dissipation P_{max} of 500 mW, the maximum voltage and current will be of 3.49 V and 143 mA, which are easily handled by the employed power source. On producing the microheaters, ablation width must be taken into account, since it has a considerable value of 20 μm, thus the design made on the SCA program considers this offset. The contact pads have dimensions of 200 μm x 200 μm, which is enough to effectively connect the tungsten micro needles that will make the electrical contact. Before connecting the tungsten needles to the microheater, they were connected to the surrounding gold to assess the short-circuit resistance, yielding $R_{sc} = 4.2\Omega$, which is probably due to oxidation on the needles and resistances inside the measurement circuit. The first device tested was the third smallest, since preliminary tests on the two smallest devices led to their short-circuit, probably due to overheating of surface debris, rendering them useless.

For the third device, the tungsten needles were placed on the contact pads and voltage was raised from 0 to 7.1 V in steps of 0.1 V to assess current, dissipated power, and resistance. Figure 5.6 shows the dependence of resistance on dissipated electrical power.

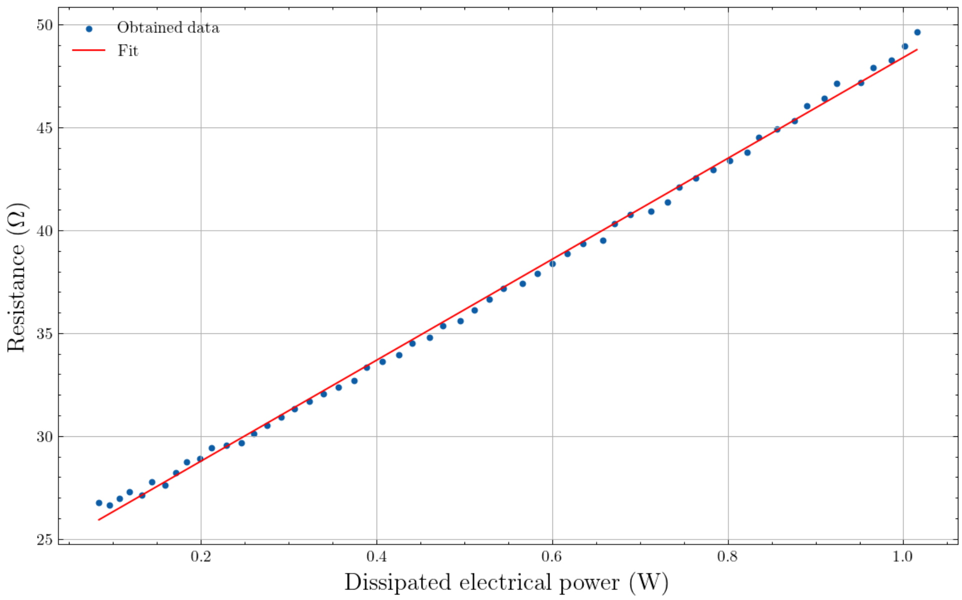

Figure 5.6: Dependence of microheater resistance (R_{ts}) on the disipated electrical power (P_{el}).

A linear behavior can be observed, which was expected by equation (5.12). From the linear fit, and considering the non-zero short-circuit resistance, $R_0 = 19.671 \pm 0.008\Omega$, a relative error by deficit of 19% from the theoretical value was obtained. The value $\gamma = 24.53 \pm 0.02\Omega/W$ was also taken from the fit.

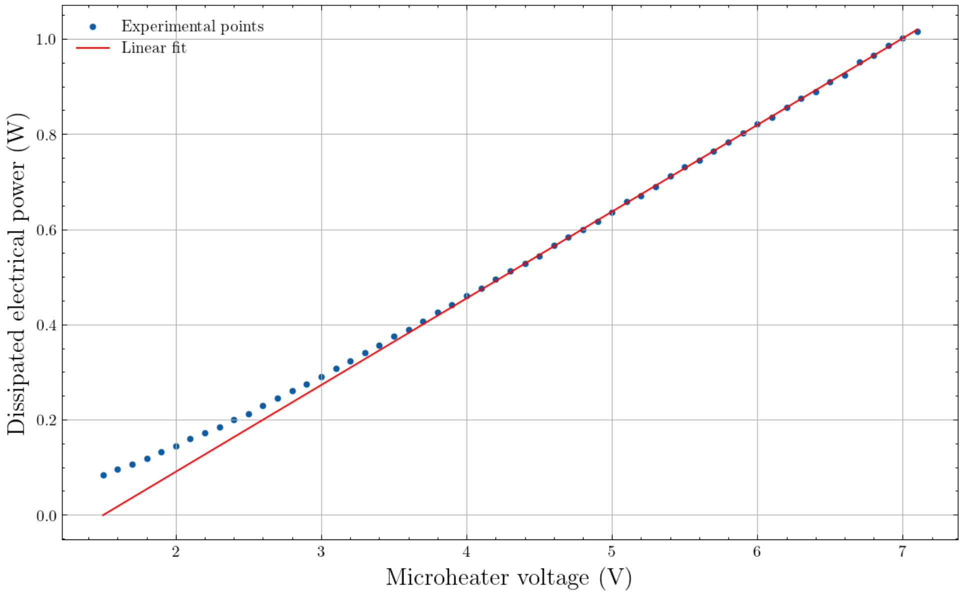

Figure 5.7: Dependence of microheater disipated electrical power (P_{el}) on voltage applied at its terminals.

From figure 5.7 we can also observe an asymptotic linear dependence of the dissipated power on the applied voltage. This result is actually beneficial, since, in the next sections, the dependence of several quantities will be analyzed with respect to dissipated power, however, direct manipulation of this value is not easy, which means that voltage has to be carefully chosen to meet the desired dissipated power. This result indicates that an increase in voltage corresponds to an approximately proportional increase in dissipated power, validating the use of a linear voltage sweep to get moderately uniformly separated dissipated powers.

5.5 Active Modulation

By keeping the tungsten needles in place, an optical fiber was aligned to the upmost input port and a fiber-array possessing two optical fibers with a pitch of 250 μm, similar to that of the fabricated device, was aligned with the two output ports of the third device, possessing an arm length of 3 mm, and voltage on the microheater was raised in steps of 0.1 V, while current, input optical power and output optical power through both ports were monitored. Since it was not possible to perfectly align the fiber-array to the output facet, each output had different losses associated, and thus, only the normalized output power, which is the power through an arm divided by maximum achieved power through that arm, was analyzed. The obtained results are depicted on figure 5.8.

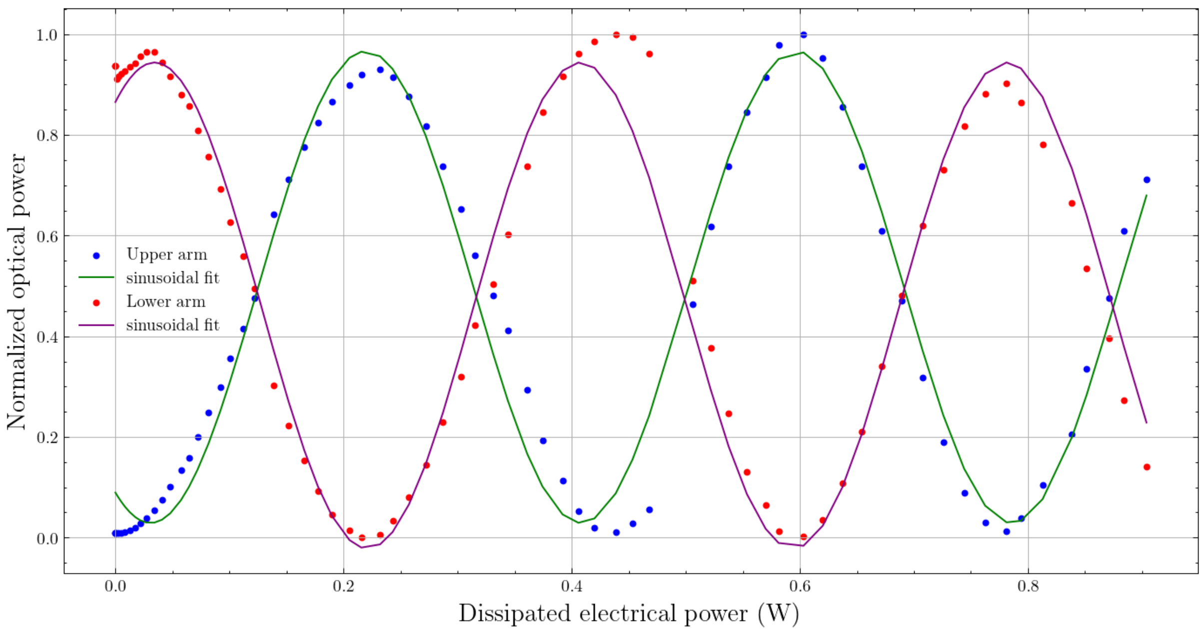

Figure 5.8: Normalized optical power for the upper (blue) and lower (red) output ports with their respective sinusoidal fits.

An oscillatory behavior was observed, as expected, however the maximum output power reached on the upper port, 18,7 μW was significantly smaller than that through the lower port, 87.4 μW. This difference is not due to asymmetric directional couplers. In fact, as figure 5.8 suggests, when maximum power is achieved in one port, an almost null power is observed through the other port. If asymmetry were to be the case, incomplete power transfer would be observed.

This difference in maximum achieved powers can be due to defects on the waveguide, mainly on the upper port after the interaction region, bad polishing or, most likely, the aforementioned poor alignment of the fiber-array.

It is found that the power coming through the upper arm reaches a minimum of 164 nW at an electrical power of 0.9 mW, pointing to an almost complete power transfer. As it is seen in equation (5.5), this behavior is typical of 50:50 power splitters. The small shift in normalized power through the lower arm can be explained by the presence of the aforementioned asymmetry in the couplers, which can exhibit a small Δ. In microheater production, since laser power is enough to produce ablation of the glass, it could also have lead to modifications of the material's residual stress profile [78], leading to a modification of the waveguide's properties through the elastooptic effect, and as a consequence, changing the phase of light.

A sinusoidal fit of the form $f(x, a, b, c, d) = a + b\cos(cx + d)$ was made. From these fits, values for α and Δ were calculated. The values are listed in table 5.2.

	α (rad/W)	Δ (rad/mm)
value	16.743	0.0859
uncertainty	0.005	0.0003

Table 5.2: Parameters for the MZI fit.

The power needed for a 2π phase-shift, $P_{2\pi}$, is of 375.3 $\pm$ 0.1 mW, 21% higher than the theoretical value calculated (309 mW). This was to be expected, since the predicted value is based on the ideal case of an infinitesimal wire, which does not correspond to reality. It can also be due to imperfections on the material or the heater. Another reason stems from the heat absorption and re-emission by the gold surrounding the microheater. This re-emission can heat up the opposite waveguide, raising the necessary power for a desired shift.

The value for Δ is also slightly smaller than that of table 4.5, exhibiting a relative error of 5%.

5.5.1 Response times

To assess the dynamic response of the fabricated device, the microheater was connected to a signal generator and both input signal and output optical power through the upper and lower ports were measured using an oscilloscope. The voltage values for which minimum and maximum optical powers are observed were first determined, yielding 0.04 V and 3.5 V, respectively. A rectangular wave function with these lower and upper boundaries was injected on the microheater and the device's response was studied for several frequency values.

Figure 5.9 shows the device's lower output port response to several frequencies of the input signal. Up until 20 Hz, the device seems to keep up with the change in input, however,for increasingly higher frequencies, the amplitude of modulation keeps on decreasing until no modulation is visible for frequencies higher than 1 kHz.

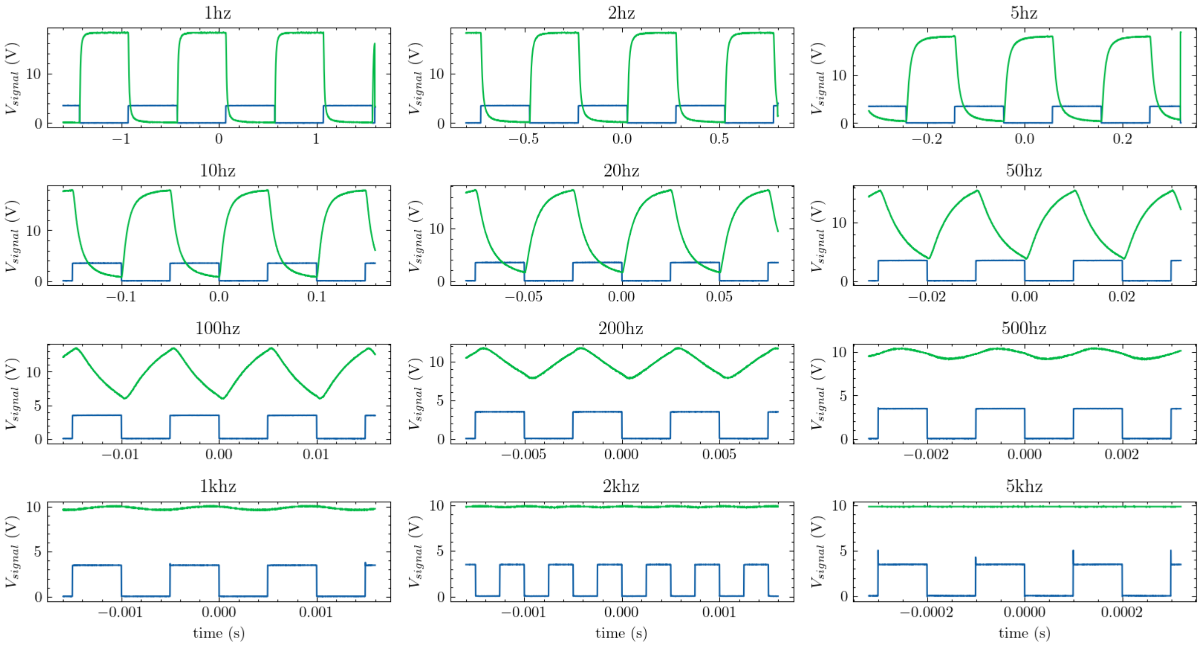

Figure 5.9: Dynamic response of lower output port (green) as a function of input signal (blue) for several frequencies.

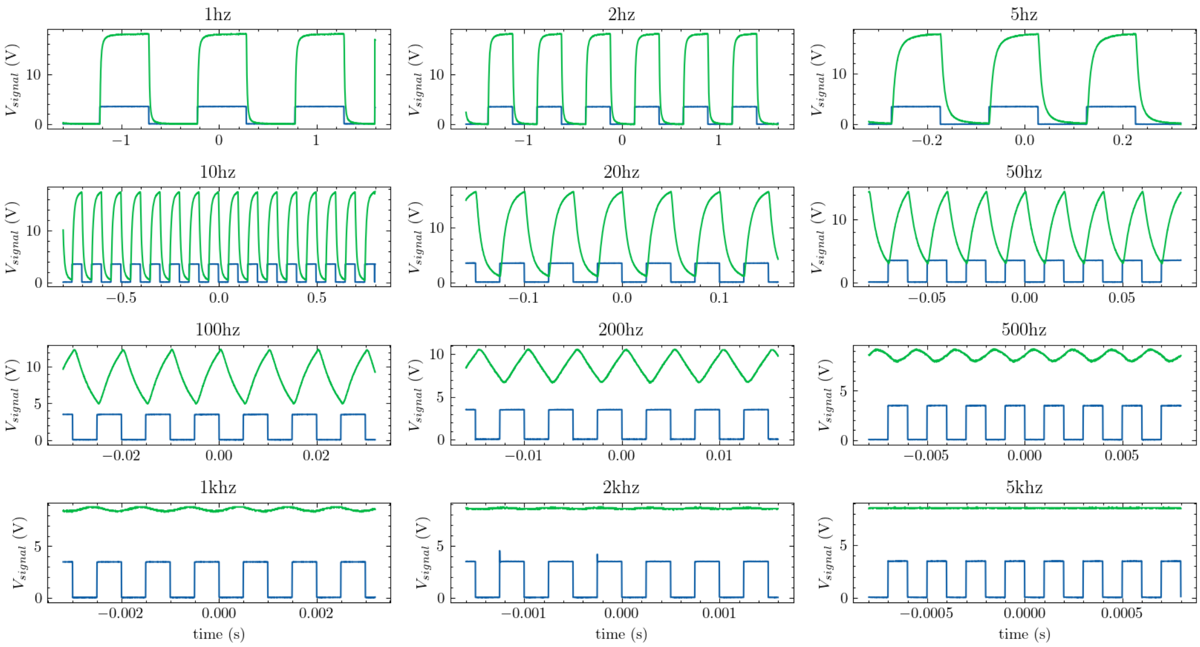

Figure 5.10: Dynamic response of upper output port (green) as a function of input signal (blue) for several frequencies.

For the lower arm, the response is the inverse of that observed on the upper arm, as it would be expected. Still, the modulation only keeps up with the signal until 20 Hz, decreasing significantly in amplitude thereafter.

Response times are defined as the time it takes for the response to go from 10% to 90% of the full modulation [79]. Figure 5.11 shows the response of the system to a step function for both system excitation (t_{rise}) and relaxation (t_{fall}).

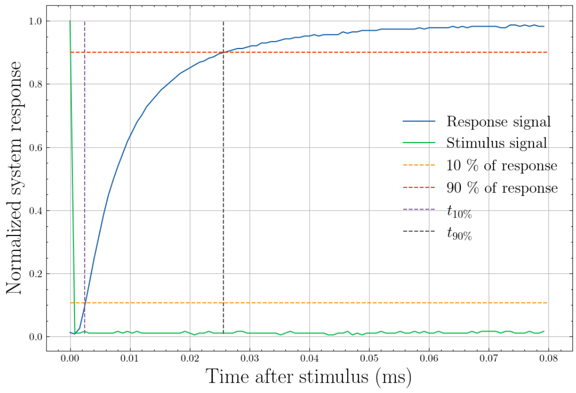

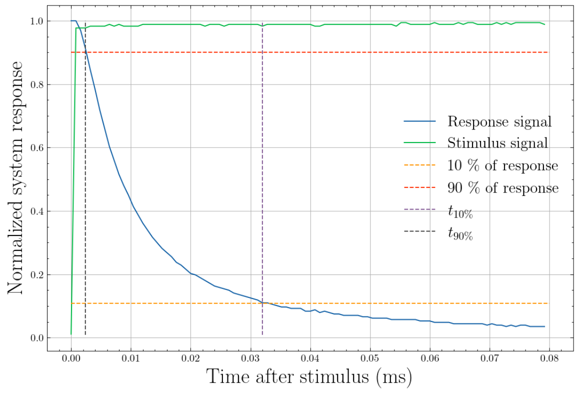

Figure 5.11: System response (upper arm) to a step voltage (t_{rise}) and after turning the stimulus off (t_{fall}).

A rise time of 24 ms is obtained, while the fall time stands at 32 ms, indicating that the material is better at absorbing thermal energy than at dissipating it, probably due to the absence of heat sinks, not providing an efficient way for heat to transfer out of the material. To calculate the bandwidth of this device, the following rough estimation can be employed:

$$f_{bw} \approx \frac{0.35}{t_{rise}} \tag{5.13}$$

, allowing for the estimation of a 14.58 Hz bandwidth.

5.6 Microheater isolation

In the previous section, it was hypothesized that the gold surrounding the microheater could be absorbing and re-emitting heat, raising $P_{2\pi}$. To validate this hypothesis, an MZI was tested before and after removing the surrounding gold. The isolation scheme for gold ablation is displayed in figure 5.12.

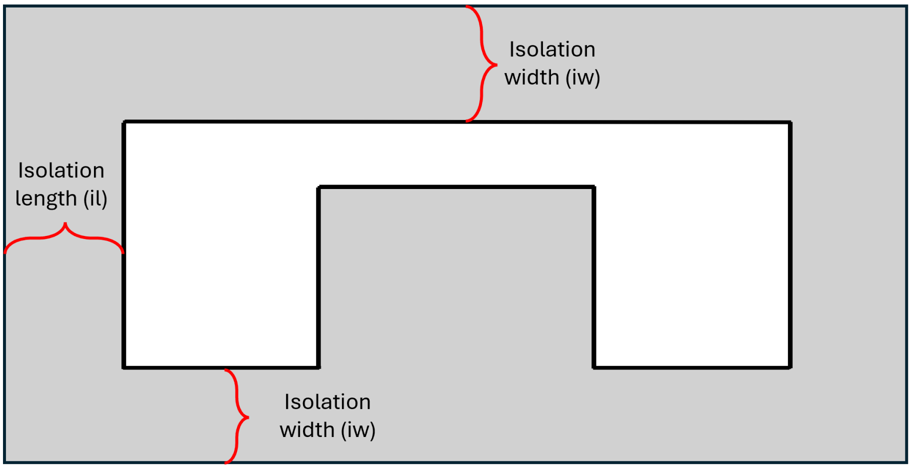

Figure 5.12: Isolation scheme used for the microheater.

The fabrication parameters used for microheater patterning were also applied here. Both the isolation width and length were kept at 150 μm.

Unfortunately, it was not possible to use the already tested MZI, since the microheater stopped working, probably due to overheating of surface debris, short-circuiting the microheater. For this reason, the MZI with the longest interferometric arm produced, of 10 mm, was tested instead. This device was chosen since it possesses the lowest operating temperature for a given phase-shift, having a smaller risk of overheating. It is true that it compromises compactness, however, only the relative change in efficiency will be studied, meaning that this knowledge can be applied to smaller size devices.

Figure 5.13 shows the normalized output optical powers through the lower arm of the MZI without and with isolation.

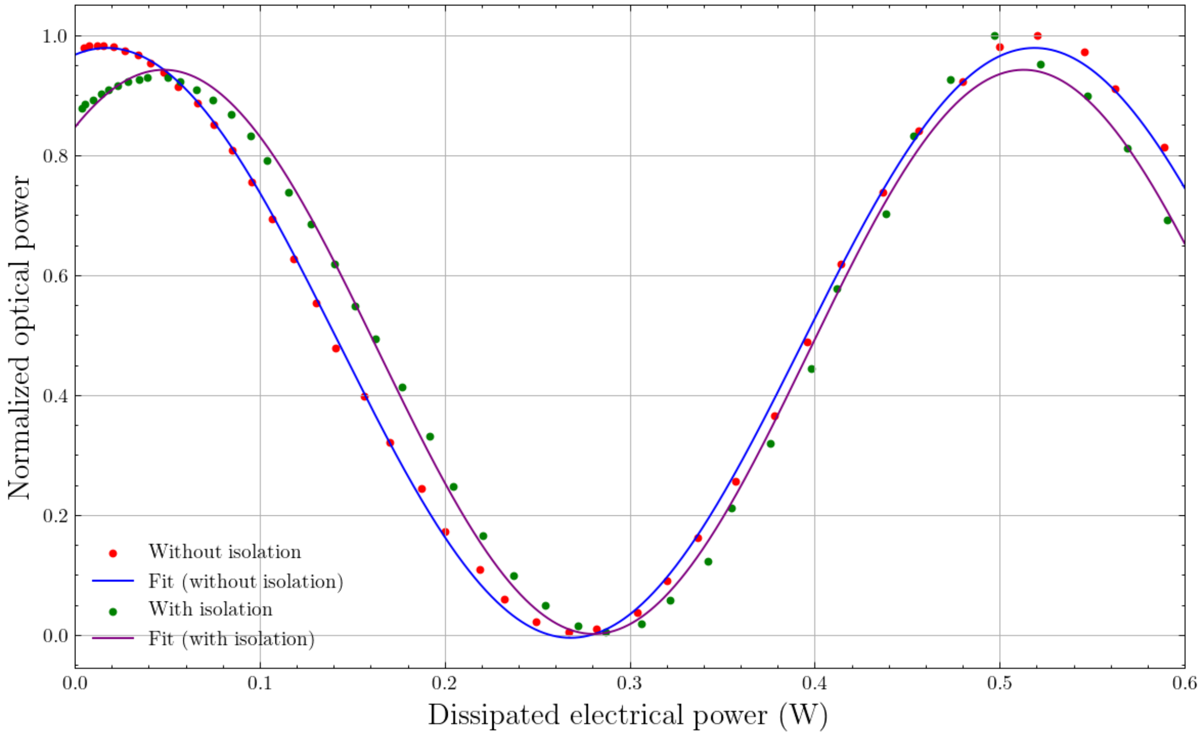

Figure 5.13: Normalized output optical powers through the lower arm of the MZI without and with isolation.

The estimated α and $P_{2\pi}$ values are present in table 5.3.

	without isolation		with isolation	
	value	uncertainty	value	uncertainty
α (rads/W)	12.747	0.001	13.908	0.004
$P_{2\pi}$ (mW)	492.90	0.05	451.76	0.1

Table 5.3: Parameters taken from the performed fits for the MZI without and with isolation.

A curious first observation is that for the MZI with isolation, a larger offset in the X axis is observed, which is unexpected, since this parameter only depends on the waveguide structure. By using arguments similar to those in section 5.5, it is lead to believe that the isolation step, which included glass ablation, could have further changed the residual stress profile of the material, ultimately changing the optical properties of the interferometric arm and, consequently, the phase of propagating light.

The $P_{2\pi}$ obtained for this MZI without isolation is a lot higher than that obtained for the previous one. This could be due to a faulty microheater, or the presence of a higher quantity of debris at the surface of the microheater, since this device has $(10/3)^2$ times more surface area, absorbing a lot more heat. Despite this decrease in efficiency, an 8% decrease in $P_{2\pi}$ is observed in relation to the same MZI with no isolation, showing an increased performance.

5.7 Conclusions

In this section, thermal phase-shifted MZIs were successfully produced using the FLDW technique.

A preliminary study on the metal layer (gold and chromium) ablation conditions was performed in order to find the parameters that optimize electrical isolation. To that end, a repetition rate of 500 kHz and a MituToyo 10 x lens with a 0.26 numerical aperture were utilized. Writing speed, pulse energy and polarization orientation were varied, and the best ablation regime was found. This regime corresponds to a gold and glass ablation region, visible for pulse energies higher than 800 nJ, independently of writing speed, and energies between 600 nJ and 800 nJ with writing speeds inferior or equal to 0.1 mm/s.

Several interferometers with varying interferometric arm lengths (L_{arm}) were produced and, before gold deposition, the reflectivity was measured for all of them. Obtained reflectivities were non-zero, meaning that either the couplers were not 50:50, the arms possess different fabrication conditions, or asymmetry is present, with the latter ones being the most likely. Reflectivity offset increased after gold deposition, but not in a statistically meaningful way.

The microheaters were patterned on the substrate and analyzed. A linear dependence between microheater resistance and dissipated electrical power was observed, as predicted by equation (5.12), yielding an R_0 of 19.671 $\pm$ 0.008 Ω, smaller than the theoretical value by 19%, and a γ of 24.53 $\pm$ 0.02 Ω/W. An approximately linear behavior was also observed for the power dependence on voltage at the microheater terminals.

By varying electrical power in the microheater, output power was simultaneously measured at both the upper and lower ports of the MZI with an L_{arm} of 3 mm, yielding an α of 16.743 $\pm$ 0.005 rads/W and a Δ of 0.0859 $\pm$ 0.0003 rads/mm. A $P_{2\pi}$ of 375.3 $\pm$ 0.1 mW, 21% higher than the theoretical value calculated (309 mW) due to the non-ideality of the real device. Even though the microheaters are electrically isolated from the rest of the gold, they are not thermally isolated, since heat can propagate from the glass to the rest of the gold and heat it up. This gold, in turn, can heat up the opposite arm, raising the power necessary for a 2π phase shift.

The dynamic response of the device was analyzed, and rise and fall times of the system's response were determined to be 24 ms and 32 ms, respectively. The higher fall time probably stems from the absence of a heat sink, not providing an efficient way to dissipating heat. An estimation of the system's bandwidth was made, yielding 14.58 Hz.

To verify if the surrounding gold indeed decreases device efficiency, the same device, with an L_{arm} of 10 mm, was tested before and after creating an isolation area around the microheater. An unexpected extra offset in dissipated electrical power was observed. Since the fabrication parameters used to make the isolation were enough to ablate the glass, the residual stress profile of the material could have changed, which in turn led to a modification of the interferometric arm's properties, slightly changing its phase. A decrease in $P_{2\pi}$ was observed, showing that the isolation increased device efficiency. Further increasing this isolation area could lead to even higher efficiencies.

6 Conclusions and further developments

Throughout this work, the femtosecond laser direct writing technique was explored on EAGLE2000 glass to fabricate several optical devices and optimize them in terms of insertion losses, compactness, and, for the MZIs, electrical power dissipation.

Throughout all produced devices, some laser parameters were kept fixed, namely a 1 MHz repetition rate, a 0.42 numerical aperture, a beam polarization parallel to te writing direction and an inscription depth of 50 μm.

To minimize insertion losses, straight waveguides were produced with varying writing speeds and pulse energies. Coupling losses and MFDs in the X and Y directions showed an increase with increasing pulse energy, probably due to a higher modification volume, which increased mode sizes. In general, for every pulse energy, coupling losses and MFDs decreased for increasing writing speed, probably due to a smaller modification volume caused by a lower fluence. Propagation losses showed an increase with smaller pulse energies, probably due to the weaker confinement. This is also verified for the same pulse energy and higher writing speeds, due to the smaller fluence. Overall, a pulse energy of 150 nJ and a writing speed of 35 mm/s were chosen for posterior designs.

Several s-bends were produced with a vertical offset of 112.5 μm and a varying radii of curvature. A decrease of bending losses was observed for increasing radii until a region of minimal losses is achieved. To minimize device size, a 70 mm radius of curvature was chosen for future devices, introducing bending losses of 0.97 dB. The decaying exponential empyrical law for bending losses per centimeter was also verified.

Various directional couplers with different interaction region separations (s_i) and lengths (L_i) were tested to study several device parameters such as power splitting, asymmetry, coupling length, the power splitting introduced by the s-bends. The main objective is to find the device that allows for reliable 50:50 power splitting. For each waveguide separation in the set 15, 20, 25 μm, interaction lengths ranging from 0 to 7.35 mm were tested. For the 15 μm separation devices, a modulation amplitude F of 0.9675 $\pm$ 0.0001 was observed. An asymmetry Δ of 0.0867 $\pm$ 0.0003 rads/mm was seen as the responsible for a non-full power transfer between arms of the coupler, with a minimum reflectivity of 0.014 being achieved. The s-bends introduced an initial phase ϕ_0 of 0.8152 $\pm$ 0.0006 rads. A coupling length L_c of 3.2625 $\pm$ 0.0001 mm was achieved. The 20 μm separation showed an unexpected power transfer behavior, not following the expected sinusoidal tendency for small interaction lengths. A smaller asymmetry Δ of 0.07917 $\pm$ 0.00002 rads/mm was obtained, as well as a smaller initial phase ϕ_0 of 0.4330

$\pm$ 0.001 rads and a higher coupling length L_c of 6.3926 $\pm$ 0.0001 mm all point to a higher separation. The 25 μm separation did not present any conclusive results. Although power is seen to pass from the lower input to the upper output arm with increasing l_c, the power that stays in the lower output arm does not seem to diminish, with the consequence of increasing total output power. A secondary oscillation is seen for both arms, which can indicate coupling of higher order modes. The 15 μm length was chosen in order to better study a full period of modulation. To this end, 115 couplers were produced with interaction lengths ranging from 1 to 6 mm to cover all possible reflectivities. It was not possible to achieve a full range of reflectivities due to the previously observed asymmetry, which showed to be higher this time, sitting at Δ=0.0908 $\pm$ 0.0001 rads/mm. An interaction length of 3.369 mm was chosen to produce 50:50 couplers to use in Mach-Zehnder interferometers.

A study on gold ablation was performed to find the best writing speeds and pulse energies to electrically isolate the microheaters. A repetition rate of 500 kHz and an objective with a numerical aperture of 0.26 were chosen. With a parallel orientation of the polarization, optimal ablation conditions (gold and glass ablation) were found for energies above 800 nJ and arbitrary writing speed, as well as for energies between 600 and 800 nJ and writing speeds smaller or equal to 0.1 mm/s. Several interferometric devices were produced and reflectivity was tested before and after the gold deposition. A non-zero reflectivity was observed and it increased after gold was deposited. This could be due to non-50:50 couplers, the presence of an asymmetry Δ or slightly different fabrication conditions for both arms, with the lattere two being the most likely. Microheaters were patterned and analyzed for their electrical properties. A linear dependence of resistance on dissipated electrical power was found, yielding an R_0 of 19.671 $\pm$ 0.008 Ω, smaller than the theoretical value by 19% and a γ of 24.53 $\pm$ 0.02 Ω/W. The dissipated power's dependence on voltage at the microheater's terminals also showed an approximately linear behavior.

The MZIs were tested for their reflectivity as a function of dissipated power. An α coefficient was found to be 16.743 $\pm$ 0.005 rads/W and an asymmetry Δ of 0.0859 $\pm$ 0.0003 rads/mm. This corresponds to a $P_{2\pi}$ of 375.3 $\pm$ 0.1 mW, higher than the value predicted of 309 mW. This discrepancy can be attributed to the fact that, although the microheaters are electrically isolated, they are not thermally isolated from the rest of the gold, and heat could have propagated through the glass to the outside gold, making it work like a heater, invalidating the thin wire approximation, which diminishes efficiency and by heating up the other arm, raising the necessary power to perform a 2π phase shift. The device was subjected to an input step voltage, and rise and fall times were determined to be 24 ms and 32 ms, respectively. The higher small time can be due to the absence of a heat sink, not providing an efficient way to dissipate heat. From this rise time, a rough estimation of the device's bandwidth was made, yielding 14.58 Hz.

To assess if the gold surrounding the microheater diminishes device efficiency, the same device (with an L_{arm} of 10 mm) was analyzed before and after creating an isolation area around the microheater. An 8% decrease in $P_{2\pi}$ was observed, however, an extra offset in dissipated power was observed, probably due to interferometric arm modifications induced by the shock waves created during the isolation production.

Overall, several factors can be improved in order to make the system more compact, energy efficient, and with a higher bandwidth. To start, the 15 μm couplers showed a 50:50 power splitting zone at smaller interaction lengths, however this was discarded due to the unexpected behavior observed. An in-depth study of these interaction lengths and the use of different geometries could lead to much more compact and fault tolerant directional couplers. Further increasing the isolation area around the microheaters could lead to higher efficiencies, taking it closer to the theoretical value.

Furthermore, by creating a trench in between the two interferometric arms, or a bridge on one arm, heat would not be able to propagate to the opposite arm, further increasing efficiency. A colleague was also able to minimize the radius of curvature by making multiple overlapping laser passes. An annealing step could also increase the refractive index contrast between core and cladding, minimizing curvature losses and overall decreasing device footprint.

Response times and power dissipation could be significantly reduced by making use of electro-optic materials, such as Lithium Niobate ($LiNBo_3$). High bandwidths (in the GHz) as well as energies in the sub-pJ per bit, all while keeping a footprint in the few mm^2 were already reported [80].

Once device footprint becomes low enough, several MZIs could be stacked in a single chip to create simple photonic circuits, such as optical logic gates, which would then allow for the creation of basic programmable PICs to perform arbitrary unitary linear transformations on input states of light, allowing for the production of wavelength filters or real-time vector matrix products. These last devices are crucial in neuromorphic and quantum computing.

References

[1] Peter G. Kazansky, Weijia Yang, Erica Bricchi, James Bovatsek, Alan Arai, Yasuhiko Shimotsuma, Kiyotaka Miura, and Kazuyuki Hirao. ”quill” writing with ultrashort light pulses in transparent materials. *Applied Physics Letters*, 90, 2007.

[2] Vítor Alexandre Oliveira Amorim, Paulo Vicente Silva Marques, and Pedro Alberto Silva Jorge. Fast prototyping of advanced sensing devices using three-dimensional direct writing with femtosecond laser. Technical report.

[3] Francesco Ceccarelli, Simone Atzeni, Alessandro Prencipe, Raffaele Farinaro, and Roberto Osellame. Thermal phase shifters for femtosecond laser written photonic integrated circuits. *Journal of Lightwave Technology*, 37:4275–4281, 6 2019.

[4] Fulvio Flamini, Lorenzo Magrini, Adil S. Rab, Nicolò Spagnolo, Vincenzo D’Ambrosio, Paolo Mataloni, Fabio Sciarrino, Tommaso Zandrini, Andrea Crespi, Roberta Ramponi, and Roberto Osellame. Thermally reconfigurable quantum photonic circuits at telecom wavelength by femtosecond laser micromachining. *Light: Science and Applications*, 4, 11 2015.

[5] Shane M Eaton, Haibin Zhang, Mi Li Ng, Jianzhao Li, Wei-Jen Chen, Stephen Ho, Peter R Herman Edward S Rogers, C B Schaffer, J F Garcia, and E Mazur. Transition from thermal diffusion to heat accumulation in high repetition rate femtosecond laser writing of buried optical waveguides. Technical report, 2008.

[6] Vítor A. Amorim, João M. Maia, Duarte Viveiros, and P. V. S. Marques. Addressing the fabrication difficulties of femtosecond laser written surface waveguides for enhanced evanescent coupling. *EPJ Web of Conferences*, 215:15003, 2019.

[7] D. Gloge. Bending loss in multimode fibers with graded and ungraded core index. Technical report, Applied Optics, 11 1972.

[8] James D. Meindl, Qiang Chen, and Jeffrey A. Davis. Limits on silicon nanoelectronics for terascale integration. *Science*, 293(5537):2044–2049, 2001.

[9] Wenchao Tian, Yifan Wang, Haojie Dang, Huahua Hou, and Yuanyuan Xi. Photonic integrated circuits: Research advances and challenges in interconnection and packaging technologies, 8 2025.

[10] Yichen Shen, Nicholas C. Harris, Scott Skirlo, Mihika Prabhu, Tom Baehr-Jones, Michael Hochberg, Xin Sun, Shijie Zhao, Hugo Larochelle, Dirk Englund, and Marin Soljacic. Deep learning with coherent nanophotonic circuits. *Nature Photonics*, 11:441–446, 6 2017.

[11] Jianwei Wang, Fabio Sciarrino, Anthony Laing, and Mark G Thompson. Integrated photonic quantum technologies. Technical report.

[12] Jacquiline Romero and Gerard Milburn. Photonic quantum computing. 4 2024.

[13] Ciro Pentangelo, Niki Di Giano, Simone Piacentini, Riccardo Arpe, Francesco Ceccarelli, Andrea Crespi, and Roberto Osellame. High-fidelity and polarization-insensitive universal photonic processors fabricated by femtosecond laser writing. *Nanophotonics*, 13:2259–2270, 5 2024.

[14] Roger Dangel, Jens Hofrichter, Folkert Horst, Daniel Jubin, Antonio La Porta, Norbert Meier, Ibrahim Murat Soganci, Jonas Weiss, and Bert Jan Offrein. Polymer waveguides for electro-optical integration in data centers and high-performance computers. *Optics Express*, 23:4736, 2 2015.

[15] Muhammad A. Butt. Integrated optics: Platforms and fabrication methods. *Encyclopedia*, 3:824–838, 6 2023.

[16] Bhavin J. Shastri, Alexander N. Tait, T. Ferreira de Lima, Wolfram H.P. Pernice, Harish Bhaskaran, C. D. Wright, and Paul R. Prucnal. Photonics for artificial intelligence and neuromorphic computing, 2 2021.

[17] Michael Reck, Anton Zeilinger, Herbert J Bernstein, and Philip Bertani. Experimental realization of any discrete unitary operator. Technical report, 1994.

[18] Zachary Chaboyer, A. Stokes, J. Downes, M. J. Steel, and Michael J. Withford. Design and fabrication of reconfigurable laser-written waveguide circuits. *Optics Express*, 25:33056, 12 2017.

[19] William R. Clements, Peter C. Humphreys, Benjamin J. Metcalf, W. Steven Kolthammer, and Ian A. Walmsley. Optimal design for universal multiport interferometers. *Optica*, 3(12):1460–1465, Dec 2016.

[20] Richard A. Lawson and Alex P.G. Robinson. *Overview of materials and processes for lithography*, volume 11, pages 1–90. Elsevier Ltd, 2016.

[21] R. R. Gattass and E. Mazur. Femtosecond laser micromachining in transparent materials. *Nature Publishing Group*, 4 2008.

[22] K M Davis, K Miura, N Sugimoto, and K Hirao. Writing waveguides in glass with a femtosecond laser. Technical report, 1996.

[23] Yong Lai Zhang, Qi Dai Chen, Hong Xia, and Hong Bo Sun. Designable 3d nanofabrication by femtosecond laser direct writing, 2010.

[24] Yue Chen Jia, Shi Xiang Wang, and Feng Chen. Femtosecond laser direct writing of flexibly configured waveguide geometries in optical crystals: Fabrication and application. *Opto-Electronic Advances*, 3:1–12, 2020.

[25] N.N. Skryabin, S.A. Zhuravitskii, I.V. Dyakonov, S.S. Straupe, A.A. Kalinkin, and S.P. Kulik. Femtosecond-laser-written low-loss multiscan waveguides in fused silica. *Phys. Rev. Appl.*, 22:064079, Dec 2024.

[26] Feng Chen and J. R.Vázquez de Aldana. Optical waveguides in crystalline dielectric materials produced by femtosecond-laser micromachining, 3 2014.

[27] Shutong Wang, Junjie Yang, Guoliang Deng, and Shouhuan Zhou. Femtosecond laser direct writing of flexible electronic devices: A mini review, 2 2024.

[28] Luís Fernandes. *Birefringence and Bragg grating control in femtosecond laser written optical circuits*. PhD thesis, 2012.

[29] Vitor A. Amorim, Duarte Viveiros, Joao M. Maia, and P. V. S. Marques. Mass producible low-loss broadband optical waveguides in eagle2000 by femtosecond laser writing. *IEEE Photonics Technology Letters*, 31:1658–1661, 10 2019.

[30] Shane Eaton, Wei-Jen Chen, Haibin Zhang, Rajiv Iyer, Jianzhao Li, Mi Li Ng, S.L. Ho, J. Aitchison, and P.R. Herman. Spectral loss characterization of femtosecond laser written waveguides in glass with application to demultiplexing of 1300 and 1550 nm wavelengths. *Journal of Lightwave Technology*, 27:1079–1085, 05 2009.

[31] Rishu Bhatia. Laser technology: A review. Technical report, Deepika, 2017.

[32] Dezhi Tan, Kaniyarakkal N. Sharafudeen, Yuanzheng Yue, and Jianrong Qiu. Femtosecond laser induced phenomena in transparent solid materials: Fundamentals and applications, 3 2016.

[33] Stefan Witte and Kjeld S.E. Eikema. Ultrafast optical parametric chirped-pulse amplification, 2012.

[34] Igor Jovanovic. Chirped□pulse amplification. *Optik & Photonik*, 5:30–33, 12 2010.

[35] João Miguel Mendes da Silva Maia and Paulo Vicente Da Silva Marques. Femtoetch-femtosecond laser micromachining and applications in microfluidics and optofluidics. Technical report, 2016.

[36] Roberto Osellame, Giulio Cerullo, and Roberta Ramponi, editors. *Femtosecond Laser Micromachining*, volume 123 of *Topics in Applied Physics*. Springer, Berlin, Heidelberg, 2012.

[37] Chris B Schaffer, André Brodeur, and Eric Mazur. Laser-induced breakdown and damage in bulk transparent materials induced by tightly focused femtosecond laser pulses. Technical report, 2001.

[38] A. P. Joglekar, H. Liu, G. J. Spooner, E. Meyhöfer, G. Mourou, and A. J. Hunt. A study of the deterministic character of optical damage by femtosecond laser pulses and applications to nanomachining. *Applied Physics B: Lasers and Optics*, 77:25–30, 8 2003.

[39] Alexander M Streltsov and Nicholas F Borrelli. Study of femtosecond-laser-written waveguides in glasses. Technical report, 2002.

[40] S. K. Sundaram and E. Mazur. Inducing and probing non-thermal transitions in semiconductors using femtosecond laser pulses. *Natura Publishing Group*, 12 2002.

[41] Martin Ams, Graham D. Marshall, Peter Dekker, Mykhaylo Dubov, Vladimir K. Mezentsev, Ian Bennion, and Michael J. Withford. Investigation of ultrafast laser-photonic material interactions: Challenges for directly written glass photonics. *IEEE Journal on Selected Topics in Quantum Electronics*, 14:1370–1388, 9 2008.

[42] João M. M. S. Maia, Paulo V. S. Marques, and Carla S. S. C. Rosa. Fabrication of optofluidic systems by femtosecond laser micromachining. Technical report, Faculty of Sciences of University of Porto, 2021.

[43] Pasquale Barbato, Roberto Osellame, and Rebeca Martínez Vázquez. Femtosecond laser nanomachining of high-aspect-ratio channels in bulk fused silica. *Advanced Materials Technologies*, 9 2024.

[44] Sören Richter, Christopher Miese, Sven Döring, Felix Zimmermann, Michael J. Withford, Andreas Tünnermann, and Stefan Nolte. Laser induced nanogratings beyond fused silica - periodic nanostructures in borosilicate glasses and ule™. *Optical Materials Express*, 3:1161, 8 2013.

[45] Felix Zimmermann, Anton Plech, Sören Richter, Andreas Tünnermann, and Stefan Nolte. Ultrashort laser pulse induced nanogratings in borosilicate glass. *Applied Physics Letters*, 104, 5 2014.

[46] Qiong Xie, Maxime Cavillon, Diego Pugliese, Davide Janner, Bertrand Poumellec, and Matthieu Lancry. On the formation of nanogratings in commercial oxide glasses by femtosecond laser direct writing. *Nanomaterials*, 12, 9 2022.

[47] Rod Taylor, Cyril Hnatovsky, and Eli Simova. Applications of femtosecond laser induced self-organized planar nanocracks inside fused silica glass, 4 2008.

[48] Pasquale Barbato, Roberto Osellame, and Rebeca Martínez Vázquez. Nanochannels in fused silica through naoh etching assisted by femtosecond laser irradiation. *Materials*, 17, 10 2024.

[49] J W Chan, T Huser, S Risbud, and D M Krol. Structural changes in fused silica after exposure to focused femtosecond laser pulses. Technical report, 2001.

[50] Kazuyoshi Itoh, Wataru Watanabe, Stefan Nolte, and Chris B. Schaffer. Ultrafast processes for bulk modification of transparent materials. Technical report, 7 2006.

[51] C. B. Schaffer, J. F. García, and E. Mazur. Bulk heating of transparent materials using a high-repetition-rate femtosecond laser. *Applied Physics A: Materials Science and Processing*, 76:351–354, 3 2003.

[52] Chris B Schaffer, André Brodeur, José F García, and Eric Mazur. Micromachining bulk glass by use of femtosecond laser pulses with nanojoule energy. Technical report, 2001.

[53] Alexander Arriola, Simon Gross, and Nemanja Jovanovic. Low bend loss waveguides enable compact, efficient 3d photonic chips. *Applied Physics Letters*, 90, 2007.

[54] S J Beecher, R R Thomson, D T Reid, N D Psaila, M Ebrahim-Zadeh, and A K Kar. Strain field manipulation in ultrafast laser inscribed bib3o6 optical waveguides for nonlinear applications. Technical report, 2011.

[55] Selig Hecht. The visual discrimination of intensity and the weber-fechner law. *The Journal of General Physiology*, 9 1924.

[56] Vítor Alexandre and Oliveira Amorim. Fabrication of integrated optical devices in fused silica by femtosecond laser direct writing. Technical report.

[57] Simone Piacentini, Roberto Osellame, Roberta Ramponi, and Marco Finazzi. Femtosecond laser writing of photonic integrated circuits for quantum technologies. Technical report, 2018.

[58] Katsunari Okamoto. *Coupled Mode Theory*. 2006.

[59] Azzedine Boudrioua. Optical waveguide theory. Technical report, ISTE, Ltd., 2009.

[60] Sembiam R. Rengarajan. On higher order mode cutoff frequencies in elliptical step index fibers. Technical report, IEEE, 8 1989.

[61] Dietrich Marcuse. *WEAKLY GUIDING OPTICAL FIBERS*, pages 60–96. Elsevier, 1991.

[62] Shane M Eaton, Haibin Zhang, Peter R Herman, Edward S Rogers, Fumiyo Yoshino, Lawrence Shah, James Bovatsek, and Alan Y Arai. Heat accumulation effects in femtosecond laser-written waveguides with variable repetition rate. Technical report, 2005.

[63] G. P.. Agrawal. *Fiber-optic communication systems*. Wiley-Interscience, 2002.

[64] F. J. Mustieles, E. Ballesteros, and P. Baquero. Theoretical s-bend profile for optimization of optical waveguide radiation losses. *IEEE*, 1993.

[65] Guangyu Li, Kim A Winick, Ali A Said, Mark Dugan, and Philippe Bado. Waveguide electro-optic modulator in fused silica fabricated by femtosecond laser direct writing and thermal poling. Technical report, 2006.

[66] Giacomo Corrielli, Andrea Crespi, and Roberto Osellame. Femtosecond laser micromachining for integrated quantum photonics, 11 2021.

[67] Thomas Meany, Markus Gräfe, René Heilmann, Armando Perez-Leija, Simon Gross, Michael J. Steel, Michael J. Withford, and Alexander Szameit. Laser written circuits for quantum photonics. *Laser & Photonics Reviews*, 9(4):363–384, 2015.

[68] Yu-Jun Quan, Pei-De Han, Xiao-Dong Lu, Zhi-Cheng Ye, and Li Wu. Optical interleaver based on directional coupler in a 2D photonic crystal slab with triangular lattice of air holes. *Optics Communications*, 270(2):203–206, February 2007.

[69] Katsuyuki Imoto, Hirohisa Sano, and Masaru Miyazaki. Guided-wave multi/demultiplexers with high stopband rejection. *Appl. Opt.*, 26(19):4214–4219, Oct 1987.

[70] Nasuhi Yurt. Gaas/algaas polarization splitting directional couplers, 1997.

[71] Enakshi Khular Sharma, Jyoti Prasad Nath, and Nikhil Dhingra. Coupled mode theory and coupled mode photonic devices: A review. Technical report, 2021.

[72] Chin-Lin Chen. Foundations for guided-wave optics. Technical report, John Wiley & Sons, 2007.

[73] Nishiara. coupling mode theory.

[74] Feng Yu, Zhen-Nan Tian, Simone Piacentini, Xiao-Yan Li, Qi-Dai Chen, Roberto Osellame, and Hong-Bo Sun. Resetting directional couplers for high-fidelity quantum photonic integrated chips. *Optics Letters*, 46:5181, 10 2021.

[75] John M Jewell. Thermooptic coefficients of some standard reference material glasses. Technical report, 4 1991.

[76] Eagle2000. Technical report, Corning, 4 2005.

[77] T. H. Gilani and Dian Rabchuk. Electrical resistivity of gold thin film as a function of film thickness. *Canadian Journal of Physics*, 96:272–274, 2018.

[78] Michael Huff. Review paper: Residual stresses in deposited thin-film material layers for micro- and nano-systems manufacturing, 12 2022.

[79] Matteo Calvarese, Petra Paiè, Francesco Ceccarelli, Federico Sala, Andrea Bassi, Roberto Osellame, and Francesca Bragheri. Strategies for improved temporal response of glass-based optical switches. *Scientific Reports*, 12, 12 2022.

[80] Yu Li, Muhan Sun, Ting Miao, and Jianping Chen. Towards high-performance pockels effect-based modulators: Review and projections, 7 2024.